On Modeling Three-Phase Flow in Discretely Fractured Porous Rock

by

Kenneth Mark Walton

A thesis

presented to the University of Waterloo

in fulfillment of the

thesis requirement for the degree of

Doctor of Philosophy

in

Earth Sciences

Waterloo, Ontario, Canada, 2013

Author's Declaration

I hereby declare that I am the sole author of this thesis. This is a true copy of the thesis, including any required final revisions, as accepted by my examiners.

I understand that my thesis may be made electronically available to the public.

Kenneth Mark Walton

Abstract

Numerical modeling of fluid flow and dissolved species transport in the subsurface is a challenging task, given variability and measurement uncertainty in the physical properties of the rock, the complexities of multi-fluid interaction, and limited computational resources. Nonetheless, this thesis seeks to expand our modeling capabilities in the context of contaminant hydrogeology. We describe the numerical simulator *CompFlow Bio* and use it to model invasion of a nonaqueous phase liquid (NAPL) contaminant through the vadose zone and below the water table in a fractured porous rock. *CompFlow Bio* is a three-phase, multicomponent, deterministic numerical model for fluid flow and dissolved species transport; it includes capillary pressure and equilibrium partitioning relationships. We have augmented the model to include randomly generated, axis-aligned, discrete fracture networks (DFNs). The DFN is coupled with the porous medium (PM) to form a single continuum. The domain is discretized using a finite-volume scheme in an unstructured mesh of rectilinear control volumes (CVs).

Herein we present the governing equations, unstructured mesh creation scheme, algebraic development of fracture intersection CV elimination, and coupling of PM CVs over a fracture plane to permit asperity contact bridged flow. We include: small scale two-phase water-air and NAPL-water simulations to validate the practice of intersection CV elimination; small scale simulations with water-air, NAPL-water, and NAPL-water-air systems in a grid refinement exercise and to demonstrate the effect of asperity contact bridged flow; intermediate scale 3D simulations of NAPL invading the saturated zone, based on the Smithville, Ontario, site; intermediate scale 2D and 3D simulations of NAPL invading the vadose zone and saturated zone with transient recharge, based on the Santa Susana Field Laboratory site, California.

Our findings indicate that: the formulation provides a practical and satisfactory way of modeling three-phase flow in discretely fractured porous rock; numerical error caused by spatial discretization manifests itself as several biases in physical flow processes; that asperity contact is important in establishing target water saturation conditions in the vadose zone; and simulation results are sensitive to relative permeability-saturation-capillary pressure relationships. We suggest a number of enhancements to *CompFlow Bio* to overcome certain computational limitations.

Acknowledgements

First and foremost, I acknowledge my supervisor, Dr. Andre Unger, for his support and mentorship. I sincerely thank him for his dedication to this project – his commitment, guidance and timely advice have made this work possible. I acknowledge also my thesis committee members, Drs. Edward Sudicky, Beth Parker, and Marios Ioannidis, for their contributions and for supporting this project's transition from a Master's level to Ph.D. status. Furthermore, I thank all members of the committee for their teachings, advice and editorial comments throughout this process.

Specific thanks go to: Dr. Ioannidis for his expertise in crafting discussions in Appendix A and Dr. Unger in support of Appendix C; the four anonymous reviewers who provided critiques on the content of Chapter 2 and Chapter 3; my thesis examiners Drs. Peter Forsyth and Rainer Helmig who generously gave their time and thoughtful criticism.

I gratefully acknowledge my sources of funding through this course of research: during my time as a Master's candidate, from Strategic Environmental Research and Development Program, ER-1610, garnered by Dr. Sudicky; during the balance of time, from The Boeing Company via the University Consortium for Field-Focused Groundwater Contamination Research, led by Dr. Parker and Dr. John Cherry, and an Industrial Research Chair grant from the Natural Sciences and Engineering Research Council of Canada held by Dr. Parker.

Many fellow students have assisted me over the course of my study either as coinvestigators to move this project forward or as friends to set it aside. I thank Xiaomin Wang, Mike Makahnouk, Rodrigo Herrera, Scott Jasechko, Matt Alexander, Kaiying Qiu, Fanlong Meng, and Chenlong Wang.

Finally, but not at all in the least, I owe a great debt of gratitude to my wife, Tara Gomes, my parents, Jim and Bonnie Walton, and my aunt and uncle, Wendy and Robert DesChamp, who have given their support throughout. Mom: Your proofreading skills are uncommaly good.

Dedication

To my love, Tara.

In memory of Grandma Raddon.

Table of Contents

List of Figures

List of Tables

List of Symbols

A summary of the notation in the governing equations (Section 2.2.1) is given by:

d is depth [m];

δ_{IJ} is the Kroneker delta function at matrix indices *I* and *J;*

g is the gravitational acceleration constant [m/s^2];

ϕ is porosity [-];

$\mathbb{K}$ is the intrinsic permeability tensor [m^2];

K_d is sorption coefficient [m^3/kg];

k_{rl} is relative permeability of phase l [-];

$l \epsilon \{q, n, g\}$, fluid phase l is one of aqueous, q, nonaqueous, n, or gas, g;

M_l is molar density of phase l [mol/m^3];

μ_l is coefficient of dynamic viscosity of phase l [kg m^{-1} s^{-1}];

ω_p is the molecular mass of component p [kg/mol];

$P_{c,l_1 l_2}$ is the two-phase capillary pressure between phase l_1 and l_2 [kg m^{-1} s^{-2}];

P_l is fluid pressure of phase l [kg m^{-1} s^{-2}];

$p \epsilon \{w, a, c\}$ component species p is one of water, w, air, a, or TCE, c;

Q_p is a source/sink term for species p [mol m^{-3} d^{-1}];

ρ_l is mass density of phase l [kg/m^3];

ρ_b is bulk density of the porous medium [kg/m^3];

S_l is saturation of phase l [-];

t is time [d]; and

X_{pl} is mole fraction of species p in phase l [-].

A summary of the notation and certain basic formulae for the discretized equations (Section 2.2.4) is given by:

$\alpha^{l}_{L,ij}, \alpha^{l}_{TH,ij}, \alpha^{l}_{TV,ij}$ are longitudinal, transverse horizontal, and transverse vertical dispersivities of phase *l* at the *i-j* interface [m^2];

b_{BC} is the efficiency of a source/sink term [-];

BC the subscript denotes a variable or constraint in a source/sink term;

$B_i = \begin{cases} 10^6 & \text{for "invariant property"} \\ 1 & \text{otherwise} \end{cases}$ is a volume multiplier in node *i* [-];

i, j with $i \neq j$, are indices of the i^{th} and j^{th} node;

$\Gamma^{N+1}_{l,i}$ the total fluid potential of phase *l* in node *i* at time step *N*+1 [kPa];

$\Gamma^{N+1}_{l,ij}$ is the fluid potential difference between *i* and *j* [kPa];

γ_{ij} is the influence coefficient for the advective flux between *i* and *j* [m^3];

γ^{*}_{ij} is the influence coefficient for the diffusive flux between *i* and *j* [m^2 d];

η_i is the set of control volumes that are neighbours of node *i*;

$k_{rl,i}$ is the relative permeability of phase *l* in node *i* [-];

$\lambda_{l,i} = k_{rl,i} M_{l,i} / \mu_{l,i}$ is the phase mobility term [mol d m^{-2} kg^{-1}];

$\lambda_{l,BC} = M_{l,BC} / \mu_{l,BC}$ is a mobility term for phase *l* at the boundary [mol d m^{-2} kg^{-1}];

$M_{l,i}$ is molar density of phase *l* in node *i* [mol/m^3];

$\mu_{l,i}$ is coefficient of dynamic viscosity of phase *l* in node *i* [kg m^{-1} d^{-1}];

N is a time step index value;

$\vec{n}_{ij}$ is the normal vector to the *i-j* interface [m];

$S^{N+1}_{l,ij} = \frac{S^{N+1}_{l,i} S^{N+1}_{l,j} (V_i + V_j)}{S^{N+1}_{l,j} V_i + S^{N+1}_{l,i} V_j}$ is the harmonic mean of saturations weighted by node volume [-];

$\hat{S}_{\text{smooth}}$ is a parameter used in smoothing relative permeability curves [-];

$\tau = \left(\phi_{\eta_i} S_{l,\eta_i}^{N}\right)^{7/3}$ is the tortuosity factor [-];

Δt^{N+1} is the time step size at time index *N+1* [d];

$\text{ups}\langle i,j\rangle = \begin{cases} i & \Gamma_{l,ij} \geq 0 \\ j & \Gamma_{l,ij} < 0 \end{cases}$ is the upstream node based on total potential of phase *l*; and

$v_{l,ij}^{N}$ is the velocity of phase *l* at the *i-j* interface at time step *N* in [m/d].

A summary of the notation for the algebraic development of intersection CV elimination (Section 2.2.5) is given by:

$F_{l,ij}$ the volumetric flow rate of phase *l* from *i* to *j* in [m^3/d];

$\gamma_{ij}, \gamma'_{ij}, \gamma''_{ij}$ influence coefficients for advective flux between *i* and *j* after zero, one, or two rounds of node elimination; and

$\eta_i = \{j_1, j_2, \ldots, k, \ldots, j_n\}$ is the set of neighbours of *i*. The *j*s and *k* are indices of neighbour CVs.

Chapter 1

Introduction

1.1 Motivation and General Scope

Numerical modeling is a task that is common in many investigations of the subsurface. In the fields of contaminant hydrogeology, petroleum reservoir engineering, geothermal engineering, and carbon sequestration, simulation of fluid and energy flows and transport of dissolved chemicals is widely used for evaluative and predictive purposes. Aside from physical characterization of the subsurface environment, numerical modeling is a challenging task because of heterogeneity, fractures, faults and karst in the subsurface materials, and complex interactions between fluids and chemical species. Formulation of such problems for deterministic simulation involves: 1) defining a set of governing equations, 2) determining parameters for physical constants or relationships in that set of equations, 3) constructing a spatial discretization of the domain of interest, and 4) assembling and solving the resultant numerical system of equations.

Herein we consider the first three aspects listed above in the context of contaminant hydrogeology. The basic scenario that motivates this study is the invasion of a nonaqueous phase liquid (NAPL) contaminant from the ground surface, through a fractured porous rock vadose zone, down to a groundwater aquifer. This involves the flow of three mutually interactive fluid phases (the aqueous phase, gas phase and nonaqueous phase) and three component species (water, air, and a NAPL contaminant) in a discretely fractured porous medium. Our emphasis shall be on a practical technique to model NAPL invasion, the spatial structure of the zone occupied by the NAPL (i.e. the source zone architecture), and how the source zone evolves.

For this task we employ and augment the numerical model *CompFlow Bio* developed by Unger et al. [1]. *CompFlow Bio* is a multiphase, multicomponent, first-order accurate, finite-volume simulator. We describe the novel enhancements incorporated into the simulator and consequent scientific findings in the section that follows.

1.2 Contributions

The scientific contributions of this thesis may be grouped in to three categories: theoretical aspects; insights from small scale numerical test problems; and insights from intermediate scale, field-relevant simulations.

Theoretical contributions include novel aspects of flow phenomena modeling and spatial discretization. In Chapter 2 we describe a method of control volume (CV) bisection to insert fractures in order to reduce the number of CVs in the computational domain, and we extend the algebraic process of Slough et al. [2] for eliminating CVs at the intersection of three orthogonal fractures. In Chapter 3 we introduce a simple approach to model flow through asperity contact points of opposite fracture walls as a means for fracture cross flow.

From two suites of small scale test problems in Chapter 3, we validate the practice of intersection elimination below the water table and qualitatively reveal biases to imbibition and fracture cross flow rates in a three-phase context induced by the spatial discretization.

The intermediate scale 2D and 3D simulations presented in Chapter 2 and Chapter 4 unite novel aspects outlined above and yield valuable information about the simulator's capabilities and limitations. They indicate a need for considering combined fracture and matrix flow both above and below the water table and also highlight the important role of fracture asperity contact area and relative permeability-saturation-capillary pressure relationships.

Overall, this thesis benefits researchers and contaminant hydrogeology practitioners who now have another tool to model flow in fractured rock and assess contamination and remediation scenarios.

1.3 Organization of this Document

This thesis is organized into five chapters and several appendices. Chapter 2 through Chapter 4 comprise the core of this work. These chapters provide their own contextual descriptions/literature reviews, results, and conclusions. Chapter 5 provides a summary of the major findings and suggests some topics for future study. Finally, the appendices contain foundationally important calculations, or other novel contributions.

Chapter 2

On Combined Matrix and Discrete Fracture Flow and Transport

Chapter Summary

To support modeling of nonaqueous phase liquid (NAPL) source zones as they evolve in the vadose and saturated zones in fractured rock, we present a set of governing equations and their discretization in the numerical model *CompFlow Bio*. This numerical model simulates isothermal flow and transport of three components (water, air and an oil/contaminant species) in three mobile and mutually interactive phases (aqueous, gas, and nonaqueous) in a 3D porous medium (PM) and discrete fracture network (DFN) domain using a first-order accurate, finite-volume formulation. Novel aspects include: 1) direct PM-to-PM flow across a fracture plane via asperity contact bridged flow; 2) PM control volume (CV) bisection to insert axis aligned, orthogonal, rough-walled fractures resulting in an unstructured mesh; and 3) algebraic reformulation of the flow equations to remove small CVs at the intersection of three fractures. We demonstrate our mesh technique using three meshes for a water-NAPL flow scenario including 1 year of NAPL loading and 100 years of migration and dissolution. The domain is 200×50×43 m and has 1900 randomly located fractures (fracture density ~1/m). We find that both fractures and the PM contribute to water flow and asperity contact reduces the bulk permeability of the fractured porous medium. The tradeoff is mesh-dependence of bulk transmissivity for water. Overall, this study outlines the framework for a useful simulator for multiphase flow in discretely fractured rock.

2.1 Introduction

Understanding of two- and three-phase fluid flow and solute transport in the subsurface is applicable to many fields. Petroleum engineering is tasked with optimizing production of oil from a reservoir by forced injection of water given the presence of resident gas trapped in the formation. Carbon sequestration in geologic repositories involves injection of supercritical carbon dioxide deep below the water table. Underground nuclear waste storage is concerned with migration of radionuclides away from the vadose zone repository over the long term. Finally, contaminant hydrogeology is often faced with spills of nonaqueous phase liquid (NAPL) contaminants that migrate through the vadose and saturated zones. These problems frequently arise in the geologic context of heterogeneous and fractured rock. Given the complex subsurface environment and the intricacies of multiphase flow, practitioners often use numerical models to assist in site assessment. One example where numerical modeling is being applied in the area of contaminant hydrogeology is at the former polychlorinated biphenyl waste transfer facility near Smithville, Ontario, Canada [3]. Numerical models are presently being employed at the Smithville site to assist in quantifying the extent of the source zone and dissolved plume and to evaluate possible remediation strategies [4].

In a general sense, this study outlines one approach to numerical modeling of three mutually interactive phases (i.e. the aqueous, nonaqueous and gas phases) in discretely fractured rock. We look at issues of spatially representing fractures and the rock matrix in the domain (geometric connectivity), and coupling the matrix, fractures and fracture intersections to quantify flow and transport processes (flux connectivity) in a computationally feasible manner. We introduce the relevant topics by: first, describing the conceptual pathway of contamination (which highlights physical phenomena captured in the numerical model); giving a brief history of numerical modeling in discretely fractured rock; and finally by describing how our numerical model augments what is currently reported in the literature.

Generalizing the Smithville site example, our approach to simulating the evolution of a contaminant source zone in the subsurface is based on the following conceptual pathway. The pathway is similar to that of Abriola and Pinder [5] but we add issues specific to fractured rock; it augments the pathway of Parker et al. [6] by including NAPL invasion in a fractured rock vadose zone. A diagram of this pathway is presented in Figure 2-1. Prior

to introduction of a NAPL contaminant we consider the air and water residing in the fractures and pore space of the porous medium (PM). At the ground surface, surface water and/or some portion of precipitation infiltrate by entering fractures or the rock matrix (a). The gas phase interacts freely with the atmosphere. Capillarity causes water to reside in the PM leaving fractures as primarily gas-filled (b). In its gravity-driven, downward flow path, water may encounter a gas-filled fracture. Water may mound above such a fracture or divert its path (c) if it cannot breach the barrier. If the fracture aperture is sufficiently small or if opposite fracture walls are in contact, then fracture cross flow may occur via a liquid bridge or an asperity contact bridge (d). Eventually the infiltrating water will meet the capillary fringe and the water table. The capillary fringe thickness in the PM may differ from that in the fracture network (e). Water will flow primarily in fractures below the water table but some flow may occur in the PM (f). Next, we consider introduction of a NAPL at the ground surface and the transition from a two-phase to a three-phase system. The NAPL invades the PM pore space or fracture voids by displacing resident air and water in varying proportions depending on capillarity and fluid entrapment (g). It continues downward in the vadose zone under the influence of gravity. Depending on fracture aperture, the NAPL front will lead in the fracture network and leave a trailing imbibition halo in the rock matrix (h). NAPL invasion continues through the capillary fringe where it may cause a depression (i). At the water table the NAPL may form a lens if it is less dense than water (i.e. an LNAPL) or may continue to infiltrate deeper if it is more dense than water (i.e. a DNAPL). Assuming an invading DNAPL, fractures below the water table act as conduits due to their relatively high permeability (j). The advance of the liquid will eventually halt and a terminal source zone architecture will be manifest if the NAPL release is finite. Physical processes such as dissolution, volatilization, sorption, diffusion and dispersion may occur concurrently with and be influential to the evolution of the source zone. These processes may lead to a plume of dissolved contaminant being transmitted away from the source zone over long periods via advective and diffusive fluxes of the solvent phase(s). Degradation processes may cause the plume to become stationary or even recede.

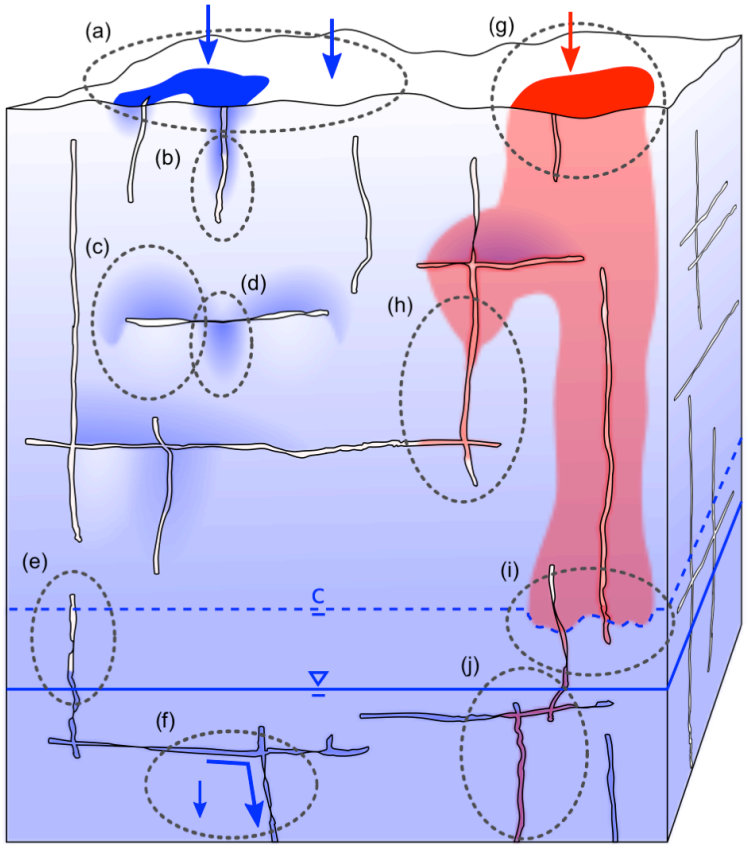

Figure 2-1 Schematic of phase structure and relevant flow phenomena in the conceptual pathway of contamination; an antecedent air-water system and invasion nonaqueous phase liquid (NAPL) to create an air-NAPL-water system.

In summary, each phase may flow from matrix-to-matrix, fracture-to-fracture, matrix-to-fracture, fracture-to-matrix (imbibition), or matrix-to-matrix across a fracture (fracture cross flow). The mode of flow depends on the three-phase saturation conditions, phase total potentials, fluid mobility, and capillary pressure (noting that the aqueous phase is assumed to be the most wetting and gas to be the least wetting). Additional influences to the source zone and plume include precipitation events, changes in the ambient barometric pressure at the ground surface, and temporal variation in the height of the water table.

To model these phenomena, or subsets thereof, Narasimhan [7] provides an excellent overview of the three broad classes of hydrogeological numerical models: equivalent porous medium (EPM); dual continuum models, which may be subcategorized as dual-porosity (DP) [8, 9, 10] or dual-permeability (DK) [11]; and models using discrete fracture networks (DFNs) [12, 13]. EPM models have been successfully applied to contaminant transport problems in highly fractured, high porosity systems [14] but may be unsuitable

for many other transport applications [15, 16] including more sparse fracture patterns [17, 18], or in cases where fracture flow is of explicit interest. Kazemi and Gilman [19] provide a brief overview of DP and DK models. DP models have recently been used by Ngien et al. [20] to study source zone evolution of LNAPL. DK models have been applied to nuclear waste repository modeling (e.g. Liu et al. [21]) and continue to be developed for the petroleum industry (e.g. Sarma and Aziz [22]). The draw back to this class of models is the use of a *shape factor* scaling the mass transfer between the matrix and fracture continua that may not be uniquely defined for a given geological setting [23]. This class handles fracture cross flow implicitly because fractures do not cross-cut the matrix. However, in a two-phase context the transfer function is fundamentally ill defined [24]. As computer power has increased, so too has the use of DFN models, which generally bear an extra computational burden of small volume nodes and sharp spatial contrasts in permeability. DFN models incorporating three mobile phases have been used in petroleum reservoir problems. Reichenberger et al. [25] proposed a two-phase, control volume finite-difference simulator that permitted complex discrete fracture geometry. Geiger et al. [26] developed a model using a hybrid finite-element finite-volume model for stochastically generated fracture networks with complex geometry based on the numerical *IMPES* technique. Hoteit and Firoozabadi have proposed a succession of single-phase DFN, and oil-water two-phase DFN flow and transport models with capillarity using combined discontinuous Galerkin and mixed hybrid finite-element methods [24, 27, 28, 29]. In references [24] and [29] in particular, they report that contrasts in capillary pressure may restrict nonwetting phase flux in heterogeneous PM or at a fracture plane. More recently, Moortgat et al. [30] expanded this platform to include compressible three-phase flow. They present their model in the context of carbon dioxide sequestration in a homogeneous, unfractured PM. Lesinigo et al. [31] present another DFN model that uses Darcean flow in the PM with Stokes-Brinkman flow in fractures to better capture kinetic fluid flow in single-phase flow problems. Flemisch et al. [32] have constructed a simulator framework that provides a robust set of physical processes and complex geometry, which includes the capacity for multiphase flow in a fractured porous medium. A recent exposition of this model is given in Tatomir et al. [33].

In this study, we expand on the work of Slough et al. [2] by augmenting the numerical model *CompFlow Bio* to address modeling goals related to the Smithville site. This model is a three-phase, multicomponent flow and transport simulator that incorporates compress-

ible fluid flow, capillary pressure, and equilibrium phase partitioning of component species. We use a newly implemented, 3D mesh generator to incorporate discrete fractures in a fashion that reduces the number of control volumes (CVs) and eliminates fracture intersection CVs. Site goals include modeling a DNAPL source zone and its distribution in the PM and fractures below the water table in order to predict the long term contaminant fluxes at a compliance boundary [4]. We use this conceptual problem to: find the maximum spatial scale and density of fractures we can simulate in a practical way; determine trends in the shape and size of the DNAPL source zone in the fracture network and intrusion zones in the PM as a function of the mesh; show the effect, if any, of asperity contact bridged fracture cross flow on water and TCE mass flux; and to determine the consequences of our unstructured mesh approach to source zone architecture and outbound flux by applying different spatial discretization refinement strategies. We find that the bulk transmissivity of the aquifer and DNAPL source zone architecture are dependent on the mesh and the amount of asperity contact in the rough-walled fractures. We also find interesting, incidental results regarding the proportion of flow conducted in the fractures versus the PM.

Herein we present the governing equations and the finite-volume formulation of the numerical model. Following directly from Slough et al. [2] we derive how small volume CVs, which arise at the intersection of fractures in three dimensions, may be algebraically eliminated from the numerical system. We provide results from several field scale, 3D, two-phase simulations extended from the source zone modeling described by McLaren et al. [4] as a means to test the aspects listed above.

2.2 Theory

We present the governing equations in Section 2.2.1 and our conceptual model of discrete, rough-walled fractures in Section 2.2.2. These sections formally introduce nomenclature and spatial conceptualization necessary for subsequent topics. Section 2.2.3 provides details on the implementation of our proposed unstructured mesh generation scheme. These three topics culminate to the spatial and temporal discretization of equations in Section 2.2.4, which also includes a summary of source/sink term options. Finally, we outline the assumptions and method of fracture intersection CV elimination in Section 2.2.5, which extends the work of Slough et al. [2].

2.2.1 Governing Equations

CompFlow Bio is a numerical model that includes three mobile phases (aqueous, nonaqueous and gas) and multiple components (water, one or more oil species, air, and zero or more gas species). It uses equilibrium partitioning to transfer components between phases. A first-order accurate finite-volume approach is used to discretize the governing three-phase flow equations. Phase pressures, saturations, and component mole fractions are solved for using a fully implicit scheme. The simulator chooses time step size adaptively. *CompFlow Bio* uses a Newton-Raphson linearization method with CGStab acceleration and a block-sparse matrix data structure for the system of nonlinear differential equations. Broader sets of governing equations for *CompFlow Bio* have been reported in the literature previously in references [34, 35]. The following summarizes those applicable to a three-phase flow and three-component transport investigation.

To begin, the equation for conservation of moles of component species p is:

$$\frac{\partial}{\partial t}\left[\phi \sum_l S_l M_l X_{pl} + \rho_b K_d M_q X_{cq}\right] = -\sum_l \nabla \cdot \left(M_l X_{pl} \vec{v}_l\right) + \sum_l \nabla \cdot \left(\phi S_l \mathbb{D}_l M_l \nabla X_{pl}\right) + Q_p \tag{1}$$

The Darcy velocity is given by:

$$\vec{v}_l = -\mathbb{K}\frac{k_{rl}}{\mu_l}(\nabla P_l - \rho_l g \nabla d) \tag{2}$$

and, the dispersion tensor from Sleep and Sykes [36] has the form:

$$\phi S_l \mathbb{D}_l = \alpha_L^l \vec{v}_l \delta_{IJ} + \left(\alpha_L^l - \alpha_T^l\right)\frac{\vec{v}_{lI}\vec{v}_{lJ}}{|\vec{v}_l|} + \phi S_l \tau D_l^* \delta_{IJ} \tag{3}$$

Note that the intrinsic permeability tensor is assumed to be aligned with the principal spatial axes and thus for PM, has the form:

$$\mathbb{K} = \begin{bmatrix} k_{x_1x_1} & 0 & 0 \\ 0 & k_{x_2x_2} & 0 \\ 0 & 0 & k_{x_3x_3} \end{bmatrix} \tag{4}$$

while for fractures with effective hydraulic aperture *2b,* planar directions *I* and *J*, and with normal direction *K*, the intrinsic permeability components are given by:

$$k_{II} = k_{JJ} = \frac{(2b)^2}{12} \tag{5}$$

The above formulation leaves fifteen unknowns per CV: three saturations, S_l; nine mole fraction values, X_{pl}; and three pressures P_l. Various constraints (or simplifying assumptions) exist among the unknowns that eventually reduce the number of unknowns to three *primary variables* per control volume. Unknown values calculated via constraints are termed *secondary variables*.

The following apply to a CV in which all three phases are present. If a phase is not present, the numerical model undergoes *primary variable switching* for the affected CVs. This, as well as a description of system closure in all primary variable configurations, is given in Forsyth and Shao [37]. Beginning with unity saturation, the constraint equations are:

$$S_q + S_g + S_n = 1 \tag{6}$$

The sum of mole fractions of all components in a phase must equal unity. The system is reduced by three primary variables (one per phase) with the following:

$$\sum_p X_{pl} = 1 \tag{7}$$

Equilibrium partitioning is employed to transfer components between phases. Air is considered non-condensable and insoluble, thus it is not allowed in any phase but gas. Water is assumed to be insoluble in NAPL. Partitioning relationships reduce the number of unknowns by six. The general form of the partitioning relationship and no-partition assumptions, are:

$$X_{pl_2} = Z_{pl_2 l_1} X_{pl_1};\ X_{aq} = X_{an} = X_{wn} = 0 \tag{8}$$

where $Z_{pl_2 l_1}$ [-] is a constant or some function as described later.

Finally, constraints exist among the phase pressures due to capillarity. With experimentally determined data to parameterize the two-phase capillary pressure relationships, $P_{c,gn}$, $P_{c,gq}$ and $P_{c,nq}$, the constraint equations are:

$$\begin{aligned} P_q &= P_n - \hat{\alpha} P_{c,nq}(S_q) - (1-\hat{\alpha}) P_{c,nq}(S_q = 1) \\ P_g &= P_n + \hat{\alpha} P_{c,gn}(S_g) + (1-\hat{\alpha})\left[P_{c,gq}(S_g) - P_{c,nq}(S_q = 1)\right] \\ \hat{\alpha} &= \min\langle 1, S_n / S_n^* \rangle \end{aligned} \tag{9}$$

where $P_{c,gn}, P_{c,gq}, P_{c,nq}$ [kPa] are two-phase capillary pressure curves as functions of saturation and S_n^* [-] is a curve blending parameter.

The blending function $\hat{\alpha}$ and parameter S_n^* provide a linear transition from the two-phase gas-aqueous to the three phase gas-NAPL-aqueous capillary pressure system. This yields the correct the capillary pressure in the absence of NAPL and when NAPL is present in sufficient quantity $S_n \geq S_n^*$. The linear transition was introduced in Forsyth [38] to remove the discontinuity in the relationships proposed in Kaluarachchi and Parker [39] and Abriola and Pinder [5] that transition abruptly at a critical NAPL saturation.

Additionally, some physical quantities are functions of temperature, pressure, and/or saturation. These add to the nonlinearity of the problem:

$$M_{l\epsilon\{q,n\}} = \frac{1 + \hat{C}_l (P_l - P_{ref})}{\sum_p \left(\max\langle 0, X_{pl} \rangle / M_p^*\right)};\ M_g = \frac{P_g}{RT} \tag{10}$$

$$\rho_l = M_l \sum_p X_{pl} \omega_p \tag{11}$$

Relationships for viscosity, $\mu_l = \mu_l(T)$, equilibrium partitioning, $Z_{p,l_1,l_2} = Z_{p,l_1,l_2}(P, T, \text{etc.})$, capillary pressure, $P_{c,l_1,l_2} = P_c(S_q, S_n)$, and relative permeability, $k_{r,l} = k_{r,l}(S_q, S_n)$ are required by the model.

2.2.2 Discrete Fracture Conceptualization

The DFN framework prescribes that the void space of rough-walled fractures be modeled explicitly. We seek to capture the interactions between the rock matrix and the fracture network using physically based quantitative relationships. To represent these geologic features computationally, the domain is discretized into 3D rectilinear boxes representing matrix CVs and 2D planar rectangles representing fracture CVs. Each CV is

entirely fracture or entirely porous medium. All faces of CVs are parallel to one of the *xy*-, *yz*-, or *xz*-principal coordinate planes. Thus, all fracture intersections occur at 90° angles. Fracture intersections are captured by 1D line and 0D point CVs where two and three orthogonal fractures meet. Abutting, coplanar fractures may join to form a contiguous avenue for flow.

Figure 2-2 depicts a rough-walled fracture and surrounding matrix. This is represented by three CVs: one for the fracture and two for the matrix. The matrix CVs have physical dimensions of length, width and height, whereas fracture CVs have length and width only. Aperture is a property of the fracture. Asperity contact ratio (defined as a dimensionless factor, $0 \leq \alpha < 1$) is accounted for by dispensing a portion of the 2D fracture's surface area to allow direct contact between the adjacent matrix blocks. This reduces the intervening fracture CVs' volume and the area of communication with adjacent matrix blocks by that same factor. In Figure 2-2 the asperity contact area is depicted as a cylinder for graphical convenience, but the model does not incorporate any specific geometry internally.

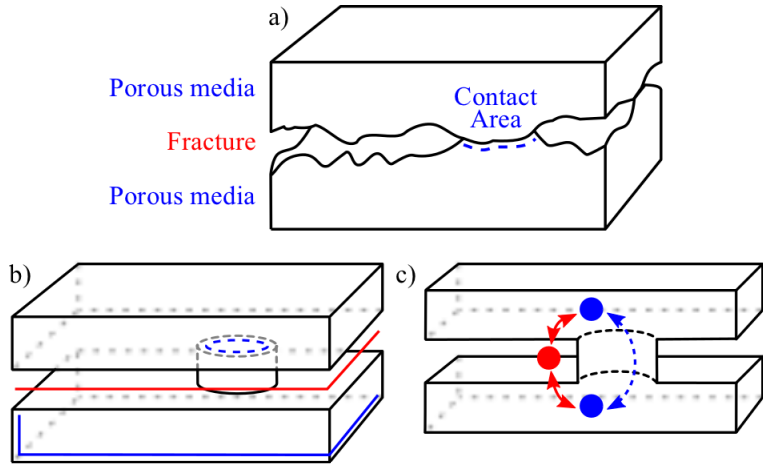

Figure 2-2 Discrete fracture conceptualization showing a) a schematic of a rough-walled fracture, b) the two dimensions of a planar fracture CV (red lines), three dimensions of a matrix CV (blue lines) and some asperity contact area (blue dashed line), and c) connection between adjacent PM blocks via asperity contact area (blue dashed arrow) and the contact of PM with the fracture CV (red arrow).

Conceptually, a fracture is formed by two parallel plates separated by some distance or aperture, *2b*. The cubic law is employed to determine the intrinsic permeability. No distinction is made between the hydraulic aperture and the mechanical aperture of a fracture, similar to the approach of Reynolds and Kueper [40]. Also, as determined in [40], the effect of fracture roughness is captured by macro-scale relative permeability and capillary pressure relationships.

Asperity contact within a real rough fracture is likely to vary spatially concomitant with fracture aperture (or fracture closure) and surface roughness properties. Asperity contact may even vary temporally caused by changes in the stress-strain conditions of the PM. For simplicity in this initial treatment, we take the asperity contact ratio parameter, α, to be constant.

2.2.3 Geometric Discretization of Fracture and Matrix CVs

The numerical model aims to allow flexibility in the location of fracture planes while maintaining a low number of CVs in the domain. Conventional "row, column and layer"-based spatial discretization schemes (i.e. regular, 3D, structured grids, such as the one in Figure 2-3) require fracture CVs to lie on and terminate at the boundaries of PM volumes. (Note that Figure 2-3 can be easily reinterpreted as a hexahedral finite-element mesh.) The boundaries of PM volumes form grid lines that are continuous across the whole domain. Greater flexibility in the location of fractures, while not inducing more fully domain-cutting grid lines, is achieved by breaking down the structured grid in areas local to fractures. This transforms the initially regular grid to an unstructured mesh of porous medium and fracture CVs.

The process of domain discretization follows four main steps: Step 1), matrix block discretization; Step 2), matrix block bisection and subdivision of fractures into fracture CVs; Step 3), fracture intersection refinement and elimination; and Step 4), addition of asperity contact connections. First, the domain is subdivided into a regular grid of recti-linear blocks with sizes given as model inputs. Second, fractures are inserted iteratively. Each insertion may cause one or more matrix and/or previously added fracture CVs to be bisected on the plane of the new fracture. The conceptual fracture is subdivided into CVs based on the boundaries of preexisting CVs. Line and point CVs are created where perpen-dicular fractures intersect one another. As an optional third step, fracture CVs may be refined outwards from fracture intersections. A schematic example of this is in Slough et al. [2], Figure 7c. The refined node size intervals are specified as model inputs. This is done to increase the spatial resolution and numerical accuracy. Fracture intersection CVs may also be eliminated during this phase. The fourth and final step is to add connections between matrix CVs across fracture planes to allow for asperity contact bridged flow.

As an example of the process above we describe insertion of a non-fully crosscutting fracture as shown in Figure 2-4. Step 1): CVs A and B are created from model inputs. Step 2): A is then split into A' and A" and new connections to B are formed based on the new interfacial areas. The fracture is contained entirely within the original A, so it does not need to be subdivided. The fracture becomes node C. Connections C to A' and C to A'' are made. The connection A' to A" is first constructed as the interface area not obstructed by C. Step 3): does not apply here. Step 4): the A' to A" connection becomes the sum of the unobstructed area plus the asperity contact area through C (provided that $\alpha \neq 0$).

Other more complicated fracture insertion scenarios exist because of different configurations of preexisting PM and fracture CVs (e.g. in Figure 2-4, consider possibilities for a vertical fracture that bisects A'). As a result: CVs may have many neighbours on each face and hence the mesh we form is unstructured; and fractures are subdivided based on the most refined CVs surrounding them and thus the resultant mesh is highly dependent on the order in which fractures are inserted. We omit many tedious cases that must be considered when inserting/subdividing fractures and building the mesh. However, neighbour relationships in the final unstructured mesh are defined by the existence of some contiguous face area between two CVs.

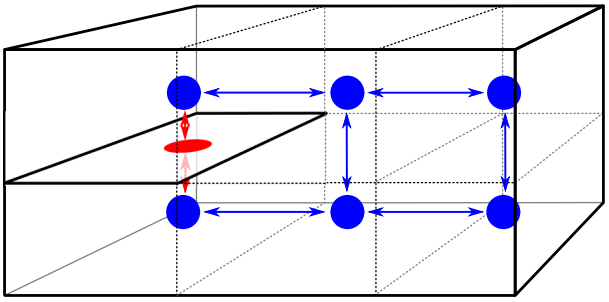

Figure 2-3 Schematic diagram of a conventional discrete fracture network control volume discretization with six porous media control volumes and one fracture control volume.

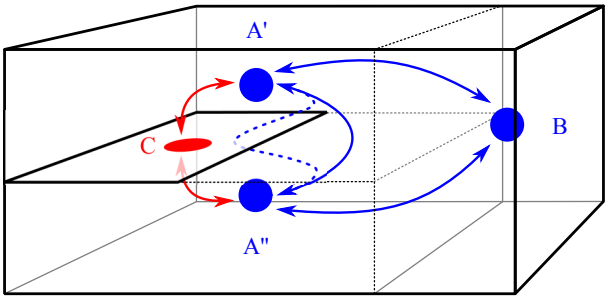

Figure 2-4 Schematic diagram of three matrix control volumes, *A'*, *A''*, and *B*, one fracture control volume, *C*, and all associated connections. The connection between *A'* and *A''* is the sum of direct contact area (solid blue arrow), plus the asperity contact area through *C* (dashed blue arrow).

To begin describing how interface areas are calculated, we first consider the volume of PM or fracture CVs. In general, the CV with index *i* has spatial dimensions $\Delta x_{1,i}$, $\Delta x_{2,i}$ and $\Delta x_{3,i}$ [m] aligned with the principal Cartesian axes, x_1, x_2 and x_3. Thus, its volume is given by:

$$V_i = \begin{cases} \Delta x_{1,i}\Delta x_{2,i}\Delta x_{3,i} & \text{for porous media} \\ 2b_i\Delta x_{I,i}\Delta x_{J,i}(1-\alpha) & \text{for fractures} \end{cases} \tag{12}$$

where V_i [m^3] is the volume of CV *i*; I and J are Cartesian directions, $I, J \epsilon \{1,2,3\}$ with $I \neq J$; and $2b$ [m] is fracture aperture. We reduce a fracture CV's volume in proportion to the asperity contact area, α, referring to the schematic in Figure 2-2b.

Interfacial area is a crucial piece of information for use in *influence coefficients*. We quantify this area in equation (13). This expression has several calculation options that we illustrate with examples. Interfacial areas are calculated using pairings of Δx_1, Δx_2 and Δx_3, but care is taken to handle cases where faces of two CVs are not congruent, such as A'-B in Figure 2-4, and where fractures partially obstruct the interface of two matrix CVs, such as A'–A":

$$A_{ij} = \begin{cases} \Delta x_I \Delta x_J & \text{for congruent faces} \\ \left(\Delta x_{I,i} \cap \Delta x_{I,j}\right)\left(\Delta x_{J,i} \cap \Delta x_{J,j}\right) & \text{for incongruent faces} \\ \min\langle 2b_i, 2b_j\rangle\left(\Delta x_{I,i} \cap \Delta x_{I,j}\right) & \text{for incongruent abutting fractures} \\ (1-\alpha)A_{ij} & \text{for fracture-matrix interfaces} \\ A_{ij} - (1-\alpha)\sum_{\forall f}\left[\bigcap_{k=\{i,j,f\}} \Delta x_{I,k} \bigcap_{k=\{i,j,f\}} \Delta x_{J,k}\right] & \text{otherwise} \end{cases} \tag{13}$$

where A_{ij} [m^2] is the interface area between CVs with indices *i* and *j*; f is one of possibly several fracture CVs that partially obstruct the *i-j* interface; and ∩ is an operator for the overlap of like dimensions of two CVs in [m].

Though the idea of interfacial area is trivial, a great deal of bookkeeping is imposed by the unstructured mesh. Figure 2-5 illustrates each case of equation (13). Figure 2-5a depicts the trivial case of two congruent CV faces is in where ⓪ $= \Delta x_{2,i} = \Delta x_{2,j}$ and ① $= \Delta x_{3,i} = \Delta x_{3,j}$ and $A_{ij} =$ ⓪×①. Figure 2-5b shows a case where faces are incongruent in the x_2-direction only and we have ② $= \left(\Delta x_{2,k} \cap \Delta x_{2,l}\right) = \Delta x_{2,l}$ and ③ is the same as ①. In Figure 2-5c, we have the case of two incongruent abutting fractures. Here,

④ $= \Delta x_{2,f1} \cap \Delta x_{2,f2}$ for which overlapping distance is found by subtracting the ending x_2-coordinate of f_2 from the starting x_2-coordinate of f_1, and the two fracture apertures are used in calculating ⑤ $= \min\langle 2b_{f1}, 2b_{f2} \rangle$. Figure 2-5d shows the interface area between an incongruent fracture and a matrix CV with $A_{mf} = (1-\alpha)$⑥×⑦, where ⑥ and ⑦ are each calculated as a simpler case of distance ④ and we multiply by a ratio complementary to the asperity contact area as per Figure 2-2c. Note that $A_{mf} \neq A_{nf}$. A final example showing two incongruent matrix CVs with one partially obstructing fracture is also in Figure 2-5d. Here, we wish the interfacial area between *m* and *n* to be the sum of the area of direct contact area plus the asperity contact area through *f*. This can be expressed equivalently by taking the entire matrix-matrix interface area and subtracting the area of the obstructing fracture: $A_{mn} =$ ⑧×⑨ $-(1-\alpha)$⑥×⑦ with ⑥ $= \Delta x_{2,m} \cap \Delta x_{2,f} \cap \Delta x_{2,n} = \Delta x_{2,n}$, ⑦ $= \Delta x_{3,m} \cap \Delta x_{3,f} \cap \Delta x_{3,n} = \Delta x_{3,f}$, and ⑧ and ⑨ are analogous to ④. The advantage of using a subtraction of obstructing fracture interface areas becomes evident as more fractures obstruct a matrix-matrix interface and the pattern of the direct contact area becomes irregular, as may be the case if f_1 and f_2 were to obstruct *m* and *n*.

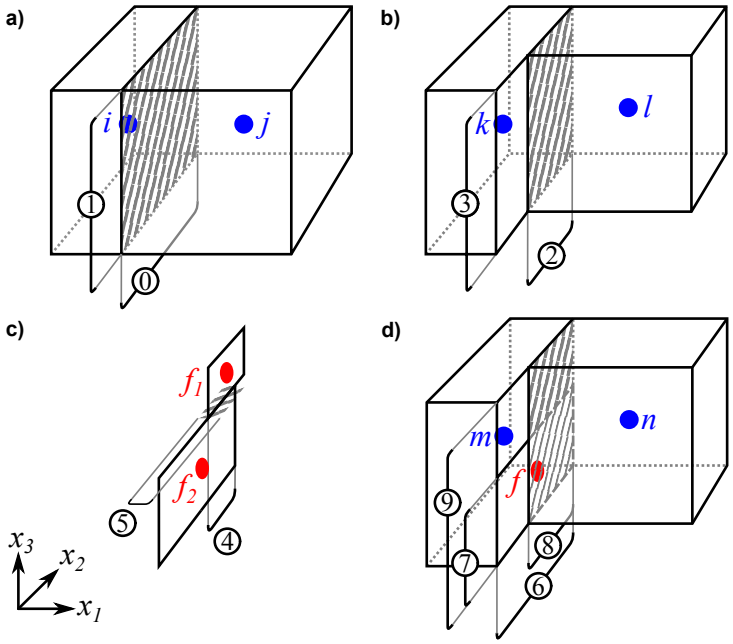

Figure 2-5 Five examples of interface area calculations with a) congruent CV faces, b) incongruent faces, c) abutting, incongruent fracture CVs with different apertures, and d) incongruent fracture-matrix interfaces and incongruent matrix CVs with their interface partially obstructed by a fracture.

In the third case of equation (13), we take the minimum of the apertures $2b_i$ and $2b_j$ because we assume a step-like narrowing of the void area from the larger to the smaller fracture and neglect any other flow effects.

2.2.4 Numerical Formulation

When discretized using first-order accurate time and spatial derivatives to capture the molar flux of component *p* from CV *i* to neighbour *j*, equation (1) becomes:

$$\begin{aligned}
&\frac{V_i B_i}{\Delta t^{N+1}}\left\{\left[\sum_l \phi S_{l,i} M_{l,i} X_{pl,i} + \rho_b K_{d,i} M_{q,i} X_{pq,i}\right]^{N+1}\right. \\
&\left. - \left[\sum_l \phi S_{l,i} M_{l,i} X_{pl,i} + \rho_b K_{d,i} M_{q,i} X_{pq,i}^1\right]^{N}\right\} \\
&= \sum_{j\epsilon\eta_i}\sum_l \left[\gamma_{ij}\lambda_{l,\mathrm{ups}\langle i,j\rangle}\Gamma_{l,ij}^{N+1} X_{pl,\mathrm{ups}\langle i,j\rangle}^{N+1} + \gamma_{ij}^* S_{l,ij}^{N+1} M_{l,\mathrm{ups}\langle i,j\rangle}^{N+1}\left(X_{pl,j}^{N+1} - X_{pl,i}^{N+1}\right)\right] \\
&+ Q_{p,i}^{N+1}
\end{aligned} \tag{14}$$

The fluid potential difference [kPa] between *i* and *j* is given as follows. We note the need for an appropriate choice for the datum to avoid nullifying the buoyancy term.

$$\Gamma_{l,ij}^{N+1} = \Gamma_{l,j}^{N+1} - \Gamma_{l,i}^{N+1} = \left(P_{l,j}^{N+1} - \rho_{l,j}^{N+1} d_j g\right) - \left(P_{l,i}^{N+1} - \rho_{l,i}^{N+1} d_i g\right) \tag{15}$$

The *influence coefficient* for the advective flux, γ_{ij}, is a term that bundles together several temporally static physical and geometric properties for repeated use in calculations. For the pair *i* and *j*, γ_{ij} is:

$$\gamma_{ij} = A_{ij}\frac{k_{II,i}k_{II,j}\left(\Delta x_{I,i} + \Delta x_{I,j}\right)}{k_{II,j}\Delta x_{I,i} + k_{II,i}\Delta x_{I,j}}\left(\frac{\Delta x_{I,i} + \Delta x_{I,j}}{2}\right)^{-1} \tag{16}$$

where *I* is the vector component normal to the *i-j* interface. The *influence coefficient* of the diffusive flux, γ_{ij}^*, is:

$$\gamma_{ij}^* = \alpha_{L,ij}^l v_{l,L,ij}^N + \alpha_{TH,ij}^l v_{l,TH,ij}^N + \alpha_{TV,ij}^l v_{l,TV,ij}^N + \phi D_l^* \tau \tag{17}$$

which is lagged in time with respect to phase velocity, $\vec{v}_{l,ij}^N$, at the interface. Vector components in the longitudinal and transverse directions are calculated by scalar projections onto the interface normal vector.

Source/sink terms are the first of two currently implemented ways to create *boundary conditions* (BC) in the numerical model. (Herein, 'boundary condition' does not take the term's more strict mathematical definition. Rather, it represents some hydraulic constraint imposed on a CV or a group of CVs.) Values for the term $Q_{p,i}^{N+1}$ [mol/d] for component *p* can be calculated in one of several ways depending on the hydraulic constraint the modeler wishes to impose. Here, we describe expressions for a *constant rate component injector*, *hydrostatic boundary*, *gas boundary*, and a *recharge boundary*.

Constant rate component injector source terms, which inject a component at a prescribed rate up to a maximum pressure threshold in their containing CVs, are defined as:

$$Q_{p,i}^{N+1} = \begin{cases} \hat{Q}_{p,BC} & \text{if } \hat{Q}_{l,BC} < \gamma_{i,BC}\lambda_{l,BC}\left(\hat{P}_{\max,BC} - P_{l,i}^{N+1}\right) \\ \gamma_{i,BC}\lambda_{l,BC}\left(\hat{P}_{\max,BC} - P_{l,i}^{N+1}\right)\hat{X}_{p,BC} & \text{otherwise} \end{cases} \quad (18)$$

where $\hat{Q}_{p,BC}$ [mol/d] is the user defined molar injection rate of component *p*; $\hat{Q}_{l,BC}$ [mol/d] is injection rate of phase *l*, calculated as the sum of $\hat{Q}_{p,BC}$ for which *p* is in *l*; $\hat{X}_{p,BC} = \hat{Q}_{p,BC}/\hat{Q}_{l,BC}$ is the mole fraction of *p* being injected in *l*; and $\hat{P}_{\max,BC}$ [kPa] is the maximum injection pressure.

Hydrostatic boundary source/sink terms inject or remove multiple components to keep the CV at a predefined pressure. Below the water table this source/sink term models pressure equilibrium between a fictitious well bore and the adjoining aquifer. It is defined as:

$$Q_{p,i}^{N+1} = \sum_{l} \begin{cases} \gamma_{i,BC}\lambda_{l,BC}\left(P_{l,BC}^{N+1} - P_{l,i}^{N+1}\right)X_{pl,BC} & \text{if } l = q \text{ and } P_{l,i}^{N+1} < P_{l,BC}^{N+1} \\ \gamma_{i,BC}\lambda_{l,i}^{N+1}\left(P_{l,BC}^{N+1} - P_{l,i}^{N+1}\right)X_{pl,i}^{N+1} & \text{if } P_{l,i}^{N+1} > P_{l,BC}^{N+1} \\ 0 & \text{otherwise} \end{cases} \quad (19)$$

where $\gamma_{i,BC} = 2\pi b_{BC}\Delta x_{i,I}\sqrt{k_{i,JJ}k_{i,KK}}/\log\left(0.37\sqrt{V_i/(\pi\Delta x_{i,I})}/r_w\right)$ [m³] is an influence coefficient combining the radius r_w [m] of the "well bore" with CV *i*'s spatial dimensions and permeability at the given source/sink efficiency. The first criterion applies when the well bore is under pressurized relative to the adjoining aquifer causing injection of all components within the BC-defined aqueous phase. This is the only phase for which positive $Q_{p,i}^{N+1}$ terms exist. The second criterion removes all components from the aqueous,

NAPL, or gas phase(s). Gas boundaries above the water table are implemented in a similar manner, except the gas phase $l = g$ is used in the first pressure criterion.

Recharge boundaries are implemented by multiple instantiations of the constant rate component injection boundary. Each CV in this boundary holds a source term that injects a component at a rate commensurate with the CVs surface area and the infiltration rate of the aqueous phase.. For example, given the aqueous phase composition, $\hat{X}_{cq,BC}$, rate of recharge in [mm/d], and $\hat{P}_{\max,BC}$, then $\hat{X}_{wq,BC} = 1 - \hat{X}_{cq,BC}$, $\hat{Q}_{c,BC}$, and $\hat{Q}_{w,BC}$ are calculated internally using the upward facing area of the CV. The influence coefficient is $\gamma_{i,BC} = 2b_{BC}\Delta x_{i,J}\Delta x_{i,K}k_{i,II}/\Delta x_{i,I}$.

A final use of the $Q_{p,i}^{N+1}$ term is the *air penalty source term*. This term helps the numerical system converge by injecting small amounts of the air component to avoid non-physical solutions with S_g<0 or X_{ag}<0 during Newton iteration. This is discussed by Forsyth, et al., in references [34, 41]. Alternatives to this method, including removing the equation for the gas phase when below the water table, are discussed in [42]. However, we rely on their result stating that these alternatives come at a greater computational expense. Our source term is a variation on Equation 27 in reference [34] and is given by:

$$Q_{a,i}^{N+1} = \begin{cases} V_i B_i \phi M_g \left(S_g^* - S_g^{N+1}\right)^2 / \Delta t^{N+1} & \text{if } S_g^{N+1} < S_g^* \\ 0 & \text{otherwise} \end{cases} \tag{20}$$

The second of the two BC types is the *invariant property boundary.* It is implemented by setting $B_i = 10^6$, or some other suitably large number. This parameter, which appears on the left-hand side of equations (14) and (20), artificially over-represents the host CVs volume causing any flux in or out (i.e. terms on the right hand side of equation (14)) to be insignificant. This effectively maintains constant pressure and composition in the host CV.

Relative permeability and capillary pressure relationships are read in to the model from tabular data (see for example Tables 2 and 3 in [43]). The benefit to tabular inputs is that they allow the underlying k_r-S or P_c-S functional relationships to be substituted at will, without modification to the model's source code. However, attention must be given when interpolating between the discrete data points in the tables. Our experience suggests that linear interpolation is sufficient except near residual saturation in the k_r-S curves. Residual saturation of a phase is determined by the first non-zero relative permeability entry in the table. A phase is immobile, $k_{rl} = 0$, in the range $S_l \epsilon [0, S_{lr})$ and it is mobile, $k_{rl} > 0$, in the

range $S_l \epsilon [S_{lr}, 1]$. Linear interpolation may cause the simulation to fail or be driven to very small time steps due to "flip-flopping" (i.e. a phase alternates between mobile and immobile states in successive Newton iterations). In the current implementation, we take great care in smoothing this problematic region. This is accomplished by splicing-in an ad hoc transformed cosine curve, $k_{rl} = k_{rl}(\hat{S}_{\text{smooth}})\left[1 - \cos\left(\pi(S_l - S_{lr})/(\hat{S}_{\text{smooth}} - S_{lr})\right)\right]/2$, on the interval $S_l \epsilon [S_{lr}, \hat{S}_{\text{smooth}}]$. $\hat{S}_{\text{smooth}}$ [-] is an arbitrary parameter chosen to be greater than the shift value used for computing numerical derivatives in saturation, but less than the residual saturation of the phase.

2.2.5 Algebraic Development of Fracture Node Elimination

In order to adequately represent domains and fracture spacing at our scale of interest (~100 m in size with multiple fractures per metre) and maintain tractability of the simulation, it is necessary to remove the small volume nodes at the intersection of fracture planes. Slough et al. [2] asserted that small volume nodes negatively impact simulation time steps. To resolve this issue, Slough et al. proposed that they can be algebraically eliminated from the numerical system under the assumption that these small volume nodes are at steady state (i.e. inflow is equal to outflow). We now proceed by developing flow equations in a manner parallel to [2], but we add a clear extension to 3D fracture intersections in order to support the objectives of this work. For 3D fracture intersections, the process occurs in two steps: elimination of point (i.e. 0D) intersections, followed by elimination of line (i.e. 1D) intersections. Ultimately, this process creates new neighbours and new influence coefficients for each fracture CV adjacent to an intersection.

For simplicity, consider the case of advective flow between a fracture node pair *i-j*. The volumetric flow rate of phase *l* is given by:

$$F_{l,ij} = \gamma_{ij} \lambda_{l,ups\langle i,j \rangle} (\Gamma_{l,j} - \Gamma_{l,i}). \tag{21}$$

Relying on the assumption of steady-state advective flow in CV *i*, we have:

$$\sum_{j \epsilon \eta_i} F_{l,ij} = 0. \tag{22}$$

Figure 2-6 depicts the arrangement of three orthogonal fractures intersecting to form one point intersection and three line intersections. This example is general and can be

extended to cases involving through-going fractures. Node *a* must be eliminated first, followed by *b*, *c*, then *d*. The final result gives flow relationships between CVs *E, F,* and *G* with the physical and geometric properties of *a*, *b*, *c* and *d* embedded in the new influence coefficients.

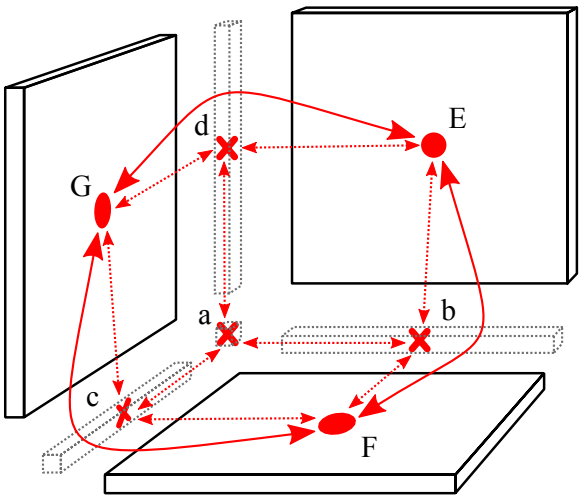

Figure 2-6 Control volumes at the intersection of three fractures: point node *a*; line nodes *b*, *c* and *d*; and 2D fracture planes *E*, *F* and *G*. Control volumes are separated spatially for clarity.

Combining equation (21) and (22), and taking the specific case of node *a* with η_a = {*b, c, d*}, we may rearrange them to obtain:

$$\Gamma_{l,a} = \frac{\sum_{j\epsilon\eta_a} \gamma_{aj}\lambda_{l,ups\langle a,j\rangle}\Gamma_{l,j}}{\sum_{j\epsilon\eta_a} \gamma_{aj}\,\lambda_{l,ups\langle a,j\rangle}} \tag{23}$$

Thus, reusing equation (21), flow from *a* to a specific neighbour *k* can be rewritten as:

$$F_{l,ak} = \gamma_{ak}\lambda_{l,ups\langle a,k\rangle}\left(\Gamma_{l,k} - \frac{\sum_{j\epsilon\eta_a} \gamma_{aj}\lambda_{l,ups\langle a,j\rangle}\Gamma_{l,j}}{\sum_{j\epsilon\eta_a} \gamma_{aj}\lambda_{l,ups\langle a,j\rangle}}\right) \tag{24}$$

$$F_{l,ak} = \frac{\gamma_{ak}\lambda_{l,ups\langle a,k\rangle}}{\mu_l \sum_{j\epsilon\eta_a} \gamma_{aj}\lambda_{l,ups\langle a,j\rangle}}\left(\Gamma_{l,k}\sum_{j\epsilon\eta_a} \gamma_{aj}\lambda_{l,ups\langle a,j\rangle} - \sum_{j\epsilon\eta_a} \gamma_{aj}\lambda_{l,ups\langle a,j\rangle}\Gamma_{l,j}\right) \tag{25}$$

For clarity, expanding the bracketed term in equation (25) yields:

$$\frac{\begin{array}{c}\gamma_{aj_1}\lambda_{l,ups\langle a,j_1\rangle}\Gamma_{l,k} + \cdots + \gamma_{ak}\lambda_{l,ups\langle a,k\rangle}\Gamma_{l,k} + \cdots + \gamma_{aj_n}\lambda_{l,ups\langle a,j_n\rangle}\Gamma_{l,k} \\ - \quad \gamma_{aj_1}\lambda_{l,ups\langle a,j_1\rangle}\Gamma_{l,j_1} + \cdots + \gamma_{ak}\lambda_{l,ups\langle a,k\rangle}\Gamma_{l,k} + \cdots + \gamma_{aj_n}\lambda_{l,ups\langle a,j_n\rangle}\Gamma_{l,j_n}\end{array}}{\gamma_{aj_1}\lambda_{l,ups\langle a,j_1\rangle}(\Gamma_{l,k} - \Gamma_{l,j_1}) + \cdots + \gamma_{ak}\lambda_{l,ups\langle a,k\rangle}(\Gamma_{l,k} - \Gamma_{l,k}) + \cdots + \gamma_{aj_n}\lambda_{l,ups\langle a,j_n\rangle}(\Gamma_{l,k} - \Gamma_{l,j_n})}$$

$$F_{l,ak} = \frac{\gamma_{ak}\lambda_{l,ups\langle a,k\rangle}}{\sum_{j\epsilon\eta_a}\gamma_{aj}\lambda_{l,ups\langle a,j\rangle}} \sum_{j\epsilon\eta_a} \gamma_{aj}\lambda_{l,ups\langle a,j\rangle}\left(\Gamma_{l,k} - \Gamma_{l,j}\right)$$

$$F_{l,ak} = \sum_{j\epsilon\eta_a}\left[\frac{\gamma_{aj}\lambda_{l,ups\langle a,j\rangle}\gamma_{ak}\lambda_{l,ups\langle a,k\rangle}}{\sum_{j^*\epsilon\eta_a}\gamma_{aj^*}\lambda_{l,ups\langle a,j^*\rangle}}\right]\left(\Gamma_{l,k} - \Gamma_{l,j}\right) \tag{26}$$

where j is the index of the outer summation and j^* is the index of the inner summation.

Recall the assumption of steady state flow, which implies that the fluid mobility terms are constant. At this point, another assumption must be made to simplify this expression for practical application in the numerical model: that the phase mobility terms are all equal. This is not desirable, but a second approximation can reintroduce upstream weighting of the mobility term:

$$F_{l,ak} \cong \sum_{j\epsilon\eta_a}\underbrace{\left[\frac{\gamma_{aj}\gamma_{ak}}{\sum_{j^*\epsilon\eta_a}\gamma_{aj^*}}\right]}_{:=\gamma'_{jk}}\lambda\left(\Gamma_k - \Gamma_j\right) \cong \sum_{j\epsilon\eta_a}\gamma'_{jk}\lambda_{l,ups\langle j,k\rangle}\left(\Gamma_k - \Gamma_j\right) = \sum_{j\epsilon\eta_a} F_{l,jk} \tag{27}$$

Equation (27) finally shows that the flow across an eliminated node can be calculated directly with the new *influence coefficient*:

$$\gamma'_{jk} := \frac{\gamma_{aj}\gamma_{ak}}{\sum_{j\epsilon\eta_a}\gamma_{aj}} \tag{28}$$

which is appropriate for any two neighbours of the eliminated node, a. With a algebraically eliminated, the neighbour set of b expands from $\eta_b = \{a, E, F\}$ to $\eta_b = \{c, d, E, F\}$ with:

$$\gamma'_{bc} := \frac{\gamma_{ab}\gamma_{ac}}{\gamma_{ab} + \gamma_{ac} + \gamma_{ad}}, \gamma'_{bd} := \frac{\gamma_{ab}\gamma_{ad}}{\gamma_{ab} + \gamma_{ac} + \gamma_{ad}}, \text{ and } \gamma'_{cd} := \frac{\gamma_{ac}\gamma_{ad}}{\gamma_{ab} + \gamma_{ac} + \gamma_{ad}}$$

Under the same presuppositions, the algebraic manipulation may be repeated on node *b.* Deletion of b produces a new influence coefficient between E and F. Making direct use of the result in (28), we have:

$$
\begin{aligned}
\gamma''_{EF} &:= \frac{\gamma_{bE}\gamma_{bF}}{\sum_{j\epsilon\eta_b}\gamma_{bj}} \\
&= \frac{\gamma_{bE}\gamma_{bF}}{\gamma_{bE}+\gamma_{bF}+\gamma'_{bc}+\gamma'_{bd}} \\
&= \frac{\gamma_{bE}\gamma_{bF}}{\gamma_{bE}+\gamma_{bF}+\frac{\gamma_{ab}\gamma_{ac}}{\gamma_{ab}+\gamma_{ac}+\gamma_{ad}}+\frac{\gamma_{ab}\gamma_{ad}}{\gamma_{ab}+\gamma_{ac}+\gamma_{ad}}}
\end{aligned}
\tag{29}
$$

Due to the generality of our derivation, expression (29) can be applied to any of the node pairs *EF*, *FG* or *EG*. Thus, all the small volume intersection nodes may be removed from the system, leaving only the 2D fracture planes in Figure 2-6 and their associated connections.

The velocity term for use in the diffusive flux between *i* and *j* is calculated in two steps. First, node centred velocities are calculated for *i* and *j* individually. A node-centred velocity is based the fluxes over each boundary of a CV. Second, a volume weighted average is taken of these two node centred velocities. We use this average because connections across an eliminated node do not have a spatially well defined interface.

2.3 Application

To demonstrate the practical capability of our new mesh generator and asperity contact formulation, we apply it to a "real world" problem based on the Smithville site modeling effort of Slough et al. [3] and more recently by McLaren et al. [4]. Both these studies use a 2D fractured rock domain with an intermediate fracture density (spacing on the order of 1 m) at a spatial scale relevant to their NAPL source zone investigation (on the order of 100 m). They restrict the simulation to the saturated zone (i.e. only aqueous and nonaqueous phases). We retain this conceptual set up (which is somewhat simplified compared to the three-phase equations presented previously) so we can explore the limit to size and number of CVs in a 3D domain. Our limit is not strictly bounded; it is the maximum size/number of CVs with which we expect to achieve a complete simulation run in a "reasonable" amount of time. Additionally, this conceptual set up allows us to judge the effects of fracture cross flow via asperity contact bridges in simplified one- and two-phase scenarios.

We structure the following by: introducing the domain; discussing findings regarding mesh scalability; presenting simulation results focusing on the effect of the unstructured

mesh and asperity contact on the spatial extent of the NAPL source zone; and finally, by presenting water and TCE mass fluxes at a transverse control plane.

2.3.1 Field Scale Simulation Domain

The domain is 200×50×43 m in length, transverse width and height relative to the ambient groundwater flow direction. We arrived at the length and width dimensions by trial and error. The domain's six horizontally layered stratigraphic units are pictured in Figure 2-7a. These consist of fractured clay overburden, a thin layer of sandy till, and four layers of fractured dolostone bedrock. Each unit has its own distinct thickness, porosity, hydraulic conductivity, set of k_r-S and P_c-S relationships, and set of fracture network statistical parameters. The matrix has conductivity values of 8.0×10^{-9}, 8.0×10^{-8} and 8.0×10^{-6} m/s in the tight, permeable and weathered dolostone units, respectively. Porosity is 0.03, 0.03 and 0.15 in the same units, and is 0.5 in the clay. Slough et al. [3] describe in detail the site-specific and literature data sources of the preceding parameters. The parameters for the 2D DFN defined in McLaren et al. [4], Table 4, apply here with x-direction values analogously reapplied in the y-direction to form the 3D DFN. Due to parameterization by stratum, few vertical fractures span more than one unit. Furthermore, x- and y-direction fracture length parameters are greater than those in the z-direction. Thus the fracture network is anisotropic and favours horizontal flow via the longer continuous discrete features.

A single DFN realization is reused in a suite of simulations in which we vary the asperity contact ratio and the fracture network and/or matrix discretizations. Three asperity contact ratio values are applied to each of three unstructured meshes (nine simulations in total). The three meshes are: 1) 'Base,' a coarse initial discretization of the PM (5×5×1 m blocks) that are subsequently transformed upon DFN integration; 2) 'FIRef,' the same coarse PM discretization but with refinement at fracture intersections (0.1 m-sized CVs oriented radially from each fracture intersection); and 3) 'Ref,' a finer initial discretization of the PM (2.5×2.5×1 m blocks) that also causes a finer fracture network discretization. The three asperity contact ratios are α = 0.0, 0.1 and 0.2. The latter two have more connections (i.e. more nonzero off-diagonal terms in the matrix-vector numerical system of equations) than the former. For anecdotal information on the computational size of the meshes, Table 2-1 gives the number of CVs in each mesh and Table 2-2 gives the approximate sizes of the matrix-vector system (noting that each "block" is a 3×3 sub-

matrix). Figure 2-7b shows fracture apertures and fracture CVs of the Base scenario in the downgradient 150 m portion of the fracture network. This realization contains approximately 1900 conceptual fractures that are discretized into 190,000 final fracture CVs. This count excludes 13,000 point intersection and 88,000 line intersection CVs removed in the algebraic node elimination step. The original 40×10×43 = 17,200 CV grid of regularly sized rectilinear PM blocks became an unstructured mesh of 129,000 PM CVs.

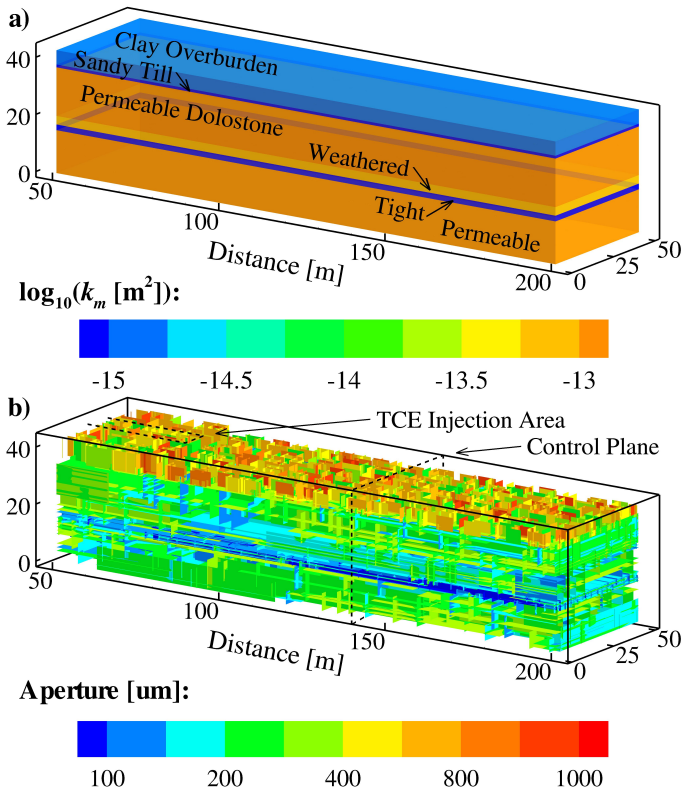

Figure 2-7 The 200×50×43 m Smithville simulation domain: a) stratigraphy (after Slough et al. [3], Figure 5), and b) discrete fracture network.

After the numerical model reaches a pseudo-steady state with respect to the ambient groundwater flow, nonaqueous phase TCE is steadily released at the top of the domain over a 50×10 m area in the upgradient portion of the domain for a period of one year. This DNAPL release zone size is reduced from the 50×50 m area estimated by Golder Associates Ltd. [44] so that, for the purposes of this demonstration, the width of the source area does not span the entire width of the domain. The simulation continues for 100 years past DNAPL loading to allow further source zone evolution, dissolution, and plume migration.

Partial results of the FIRef simulations are presented in the figures and discussion that follows. These were abandoned after 1.5 months (about 100 simulated days) due to long projected run times.

Table 2-1 Comparison of number of CVs in the three unstructured meshes (in 1000s).

	Base	**Ref**	**FIRef**
Initial PM Discretization	17	69	17
PM Discretization*	129	264	129
Fracture Discretization	191	293	640**
Frac. Int. CVs Eliminated	101	121	101

*After porous media CV bisection
**After adding refinement at fracture intersections

Table 2-2 Comparison of number of matrix blocks and symmetric off-diagonal matrix entries for nine unstructured meshes (in 1000s).

	Blocks	**Off-Diag.s**
Base-α=0.0	320	1,331
Base-α=0.1,0.2	320	1,493
Ref-α=0.0	557	2,116
Ref-α=0.1,0.2	557	2,376
FIRef-α=0.0	768	4,388
FIRef-α=0.1,0.2	768	4,551

2.3.2 Mesh Scalability

To exemplify the effectiveness of the localized node bisection technique in reducing the total number of CVs in the domain we contrast the mesh in the realization above with hypothetical meshes employing the traditional discretization technique (recall Figure 2-3 versus Figure 2-4). In the extreme end member where we do not compromise in the 1 mm resolution of the random fracture size and location – 1 mm is the arbitrary resolution of our fracture generator – a regular grid to accommodate this realization would have about 1200×360×140 grid lines. This would yield over 60,000,000 matrix CVs prior to incorporating the discretized fracture CVs. In a more moderate case, supposing that random fracture size and location were rounded to the nearest 1 m, the number of matrix CVs would total 430,000. These examples represent different choices in the tradeoff decision

between computational time versus numerical accuracy and restriction on the density of the fracture network.

The FIRef-α=0.1 and FIRef-α=0.2 are the largest simulations (in terms of number of CVs and connections) attempted with this version of *CompFlow Bio* to date. These are beyond what we can model in a practical way (in terms of computational time) given our current computational resources and use thereof. This limit may be increased in the future by employing parallel computing. The tractability of a given simulation is not only governed by the number of CVs but also by the complexity of the physical system. These simulations carry the calculative burden of three-phase flow but are essentially two-phase flow problems. If we were to introduce a vadose zone (i.e. a non-negligible gas phase) at this scale, the limit on permissible number of CVs would be drastically reduced. Because the gas phase is highly mobile and is a host for water and TCE vapour, including it would increase the nonlinearity in the numerical system; we suspect this would yield intractable simulations with this number of CVs. Anecdotally the Base, Ref, and FIRef simulations take approximately one month, 1.5 months, and presumably many months, respectively, using a consumer grade, 3.3 GHz CPU computer.

2.3.3 DNAPL Source Zone and Plume

Spatial plots of nonaqueous phase saturation (S_n) in the simulations with zero asperity contact ratio are shown in Figure 2-8 and Figure 2-9. They show S_n at 3 months and 1 year of NAPL injection, respectively. A detailed inspection shows that most of the free-phase contaminant resides in the fracture network. Some NAPL imbibes into the rock matrix in isolated pockets as highlighted in the right-hand panels. The Ref simulation has the advantage of general refinement, whereas the FIRef has the advantage of specific refinement in the fracture network. Thus, they are subject to varying amounts of spatial numerical error. The adaptive time stepping scheme produced similar trends in time step magnitude for each case; temporal error is approximately equal. Contrasting the panels of Figure 2-8 and of Figure 2-9 we observe differences in the source zone shape, length, and presumably the internal S_n distribution. Base shows the most extensive source zone and FIRef shows the least extensive zone despite the same total amount of TCE mass in the domain (see Figure 2-11a).

Figure 2-10 shows the Base scenario's dissolved contaminant plume in the fracture network (Panel a) and in the rock matrix (Panel b) at the end of TCE loading (365 days). We observe extensive downgradient transport and transverse dispersion of the plume. Ten times more TCE mass exists as a dissolved species in the aqueous phase than exists as a NAPL at this time (see Figure 2-11a).

Considering now the simulations with other asperity contact ratio values, S_n and dissolved plume results are qualitatively similar to their counterparts in Figure 2-8 through Figure 2-10. Thus, we omit them. One noteworthy trend is increasing source zone extent in the fracture network with increasing asperity contact ratio. Increasing α decreases the area available for fracture-matrix interaction. Less TCE-laden aqueous phase leaves the fracture network hence less TCE NAPL dissolves.

Figure 2-11 shows the distribution of TCE mass: Panel a) in fractures and in total; and Panel b) in the aqueous phase compared to the nonaqueous phase. Figure 2-11a shows that in all simulation cases the TCE dissolves out of the fracture network after about 10 years. Animations of spatial S_n plots reveal that the upgradient portions of the source zone dissolve first, which is consistent with fresh water flushing. The relatively short 10-year period it takes for complete dissolution from fractures is contrasted by the persistence of NAPL that imbibed into the matrix (recall the isolated pockets in Figure 2-9). Figure 2-11b shows that these pockets last ~20 years (~8000 d) and ~50 years (~18,000 d) in the Base and Ref simulations, respectively. Due to equilibrium partitioning, the time it takes for NAPL to dissolve from the matrix is related to the rate at which fresh water flushes over the source areas. Although the hydraulic gradient driving fresh water is the same for all simulations, we find that the bulk hydraulic conductivity is not the same. This disparity must be caused by the mesh, which we discuss further in the following section.

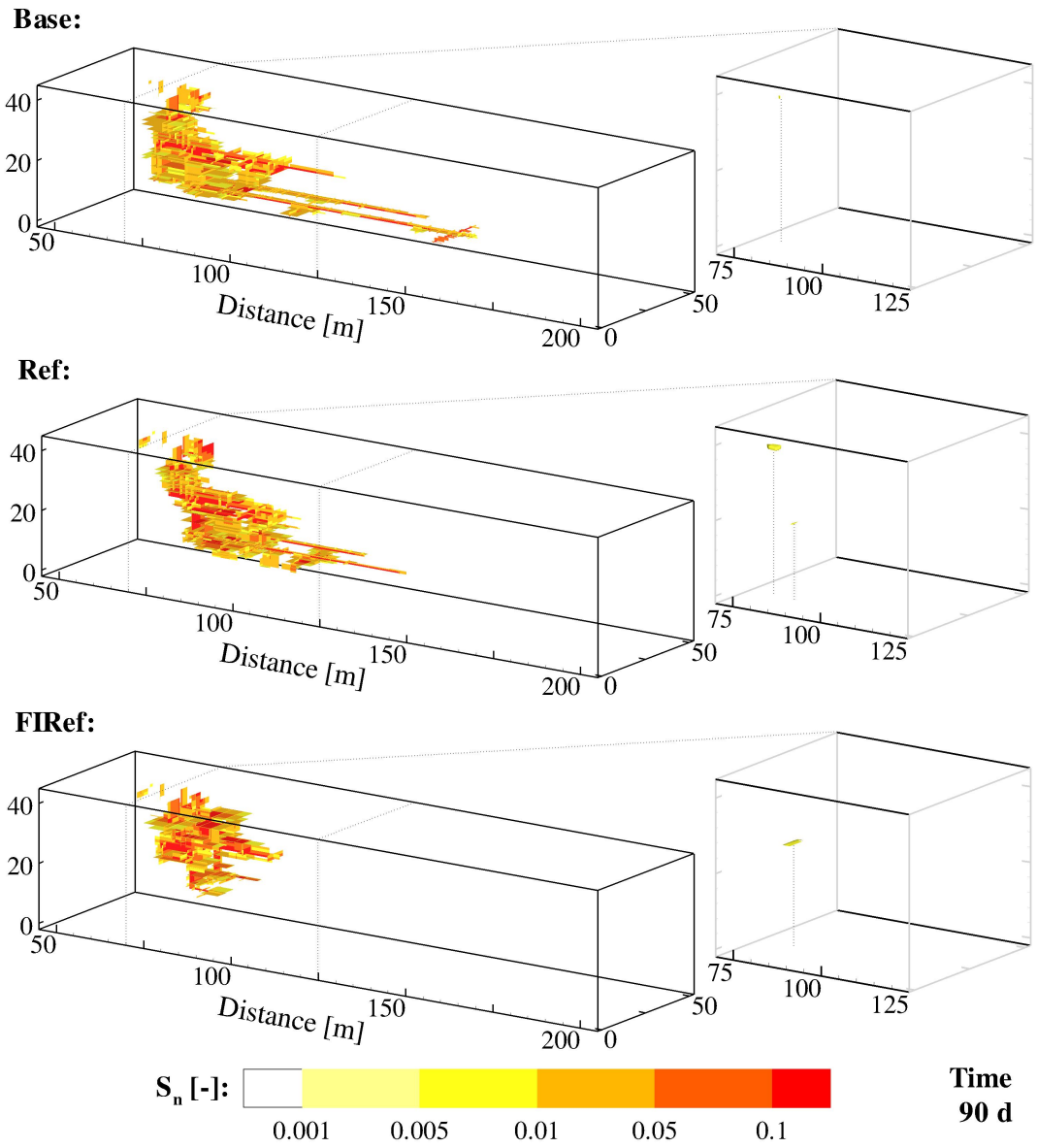

Figure 2-8 NAPL Saturation (S_n) in the fracture network (left) and matrix (right) after 90 days of TCE injection with the three different unstructured meshes.

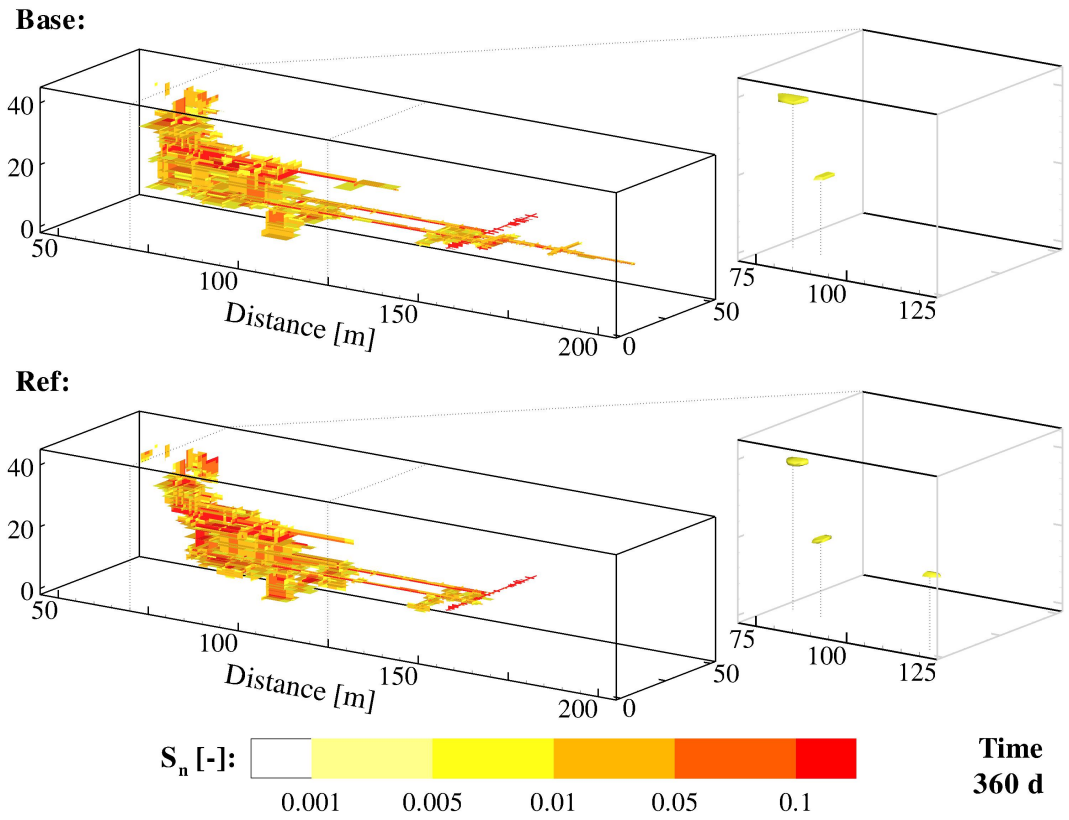

Figure 2-9 NAPL saturation (S_n) in the fractures (left) and matrix (right) after one year in the Base and Ref scenarios. NAPL is predominantly in the fracture network, except for two and three isolated pockets, which are visible only when saturation in the fractures is omitted.

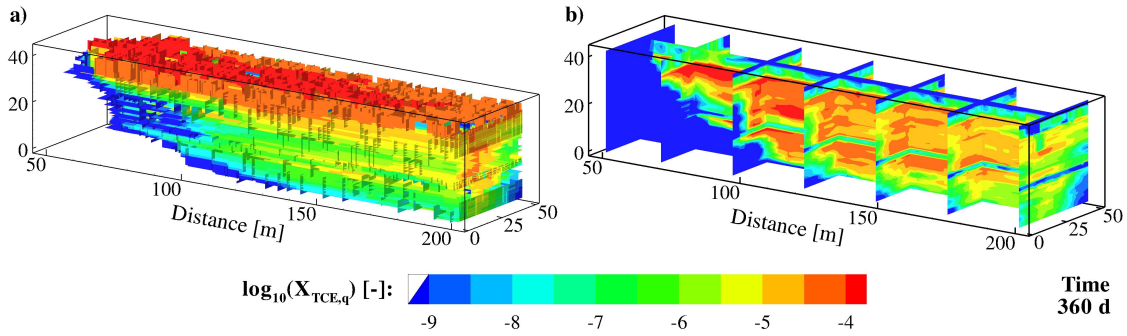

Figure 2-10 Mole fraction of TCE in the aqueous phase ($X_{TCE,q}$) after one year in the Base scenario a) in the fracture network and b) in trans-section and long-sections exposing the porous medium.

2.3.4 Fluxes at the Control Plane

Examination of the fluxes at a control plane yields a more quantitative basis for comparison of how the different unstructured meshes compare to one another and how asperity contact may influence bulk flow. In this section we consider volumetric fluxes of water and mass fluxes of TCE crossing a control plane at x = 140 m, which is approximately 80 m downgradient from the NAPL loading location (see Figure 2-7). Average

fluxes are calculated by summing the molar fluxes at each CV pair interface incident with the control plane, then by dividing by the (50×43) m^2 area of the boundary. Either all pairs or exclusively fracture CV pairs are included in these sums to produce the total or fracture-only fluxes. In the following discussion we provide relative error values to quantify difference in fluxes between simulation runs. These are calculated with respect to the maximum value in a given set. Using Figure 2-12 we make observations about: how the mesh and asperity contact affect water flow and bulk hydraulic conductivity (bulk-K); the proportioning of water flux between the matrix and fractures; flow interference between the aqueous and nonaqueous phases; how the mesh and asperity contact affect TCE mass flux and first arrival at the control plane; and finally, proportioning of TCE flux between the fractures and matrix.

We assume that water flux at this control plane is representative of flux everywhere. Thus, because the hydraulic gradient applied by the simulation BCs is the same in all cases, then differences appearing in Figure 2-12a reveal that water flux depends on both the mesh and on α. We always expect some mesh influence due to the numerical inaccuracy inherent in spatial discretization, and we hypothesized α-dependence because it directly affects CV-to-CV flow area. The relative error in water flux is 20% between FIRef, α =0.0 and Ref, α =0.0 when different meshes are considered, whereas the maximum relative error is only 0.5%, as calculated from the FIRef set. Thus, we find that the mesh has a greater influence than asperity contact on bulk-K for water flow.

Figure 2-12b shows approximately 92% of water flux is steadily conducted through the fracture network and thus the remaining 8% is conducted through the PM. The relative error is 0.8% between the maximum (FIRef,α=0) and minimum (Ref,α=0.2) normalized flux, which indicates only a small mesh-dependence of the fracture-PM flow proportions. We suspect that the fracture network characteristics control this ratio but we did not test this specifically. Partitioning of flow has important implications when we consider contaminant transport. We will revisit and elaborate on this thought below.

Regarding interference between the two flowing phases, in Figure 2-12a we see very little impact to water flux at the fence from the increasing presence of NAPL. Conceptually, the presence of a NAPL causes a decrease in the relative permeability of the aqueous phase within the source zone. S_n is about 0.15 in the fractures, which yields a reduction of 0.35 in k_{rq} from fully water saturated conditions (see Slough et al. [3], Figure 1a). The

aqueous phase presumably has the opportunity to circumvent the source zone because the 3D fracture network is well connected, or may increase the proportion of flow in the NAPL-free matrix. This local influence to flow may be reflected in a control plane located nearer to the source zone, but is not well reflected in the fluxes obtained at x = 140 m. Conversely, the aqueous phase has a profound influence on the nonaqueous phase. k_{rn} is only marginally above zero at S_q of 0.85. The ambient fluid pressure field, combined with the fracture network anisotropy, causes the invading fluid to migrate in the same direction as water. These factors, plus the gravitational influence on the DNAPL, gives the source zone its elongated shape, and downgradient and slightly downward plunging orientation as seen in Figure 2-8 and Figure 2-9.

Turning our attention to the TCE mass flux in Figure 2-12c, we see some difference between simulations during NAPL loading and very little difference after loading. First arrival occurs at approximately one day after injection in all cases. The relative error term for flux is initially high, near 45% at 10 d, near 20% at 100 d, and is 3.5% at the end of NAPL loading. The initial disparity in the flux may be linked to differences early time DNAPL source zone architecture as influenced by the mesh, but we cannot draw any clear relationship. Increasing asperity contact appears to increase the TCE mass flux for each mesh. The cause for this trend is similarly convoluted but we suggest two contributing factors: the decreased fracture-matrix communication causes more NAPL to remain in the fracture network, and thus it elongates the source, which approaches the control plane sooner; or, increased matrix-to-matrix communication may enhance numerical dispersion, thus transporting plume downgradient faster.

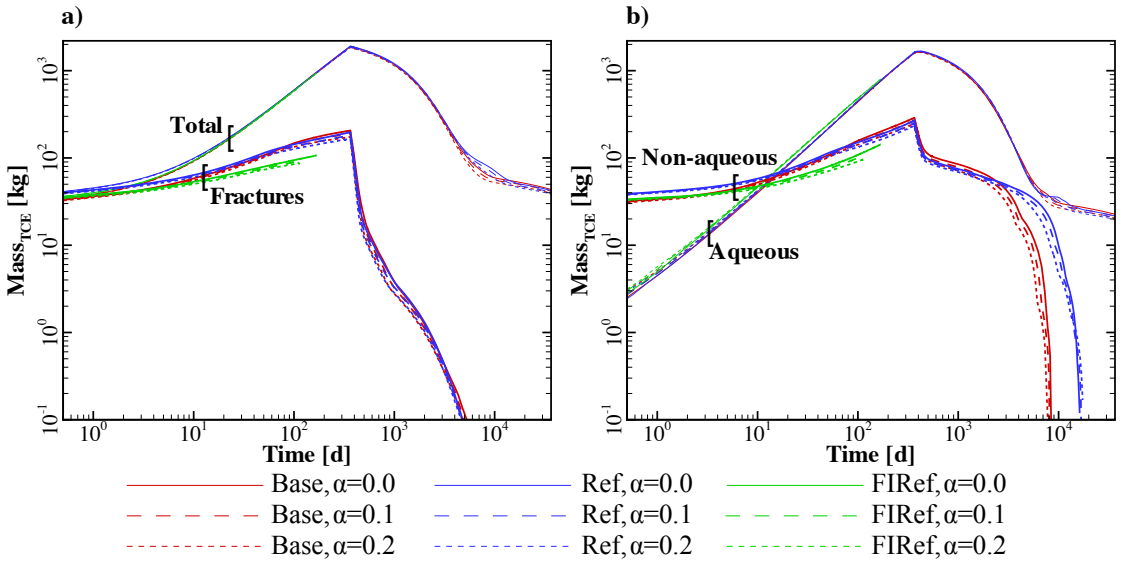

Figure 2-11 Comparison of TCE mass distribution versus time in the Base, Ref and FIRef simulations with α =0.0, 0.1, and 0.2: a) total TCE mass and mass in the fracture network only; and b) mass of TCE in the nonaqueous and aqueous phases. FIRef simulations are in progress; results up to the most recently computed time step are shown.

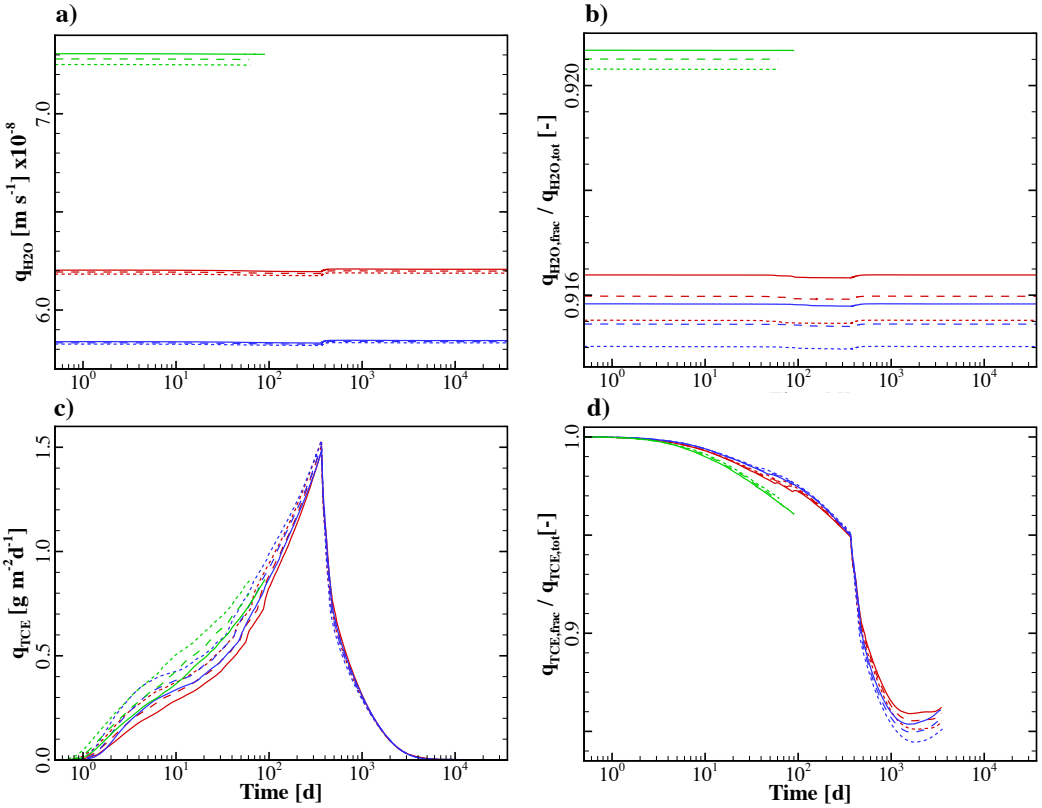

Figure 2-12 Comparison of spatially averaged fluxes of water (q_{H2O}) and TCE mass (q_{TCE}) crossing the control plane at x=140 m versus time in nine simulation runs: a) Total flux of water; b) water flux in the fracture network, normalized by total flux; c) total TCE mass flux; d) TCE flux in the fracture network, normalized by total TCE flux (truncated at 3650 d). FIRef simulations are in progress; results up to the most recently computed time step are shown. See legend in Figure 2-11.

Normalized fracture fluxes depicted in Figure 2-12d show the splitting of TCE mass flux at the control plane between the fracture network and PM. The data sets in this figure have been judiciously truncated at 10 years because the low flux rates combined with convergence tolerances in the numerical solver yield erratic, nonphysical ratio values. Therefore, we do not consider later times in this discussion. The normalized fluxes from the Base and Ref cases are similar, but the FIRef flux is less than the previous two. Generally, we see 85% to 100% TCE mass being transmitted in the fracture network and 0 to 15% passing in the PM. These ranges include a 95-to-5% split when the maximum mass flux occurs at 365 d, the end of NAPL loading. The shape of these curves is consistent with physical phenomena. Initially the flux is fracture-dominant because fast moving fracture water dissolves NAPL and carries it across the control plane. The fracture flux wanes as NAPL dissolves and is carried or diffuses into the matrix where it is transported more slowly by matrix flow. The fracture flux kinks and decreases at the end of NAPL loading when the additional fluid pressure incurred by the source term ceases. Finally, there is an upswing in the flux at ~2000 d (which corresponds to the inflection in the TCE mass in fractures in Figure 2-11a that may signify that back diffusion is becoming dominant in transport.

The results of Figure 2-12b and d indicate that matrix flow plays an appreciable role in the bulk flow system and transport of dissolved TCE. Recall the assumption of no flow in the PM engrained in the conceptual model of DP simulators (e.g. Warren and Root [8] and Kazemi [9] and Reiss [10]) or the classic analytical models of solute transport in fractures (e.g. Tang et al. [45]). These results reinforce the need for modeling practitioners to be aware of model assumptions and whether those assumptions apply in a given geologic context. In the case of the Smithville site model, which includes fractured and permeable dolostone stratigraphy, these results suggest that some amount of contaminant transport will occur in the matrix well into the future.

2.4 Conclusions

The purpose of this chapter is to introduce the framework for a practical way of modeling three-phase flow in fractured porous media. Our formulation couples the DFN and PM using physically based relationships parameterized by measurable physical quantities. The entire set of governing and discretized equations for three-phase flow, multicomponent transport, and BC implementation are laid out herein. Our approach

allows for construction of an unstructured mesh to help incorporate fractures at the density of interest while keeping the number of CVs in the numerical system relatively small. Then, simplifying assumptions are made so that small volume nodes at the intersections of fractures can be algebraically eliminated, thus removing undue constraints on the time step size. Asperity contact bridging is incorporated in this model; it permits fracture cross flow to occur but in doing so diminishes the area available for fracture-matrix interaction.

Based on the water-NAPL simulations of the Smithville site, we draw the following conclusions:

- The unstructured mesh scheme makes it possible to simulate relatively dense DFNs at a spatial scale relevant to NAPL source zone evolution problems;
- Numerical error due to the spatial discretization (i.e. unstructured mesh realization) affects bulk-*K*. Water flux at the control plane, in particular, showed mesh-dependence;
- Increasing the asperity contact ratio has the marginal effect of decreasing bulk-*K* of water (which preferentially resides in the matrix) and increasing the bulk-*K* of TCE NAPL (preferentially resides in fractures);
- Mesh-dependence of bulk-*K* has a greater effect than asperity contact ratio on flow rates; and
- Our coupled DFN-PM formulation splits aqueous phase flux by 8% to 92% and TCE mass flux by a maximum of 15% to 85% between the PM and fracture network, respectively. These observations suggest the importance of considering combined fracture and matrix flow in contaminant transport and diffusion problems.

In conclusion, simulation results of the type presented herein are rare in the contaminant hydrology literature. We feel that the numerical error incurred by the unstructured mesh is permissible at this stage, given that we face the dilemma of simulations with imperfect results versus intractable simulations. We believe it is worthwhile to continue in

three aspects of this line of research: first, to refine simulation parameters by continuing to collect experimental evidence; second, to pursue code enhancements that harness parallel computing. Parallel computing will permit grid refinement, which will in turn reduce the numerical error incurred; and finally, to pursue code enhancements to couple this code with another numerical model that is capable of simulating dissolved plume transport at spatial scales relevant to problems of groundwater resource protection.

Chapter 3

Consequences of Fracture Intersections and Asperity Contact to Modeling Three-phase Flow in Discretely Fractured Rock

Chapter Summary

To support modeling of nonaqueous phase liquid (NAPL) source zones as they evolve in the vadose and saturated zones of discretely fractured rock, we present various simulations pertaining to flow at fracture intersections, flow perpendicular to fracture planes, and mesh refinement near fracture planes using the numerical model *CompFlow Bio*. This numerical model simulates isothermal flow and transport of three components (water, air and trichloroethylene(TCE)) in three mobile and mutually interactive phases (aqueous, gas, NAPL) in a three-dimensional, single-continuum porous medium and discrete fracture network domain. Two small scale numerical investigations designed to isolate these flow effects are conducted: first, we present simulations of laboratory experiments involving flow of an invading fluid phase at a simple fracture intersection using water-air and TCE-water systems; second, we carry out a grid refinement exercise to a) examine capillary barrier effects and flow through asperity contact points as water encounters gas-filled fractures, and b) examine TCE imbibition and flow direction at fracture intersections in settings above the capillary fringe, within the capillary fringe, and below the water table. Results of the first scenario provide evidence supporting the elimination of control volumes at fracture intersections in some circumstances. The latter exercises demonstrate complex three-phase fluid interactions when a porous medium and discrete fractures are considered and reveals some bias and mesh effects that must be considered in larger scale model applications.

3.1 Introduction

In the field of contaminant hydrogeology, trichloroethylene (TCE) is one of many substances in a group called nonaqueous phase liquids (NAPLs) that contaminate the subsurface at many industrial sites worldwide. Because exposure to trace quantities of TCE in water or air is a concern to human health [46], and because TCE is only slightly soluble in water, TCE NAPL source zones potentially have long term impacts to the quality of groundwater at down-gradient receptors.

The Santa Susana Field Laboratory (SSFL), located near Los Angeles, California, is one example site of TCE contamination. The SSFL sits on top of fractured Chatsworth Formation bedrock, which is a turbidite sequence of sandstones with siltstone and shale interbeds [47]. The conceptual model of the contamination pathway is that TCE, as a NAPL, was released at the ground surface and has migrated downwards through fractures and the rock matrix in the vadose zone and through fractures in the saturated zone. TCE has entered the rock matrix material by dissolution and diffusion, imbibition, and conceivably by overcoming the rock's pore entry pressure, as may occur near dead-end fractures. Today, decades after the initial release, the contaminant resides primarily in the rock matrix where plume migration is strongly attenuated by natural processes [48, 49, 50]. One aspect of current effort is to use a numerical model to explore the architecture of the NAPL source zone above and below the water table. Model results will be used as evidence to support or challenge the existing conceptual models of contamination and to influence future laboratory or fieldwork as it pertains to further site investigation and source zone remediation.

Mathematical and numerical models for flow through fractured porous media can be divided broadly into the categories of deterministic or stochastic. In deterministic models, three main types are described by Narasimhan [7]: equivalent porous media (EPM); dual continuum (which may be further divided into dual-permeability (DK) [11] where fluid is mobile in the porous medium and fracture continua, or dual-porosity (DP) [8, 9, 10] where pore fluid is immobile); and discrete fracture network (DFN) approach [12, 13]. Stochastic models are well described by Neuman [51]Neuman [51]Neuman [51]Neuman [51]. In that same review of modeling trends in fractured rock Neuman [51]Neuman [51]Neuman [51]Neuman [51] points out that DFN approach models generally require more input data than the other model types. This stems from pedagogical assumption that small scale flow

and transport phenomena influence one another and define the larger scale system. Parker et al. [52] advocate field based measurement techniques that may be used to inform DFN model parameters. In this study we use a model of the DFN variety with which we examine the small scale phenomena described below and the effects of our choices in the model's spatial discretization.

Our numerical modeling work herein involves flow of three mobile and mutually interactive phases (i.e. the aqueous, nonaqueous and gas phases) in discretely fractured porous media (PM). Four key hypotheses related to multiphase flow underpin the study: first, we take for granted that surficial and interfacial tensions between fluids can be captured with macro-scale constitutive relationships; second, that these relationships determine fluid occupancy (and thus fluid flow) at fracture intersections; third, that they may give rise to barriers to aqueous and nonaqueous phase flow within the matrix perpendicular to gas-filled fractures; finally, that the constitutive relationships play a role in controlling rates of aqueous and nonaqueous phase liquid imbibition into the matrix as these liquids migrate through permeable fractures. We now briefly describe these hypotheses and how we test the numerical model against them.

Interfacial tension between immiscible fluid pairs and surface tension at fluid-solid interfaces give rise to capillary pressure and dictate wettability. We consider here the common case where the aqueous phase is most wetting (i.e. it preferentially resides in pore space or fracture voids where smaller aperture pore throats or fracture void spaces are occupied most strongly), the gas phase is least wetting, and the nonaqueous phase is intermediate to the previous two. In turn, pore/void occupancy influences the connectedness and ability of a fluid to flow, which, in the continuum approach, are reflected in the relationships of phase saturation to capillary pressure and relative permeability. Collectively these are referred to as the relative permeability-saturation-capillary pressure (k_r-S-P_c) relationships. Our main goal is not to define or validate k_r-S-P_c relationships but merely to assess their consequences. For example, returning to the context of flow in discretely fractured rock and the task at hand, the phase that occupies a fracture void space may be highly influential to local flow patterns: a fracture in the vadose zone will be preferentially gas-filled due to its relatively large aperture. It may act as a capillary barrier to water approaching in the adjacent rock matrix due to this "preference."

Fracture cross flow has been the topic of several studies (e.g. see below) because it is recognized as influential in multiphase flow. (We note that 'fracture cross flow' has been used elsewhere, particularly in the DK modeling literature, to denote fluid transfer between fracture and matrix continua. Herein, we use it for direct matrix-to-matrix flow across a fracture plane.) This type of flow is depicted conceptually in Figure 3-1 (after Figure 7.2.1 in Wang and Narasimhan [53]). Because capillary barriers, depicted in Figure 3-1a, are influential to wetting-phase flow in the vadose zone [54], fracture cross flow becomes an important mechanism to circumvent such barriers. Some theoretical and laboratory work has been done to gain insight into fracture cross flow: Makurat [55] measured single-phase fracture cross flow under different fracture stress-strain conditions. Considering two phases, Firoozabadi and Hauge [56] addressed capillary effects and liquid drainage across air-filled fractures. Subsequently, Firoozabadi and Markeset [57] showed that flowing petroleum exhibits these liquid bridging effects in laboratory experiments using milled sandstone blocks in various configurations across 1000 μm, smooth-walled fractures. Dejam and Hassanzadeh [58] have recently put forth some theoretical work for *liquid bridging* or *capillary cross flow* depicted in Figure 3-1b, an idea put forth by Saidi [59]. We hypothesize that a second mechanism for fracture cross flow is flow through matrix material in areas where opposing walls of a fracture make direct contact, as in Figure 3-1c. Herein, this shall be termed *asperity contact bridging.* Some researchers have numerically modeled dynamic closure of rough-walled fractures based on hydromechanical stress and strain (e.g. Unger and Mase [60], McDermott and Kolditz [61], and Walsh et al. [62]). Those studies and their supporting works describe measurable properties of the rock and the hydromechanical system that form a basis for quantitatively estimating the amount of fracture surface area where opposite walls are in direct contact. It is through this surface area where we postulate that Darcy flow occurs. Under this supposition we explicitly allow for this flow mechanism in our numerical model.

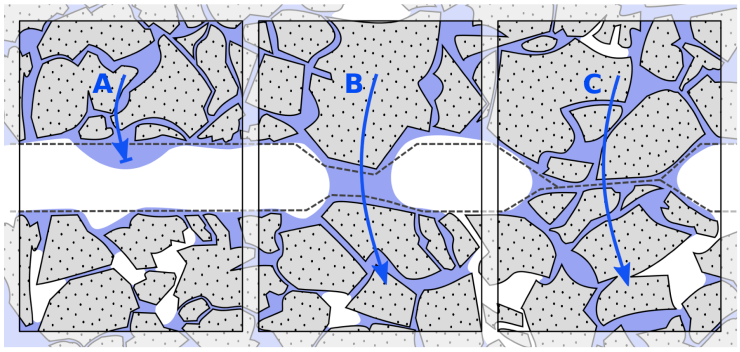

Figure 3-1 Schematic representation of two phases, wetting and non-wetting, e.g. aqueous and gas, in a fractured porous medium with wetting phase a) at a capillary barrier, or exhibiting fracture cross flow via b) a liquid bridge or c) an asperity contact bridge.

When fractures are idealized as parallel plates, the intersection of two fractures has a large void space relative to the incident branches. As such, fracture intersections are influential to multiphase fluid flow in two ways: an invading fluid may encounter the intersection in a parallel direction (i.e. flowing along the intersection); or from a perpendicular direction (i.e. originating from a fracture branch). The former may be a conduit for flow [63] because of the enlarged void space. The latter, which is of consequence in this study, may cause a barrier to the flow of the invading phase and may then influence the direction of outflow. Capillary barriers and outflow direction are the subjects of several studies (e.g. Glass et al. [64], Dragila and Weisbrod [65], Ji et al. [66], and Ji et al. [67]). Section 3.2.1 further describes how we use knowledge of two-phase flow behaviour at a simple fracture intersection to judge the consequence of the modeling choice to retain or eliminate the numerical entity representing the intersection.

Imbibition, fluid flow driven by capillarity-based tension forces, is the final physical process that we highlight. Although we do not attempt to quantify imbibition rates specifically, the constitutive relationships described above give rise to this phenomenon in our model. Thus, in the three-phase context, it is relevant to observe this flow (e.g. a wetting fluid from fracture to matrix or within the matrix transverse to the primary fluid flow direction) because it influences the overall phase distribution, internal structure, and rate of forward movement.

In this study we report on the ability of the three-phase, compositional model *CompFlow Bio* to capture the phenomena mentioned above using small scale test scenarios. Our objectives are threefold: first, to validate the practice of algebraically eliminating small volume fracture intersection finite-volumes; second, to expose any limitations or

sensitivity in the model with respect to the spatial discretization and parameterization; third, to elucidate the effect of fracture cross flow (i.e. capillary barriers combined with flow through asperity contact points). To achieve these goals we model: 1) the direction of both non-wetting and wetting phase fluid invasion at fracture intersections as governed by the capillary forces in outflow fractures of different apertures and compare model results to results of a laboratory experiment; 2a) in the context of a grid-refinement exercise, fracture-matrix flow interactions as wetting phases imbibe or as non-wetting phases displace the resident wetting phase from a fracture; and finally, 2b) cross-fracture matrix-to-matrix flow as it is influenced by capillarity and relative permeability barriers that exist in variably saturated systems. The ultimate consequence of this study is to provide model insight and justification for larger scale simulations.

In Section 3.2 we briefly describe our numerical model. We explain the conceptual set up and results of our two small scale test problems, those being scenarios for flow at fracture intersections in Section 3.2.1 and flow through asperity contact points in Section 3.2.2. In Section 3.3 we summarize the major results and implications, and provide some concluding remarks on the performance of the model. Finally, to report more fully on our methods, Appendix A contains relevant simulation parameters and a discussion of creating three-phase k_r-S-P_c relationships.

3.2 Numerical Simulations

To conduct these simulations we use an augmented version of *CompFlow Bio* (see e.g. Unger et al. [1]). This model is a three-phase, multicomponent flow and transport simulator that uses equilibrium phase partitioning of component species. It uses a first-order accurate finite-volume discretization scheme for rectilinear porous media CVs and rectangular fracture CVs. We follow the approach of Slough et al. [2] for flow at fracture intersections, which we extend to eliminate "point fractures" that occur at the intersection of three orthogonal fracture planes. Fracture cross flow is facilitated by including extra adjacency relationships in the discretized domain: in places where two PM finite-volumes are separated by a fracture we assume Darcy flow over an interface with area $\alpha \times A$, where A [m^2] is total the common surface area of the fracture and two PM volumes and α [-] is the ratio of asperity contact area per unit total area. The details of fracture intersection elimination and asperity contact bridged flow enhancements may be found in Chapter 2.

3.2.1 Flux at Fracture Intersections

To judge the effect of algebraic elimination of fracture intersection CVs and the assumptions in equation (21) of Chapter 2, the laboratory experiments conducted by Ji et al. [67] are used as the framework for a suite of test simulations. Their experiment was chosen as the conceptual basis for this suite: 1) because of its geometric simplicity and its apparent relevance to our investigation into the impact of using node elimination; and 2) because TCE invading water and water invading gas-filled fractures are small scale analogues to NAPL invading the saturated zone and NAPL or aqueous phase invading gas-filled fractures in the vadose zone. These items are all of field-relevance for the SSFL investigation. For reasons explained below, we only attempt to glean a qualitative comparison between the laboratory and the simulation results. A description of the parameterization is given in Appendix A.

In the laboratory experiment the investigators fabricated a simple fracture intersection by cracking a glass plate to form a vertical and a horizontal fracture. Wires of different diameters were used to hold fractures open at the desired apertures. The investigators then examined non-wetting phase flow behaviour by injecting TCE into initially water-filled fractures, and wetting phase flow by injecting water into initially gas-filled fractures. Under three different cases of horizontal fracture aperture they injected the invading fluid into the top of the vertical fracture and allowed gravity-driven displacement to occur. They observed very complex phase structures depending on the injection rate (i.e. modifying the relative importance of viscous versus capillary forces) and quantified their results by comparing predicted versus observed pool heights above the fracture intersection. (For full details, see Ji et al. [67].)

A continuum model cannot capture many of the complex phase structures observed in the experiment such as blobs, tendrils, and columns of fluid hanging below the target intersection. As dictated by the continuum model framework, our simulations use k_r-S-P_c relationships characteristic of rough-walled fractures at a macro scale. Our application of these k_r-S-P_c relationships to smooth, parallel plate-like glass fracture to mimic the pore-network-like behaviour of the phases in the vicinity of the fracture intersection is irresolute. Therefore, our purpose for using these experiments is to judge whether the numerical model can correctly capture the correct direction of flow at the fracture intersection rather than to make a quantitative match to measured pool heights.

Conceptually, we will scrutinize the flow path at a four-way intersection where fluid enters from the top branch and may flow horizontally left or right, or continue downwards. From this set up we shall compare results from retaining and eliminating the central node. Because the intersection node has a slightly larger aperture and hence a slightly different capillary pressure than the inflow and outflow fractures, hypotheses are: 1a) NAPL will readily invade the intersection and the outflow nodes will act as capillary barriers as shown schematically in Ji et al. [67] Figure 7; 1b) the intersection itself will act as a capillary barrier to invading water, see Ji et al. [67] Figure 5a; 2) these capillary barrier effects will be less prominent when the intersection CV is eliminated; 3) in all cases, outflow path will be dictated by lowest (non-wetting phase invasion) or highest (wetting phase invasion) capillary pressure; and finally, 4) capillary pressure of peripheral and boundary fractures will constrain the flow to paths that replicate the experiment.

3.2.1.1 Numerical Representation of the Fractured Glass Plate Experiments

The physical experimental set up is matched well by the simulation domain with respect to size, fracture location and fracture aperture. The target vertical and horizontal fracture, as well as side bounding fractures and the front and back bounding plates are modeled exactly. One slight but possibly important deviation from the experiment is in the alignment of the horizontal fracture at the intersection. The simulated horizontal fracture is aligned perfectly whereas the actual fracture was slightly offset due to inherent difficulties in creating the mechanical break. The fractures are outlined in Figure 3-2 using black lines and form a domain that is 25 cm long, 25 cm tall and 1.9 cm thick. The vertical fracture has an aperture of 371 μm while the horizontal fracture has aperture 371 μm, 650 μm or 295 μm. These three combinations shall be referred to as cases '371-371,' '371-650' and '371-295,' respectively. The aperture at the fracture intersection is determined by calculating the hypotenuse of the apertures of the two intersecting fractures giving 525, 748 and 474 μm respectively for each of the three cases. (We choose the hypotenuse as aperture based on the idealized phase structure at the fracture intersection presented in Figure 5c in [67]. It will also always yield an aperture value larger than those of the incident branches, which is desirable for our capillary pressure calculations.) For non-wetting phase flow, the peripheral fractures have apertures 80 μm for the front and back bounding plates, 295 μm for the top, left and right perimeter fractures and 650 μm for the bottom perimeter fracture. The bottom fracture has the largest aperture and thus the least capillary pressure difference to promote free exit of the non-wetting phase. For wetting

phase flow the bounding fractures have apertures of 1000 µm, 650 µm, and 100 µm, respectively. Matrix CVs in the spaces between the fractures are removed from the simulation to mimic impermeable glass by precluding fracture-matrix interaction. Fracture CVs adjacent to the intersection are very well resolved spatially; sizes are approximately 1, 5, 10, and 20 mm, respectively, leading outward from the intersection.

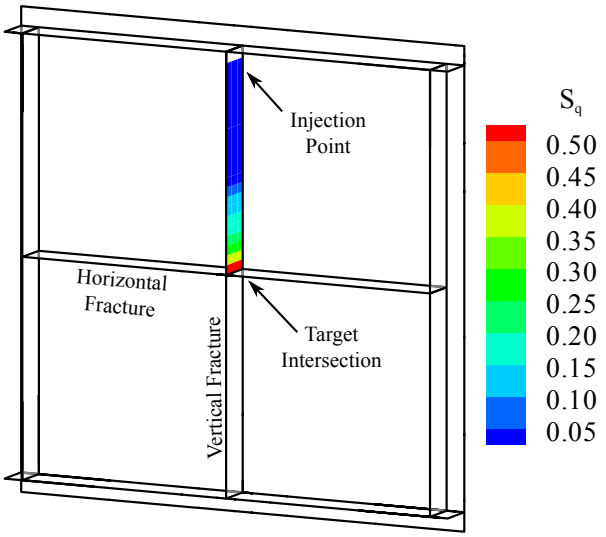

Figure 3-2 25 cm × 1.9 cm × 25 cm domain for glass plate simulations with the front plate hidden. Contours show aqueous phase saturation of before breaking through the intersection in the water-air simulation, case 371-650.

Boundary conditions are imposed around the perimeter of the bounding plates and at the left and right ends of the upper and lower perimeter fractures to allow free entry or exit of the resident phase and free exit of the invading phase. To create these boundary conditions, each simulation run undergoes two distinct stages. First, the simulation is run to a suitable pseudo-steady-state with a single node holding a static water pressure source/sink term (maintaining the water table above the top of the domain for initially water-filled conditions and near the bottom for initially gas-filled conditions). Second, the source/sink term is removed and all nodes on the perimeter of the front and back plates and the ends of the top and bottom bounding fractures become essentially invariant in composition and pressure by using a large volume multiplier, $B = 10^6$, similar to the approach in the *TOUGH2* numerical simulator [68].

Injection of the invading fluid occurs at a steady rate of 0.012 mL/min in all simulation cases. Ji et al. [67] used a six-tier stepped injection rate varying from 0.012 mL/min to 10.00 mL/min. We chose only the smallest injection rate for the simulations to

keep the flow regime governed by capillary forces. Capillary numbers for the chosen injection rate at the point of injection is $Ca = \mu_n v_n / \sigma_{nq} \cong 7.4\times10^{-10}$ or $\mu_q v_q / \sigma_{gq} \cong 5.1\times10^{-10}$ for TCE into water or water into air, respectively, where v is the superficial velocity assuming saturated downward flow from the CV holding the source term to the next lower CV in the fracture.

Relative permeability versus saturation relationships and capillary pressure versus saturation relationships are explained in the Appendix. Other phase and fluid properties are listed in Table A-1 through Table A-3.

For the purpose of reporting the simulation results, monitoring of advective flux occurs at *fences* located 5 mm away from the fracture intersection in each direction. In the following sections, the fence above the target intersection that captures downward flow is termed 'inflow', the fence below the intersection is termed 'outflow, downward,' and the two fences capturing lateral flow are summed together and termed 'outflow, sideways.' Flow into or through the bounding plate fractures is negligible or non-existent so we omit them from the following results. Flow rate values in the preceding list are divided by the injection rate to produce normalized values.

3.2.1.2 TCE-Water Simulation Results

Figure 3-3 shows the results of non-wetting phase invasion of TCE into water depicted as the volumetric rate of TCE NAPL (normalized by the injection rate) flowing in and out of the target intersection through time. In this situation we expect NAPL to readily enter the fracture intersection due to its inherent lower capillary pressure relative to the upstream fracture. Next, we expect the NAPL to pool above the intersection until sufficient backpressure is built up to breach any outflow capillary barrier. These expectations follow directly from observations reported by Ji et al. [67]. In all cases, node elimination has no impact on the flow rate of TCE above the target intersection from above based on the agreement of flow rates in Figure 3-3. Inflection points in the curves in this figure indicate times of partial backfilling above the monitoring fence. This occurs before the NAPL breaches the capillary barriers of any outflow fracture. Case 371-371 in Figure 3-3a exhibits the most sensitivity to the node elimination strategy. With the intersection node, the NAPL follows a direct downward flow path, which contrasts with a 90% downward and 10% sideways split when the node is removed. Ji et al. [67] observed slight sideways penetration, then the formation of a hanging column from which blobs and tendrils of downward flow

formed. The 371-650 case shown in Figure 3-3b yields exclusively sideways flow that is consistent with the laboratory observations. There is a slight time lag in the no-elimination case due to a lower potential difference between the 747 μm intersection CV and the 650 μm outflow CV as compared to the elimination case where the 371 μm inflow fracture CV is connected directly to the 650 μm outflow CV. The small wane in the sideways outflow rate (the shallow trough centred at 0.015d) is attributed to TCE storage in the nodes adjacent to the intersection. This back filling ceases and 100% sideways flow is resumed by 0.02 d. Finally, Figure 3-3c shows the results of case 371-295 where, consistent with laboratory observations, downward flow occurs exclusively.

3.2.1.3 Water-Air Simulation Results

Figure 3-4 shows the results of the wetting-phase invasion simulations: water into initially air-filled fractures. Consistent with the results of laboratory experiments, e.g. Ji et al. [67] and Glass et al. [69], we expect the intersection itself to be a barrier to wetting phase flow in all cases because of the relative increase in gas-filled void space. Thus, some column of water should always form above the intersection. This suite exposes a greater impact to flux caused by retaining or eliminating the intersection node when compared to the preceding TCE-water suite. The greatest difference is in the intersection inflow rate. Retaining the intersection node indeed causes a barrier to aqueous phase entry. Figure 3-2 depicts water held above the intersection. The backup is caused by capillary pressure holding the wetting phase in tension in the upper fracture. The phase must form a sufficient head to overcome that "capillary barrier." In contrast, no such barrier is seen in the case of node elimination. Figure 3-2 also shows a rarefaction in the aqueous phase saturation extending from the leading edge at the intersection back to the injection point. This phenomenon was not observed in the experiment and is likely a consequence of using continuum-based k_r-S-P_c relationships.

Cases 371-371 and 371-650 show plateaus in the inflow rate when water is backing up above the intersection. The time before intersection breakthrough is proportional to the strength of the capillary barrier. In simulations where the intersection node is eliminated. the plateau is not present and the invading phase diverts to an outflow channel immediately. 371-371 shows disagreement in the initial outflow directions. However, at later time (after about 0.06 d, not shown), the solution with the intersection CV present tends towards a 99% downward dominant flow path in accord with the corresponding

case employing elimination. Ji et al. [67] observed filling of the left and right branches in 371-371, and filling of the left branch only in 371-650 before regular downward flow commenced. In case 371-295 the dominant initial flow path is sideways but the degree of flow splitting differs between 60-40% when the node is retained and 80-20% when the node is eliminated. In the laboratory, the left branch filled first due to misalignment of the horizontal fracture, then flow split between the right and downward flow directions with flow into the right branch being slightly more dominant.

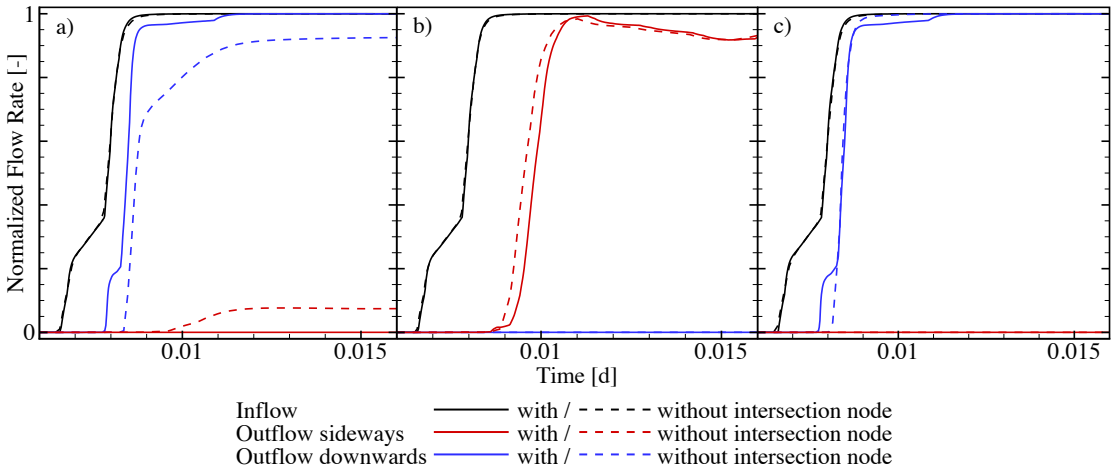

Figure 3-3 Results of the TCE-water simulation showing NAPL flow rates at the target intersection in cases a) 371-371, b) 371-650 and c) 371-295.

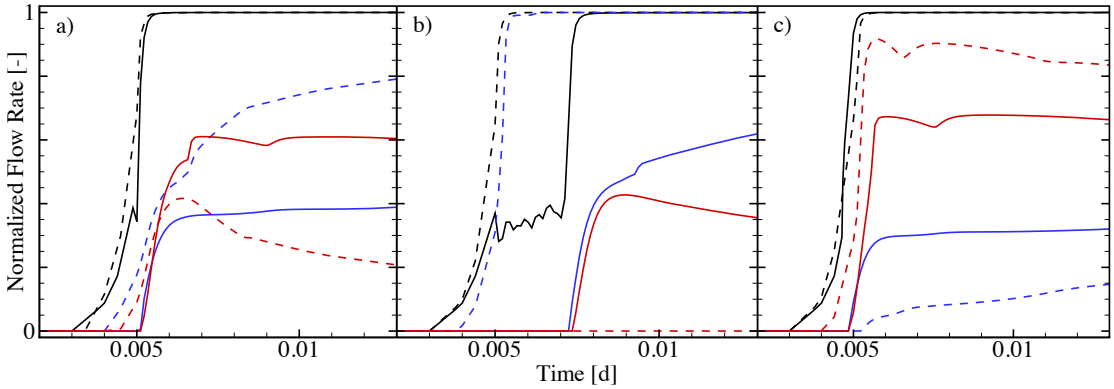

Figure 3-4 Results of the water-air simulation showing water flow rates at the target intersection in a) case 371-371, b) case 371-650, and case 371-295. See legend in Figure 3-3.

3.2.1.4 Fractured Glass Plate Experiment Summary

Based on the TCE-water simulations, node elimination has little impact on non-wetting phase/NAPL flow direction in initially aqueous phase-filled fractures at simple fracture intersections. Furthermore, the simulation results are a qualitative match to those of the laboratory experiment. Predicated on the hypothesis that large, multi-fracture

systems behave as the sum of many small systems like this one, we can therefore claim that these results demonstrate that node elimination could be applied in the saturated zone of larger scale SSFL simulations without detriment to the architecture of the evolving NAPL source zone.

Based on the water-air simulations, retaining versus eliminating the CV at the fracture intersection causes significant differences in invading phase breakthrough time and dominance of one flow direction over the other. Eliminating the node: 1) removes the barrier to downward wetting-phase flow above the intersection (i.e. causes a temporal change); and 2) changes the ratios of flow path diversion to being predominantly downward. The net effect of node elimination is to cause more immediate, downward-biased flow as wetting fluid invades the intersection.

The caveat of both of the above situations is that the porous medium has been removed. In three-phase flow situations with a porous medium the capillary pressure and permeability contrast between the fracture and the rock matrix may influence flow timing and direction. We address the consequence of fracture flow interacting with a porous medium in the following sections, which are much more readily applicable to modeling the SSFL site characteristics.

3.2.2 Fracture-Matrix Interaction

In any field-relevant DFN modeling application, the fracture network cannot be considered in isolation of the rock matrix due to loss of important physical processes like diffusion[6], imbibition, and matrix flow itself. As the complexity of the physical system increases, more fluxes and nonlinear processes are included in the formulation and the tradeoff between accuracy and computational tractability is encountered. A common way to keep a problem tractable in hydrogeological modeling is to increase the size of CVs, which thereby decreases the number of unknowns in the numerical system of equations. Increasing the size of a CV increases the amount of spatial error (and temporal error by way of relaxed Courant constraints on the time step) in finite-volume discretizations. Thus, it is necessary to distill the artifacts caused by inherent spatial and temporal error from effects of model parameters and governing equations.

For this purpose, we undertake a mesh refinement exercise. Using the same simulation scenario, successively higher resolution meshes are used so we can judge the rate of

convergence towards the solution given by the most accurate mesh (i.e. demonstrate point-wise stability). The conceptual problem for this exercise is adapted from Slough et al. [70]. The intersecting horizontal and vertical fracture set up is extended by adding another vertical fracture in the third spatial plane, as is visualized in Figure 3-5a. Diverging from [70], the porous medium problem is parameterized as a generic sandstone, with values derived from the SSFL site. Our intent is to detect any effects the spatial resolution of the mesh may have on fracture-matrix interaction.

Four complementary scenarios demonstrating site-relevant fracture-matrix interaction issues are investigated by the simple 3D fracture network shown in Figure 3-5: 1) NAPL invading aqueous phase-saturated rock (see Figure 3-5b) with the horizontal fracture below the water table; 2) water infiltrating into variably saturated rock with the water table at the bottom of the domain (see Figure 3-5c) and the horizontal fracture above the capillary fringe; 3) NAPL invasion with Scenario 2 taken as the antecedent conditions; and 4) NAPL invading variably saturated rock with an elevated water table such that the horizontal fracture is within the capillary fringe. Scenarios 1, 3 and 4 involve the NAPL being injected near the two-fracture intersection at the top. It then flows downward toward the three-fracture intersection in the centre of the domain. Recharge water is applied at a steady rate across the top of the domain, which creates a vertically downward flow regime. We refine the fractures separately from the PM in a manner analogous to Slough et al. [2] following their explanatory diagram Figure 7c.

In the NAPL-aqueous scenario, grid refinement within the fracture network is necessary to resolve the capillary forces that govern the direction of flow once the NAPL invades the intersection of the vertical and horizontal fractures. The outflow direction should be horizontal given that the horizontal fracture has a larger aperture than the vertical fracture. This hypothesis follows from the discussion in Section 3.2.1.2. Refinement in the matrix is of lesser significance given that the gravity-driven NAPL is not under sufficient pressure to enter the matrix pores. Capillary forces in the matrix force the NAPL to reside in the fractures. These hypotheses are consistent with the ones drawn by Slough et al. [2] in their analogous 2D exercise. We note that inclusion of the matrix continuum is a clear extension of the glass plate simulations in Section 3.2.1.2. The purpose of the following investigation is to provide insight into how model formulations and numerical considerations affect the evolution of the TCE NAPL source zone below the water table.

The aqueous-gas scenario exemplifies the difference in capillarity between the fractures and matrix (note the magnitude of fracture P_c Figure A-1b versus matrix P_c Figure A-1e) by strongly imbibing all infiltrating water from the fractures to the matrix. Thus, the matrix preferentially conducts infiltrating water, which leaves the fractures at residual aqueous phase saturation, S_{qr} = 0.02. This hypothesis is consistent with the results of Cey et al. [71] who numerically modeled infiltration events in fractured soils, and the experimental and modeling work of Roels et al. [72] who demonstrated that the dominant regime for the uptake of water is dependent on the fracture aperture, roughness, and PM properties. (We note the limited applicability of the experiment conducted in reference [72]: their experiment drew water upward into the matrix and a vertical fracture from an open-water source, whereas we model infiltrating water and the influence of horizontal and vertical fractures on a downward water flow path.) We anticipate that the strength of the capillary forces pulling the aqueous phase out of the fractures will be sufficient to immobilize the phase (i.e. put $S_q \leq S_{qr}$ such that $k_{r,q} = 0$) causing the fractures themselves to be non-conductive and/or to be barriers to fracture cross flow. Thus, this scenario is ideal for demonstrating sensitivity of fracture cross flow to asperity contact area. Ultimately, we hypothesize fractures serving as capillary barriers to flow of infiltrating water affect vadose zone saturation at larger spatial scales.

In the first aqueous-NAPL-gas scenario we anticipate that NAPL will flow primarily in the fracture network due to its higher permeability relative to the matrix. However, recalling that NAPL has intermediate wettability as compared to gas (least wetting) and aqueous (most wetting) phases both on fracture surfaces and in the pores of the rock matrix, this tendency may be precluded if capillary forces are sufficiently strong to draw NAPL into the matrix. Then, NAPL would displace gas for reasons analogous to water imbibition described above (except comparing Figure A-1c, lines A and B, versus Figure A-1f). As the saturation of NAPL increases above the residual value in the matrix, the nonaqueous phase will become mobile and gravity-driven advection will commence. NAPL will displace resident gas and aqueous phase in varying proportions as it migrates downward. Finally, if the NAPL is mobile in the fracture network at the intersection of the vertical and horizontal fracture, then we expect the NAPL to migrate sideways given that we constrain the horizontal fracture to have a smaller aperture relative to the vertical fracture. (Recall the results of the water-air wetting phase invasion simulations in Section 3.2.1.3, except we now substitute NAPL as the wetting phase, relative to gas.) The balance

of horizontal to vertical flow diversion at the fracture intersection will provide insight to the evolution of the TCE NAPL source zone in the aqueous-gas variably saturated regions in the vadose zone.

In the second aqueous-NAPL-gas scenario we hold many of the same hypotheses, except as follows. Because the capillary fringe now straddles the horizontal fracture we expect less imbibition of NAPL near the intersection and hence greater diversion of flow into the horizontal fracture. This complements the previous scenario by examining NAPL invasion and flow path choice in gas-filled fractures adjacent to aqueous phase-saturated PM regions. This is relevant in the capillary fringe proper or any other zone of high water saturation above the water table, which may occur e.g. due to geologic heterogeneity.

3.2.2.1 Numerical Representation of 3d Fracture-Matrix Domain

The domain for this suite of simulations is a 10×10×10 m cube as shown in Figure 3-5a. Three orthogonal fractures (two vertical and one horizontal) cross cut the domain. Boundary conditions at the bottom maintain the water table at an elevation of about z = 10.1 m in the aqueous saturated domain (see Figure 3-5b), at z = 1 cm for the variably saturated case (see Figure 3-5c), and at z = 3 m in the second variably saturated case (see Figure 3-5d). In the variably saturated cases, a capillary fringe exists that extends upwards to just below the horizontal fracture, or roughly centres itself on the horizontal fracture. The sides permit free entry of resident phases and/or exit of any phase. Two layers of CVs at the top of the domain inject recharge water and allow gas exchange in the variably saturated situation. NAPL is injected directly into the fractures at the top of the domain in a small radius centred at the vertical fracture intersection. This conceptual domain forms the basis for the grid refinement exercise.

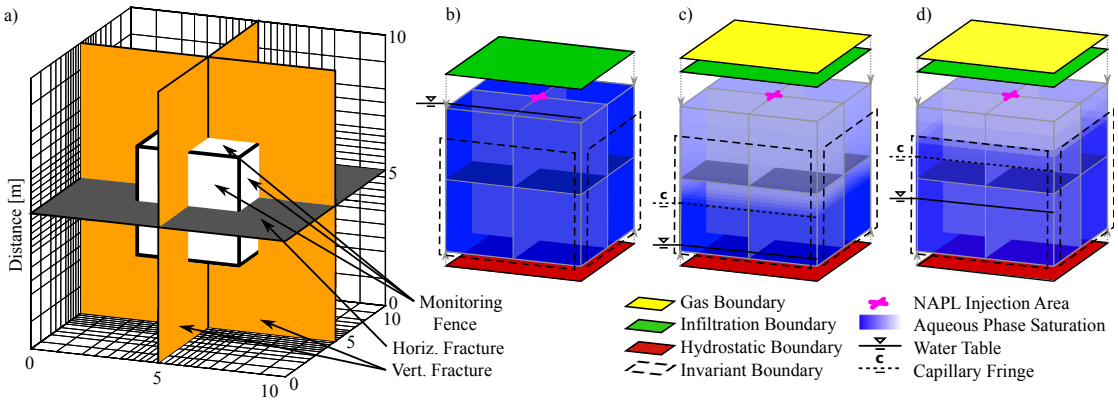

Figure 3-5 Domain discretization of the u25 simulation showing a) the three fracture planes, *monitoring fences* and spatial dimensions, b) boundary conditions and initial water saturation for

the NAPL-aqueous scenario, and c) and d) boundary conditions and approximate initial water saturation for the two aqueous-NAPL-gas scenarios.

The test scenario with the most refined grid uses the following sequence of CV sizes to fill the 5 m distance from the fracture to the side of the domain: five CVs at 1 cm each, three at 5 cm, three at 10 cm, four at 25 cm, three at 50 cm, one at 100 cm, one at 99 cm, and finally one at 1 cm. The 1 cm layers of nodes on the domain boundaries are used to hold the boundary condition source/sink terms. Scenarios with coarser grids follow the same sequence except the small CVs are replaced with one or more CVs of the next coarser size. Scenarios in this suite are named according to a convention that can be explained using two examples: 'u1' means that the fractures and porous media are discretized uniformly beginning the sequence at the 1 cm interval; 'm25-f1f5' means that the porous medium begins the discretization sequence at 25 cm, while the fractures have two additional layers of refinement with 1 cm and 5 cm CVs adjacent to fracture intersections. After the initial refined layers, fracture CVs boundaries align with the divisions in the matrix.

We note that the mesh u30 is significant as a reference given that the fracture density in some areas of the Chatsworth formation is 3 per metre, as a rough simplification of core measurements by [73]. Accordingly, we examine meshes that are coarser and finer than this reference to gain insight on how discretization may affect site scale simulation results.

In all cases, the vertical fracture apertures are 100 μm. In the high water table case (Figure 3-5b), the horizontal fracture aperture is 200 μm so capillary pressure at the intersection should induce lateral NAPL flow (recall the 371-650 TCE-water case in Section 3.2.1.2). In the lower water table cases (Figure 3-5c-d), the horizontal fracture aperture is 50 μm so, again, lateral NAPL flow is favoured (recall the 371-295 water-air case in Section 3.2.1.3). Intrinsic permeabilities of a 50, 100 and 200 μm fracture, by the cubic law are 8.3×10^{-10}, 3.3×10^{-9} and 1.3×10^{-8} m^2, respectively (see equation (5)).

Many physical and chemical parameters are the same as the glass plate simulations. Properties of the porous medium are outlined in the Appendix A. Asperity contact is fixed at 1% unless otherwise noted. Node elimination is used in all scenarios because many of the simulations proved computationally impracticable due to small time steps.

Because NAPL, aqueous and gas phases will now be present in the matrix, it is necessary to consider the relationships of phase saturation to relative permeability and

capillary pressure in a three-phase context. A discussion of the relevant parameters is given in Appendix A.

Boundary conditions for the NAPL-aqueous simulations include free-flow hydrostatic boundaries from z=0 to 7 m on each side and covering the bottom to maintain the water table at 20 cm above the top of the domain. No flow is allowed over the sides from z = 7 to 10 m to avoid potential interference between the top and side boundary conditions. Recharge is applied on the top face of the domain at a steady rate of 2.3 cm/year. This rate is based on 46 cm/year precipitation with about 5% of that infiltrating to the subsurface, as per the conditions at SSFL site [74]. Free-phase TCE is injected directly into a subset of fracture network CVs located just below the recharge boundary in a 25 cm radius of the vertical fracture intersection. It is injected for 30 days at a steady rate of 0.4 L/day. This rate and cross sectional fracture area for injection is consistent with reference [2] and represents $Ca \cong 1.2\times10^{-9}$ or 1.4×10^{-9} for NAPL invading aqueous or gas phase, respectively.

The aqueous-gas and aqueous-NAPL-gas simulations use a hydrostatic boundary on the bottom of their domains that maintain the water table at the specified elevations. Invariant boundaries, implemented by large volume nodes, allow free-flow of all phases from z=0 to 7 m on each side. These boundaries are introduced to the simulation in a similar fashion to the glass plate simulations. The gas pressure at the top boundary is maintained at 99.999 kPa by injection of the air component into the gas phase, or removal of all components within the gas and/or other phases. Recharge, at the rate specified above, is applied just below the gas boundary condition layer. TCE is injected in the same manner as above except for a 10-year duration. Injection commences at 10,000 days, which is an arbitrary time given to allow the aqueous and gas phases to reach a suitable equilibrium.

3.2.2.2 NAPL-Aqueous, Below the Water Table

Results of the NAPL-aqueous simulations are shown spatially in Figure 3-6 and in terms of flux over fences in Figure 3-7. Figure 3-6 shows the saturation of NAPL in the most refined test case, u1. In this case, NAPL displaces the resident aqueous phase in the fracture as it advances vertically downward from the injection point. At the intersection with the horizontal fracture nearly all of the NAPL is diverted laterally as expected due to the lower entry capillary pressure of the larger-aperture horizontal fracture. Additionally,

the high entry pressure of the matrix prevents imbibition, so all NAPL stays in the fracture network.

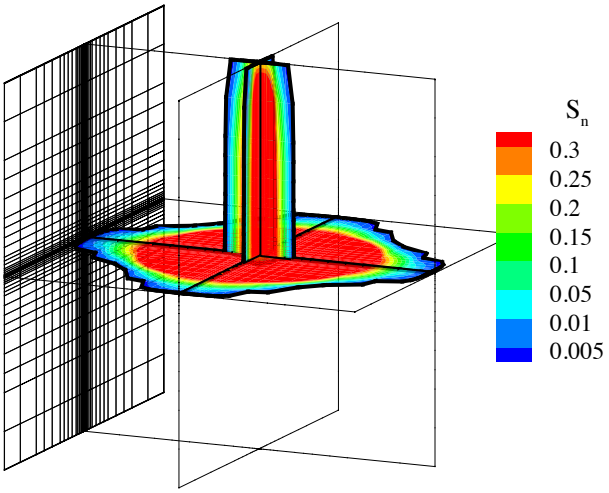

Figure 3-6 NAPL saturation in the fracture network (contours bounded by black lines) in the u1 case at 8.5 days. Narrow black lines on the left-hand boundary plane show the CV divisions that are applied in each direction.

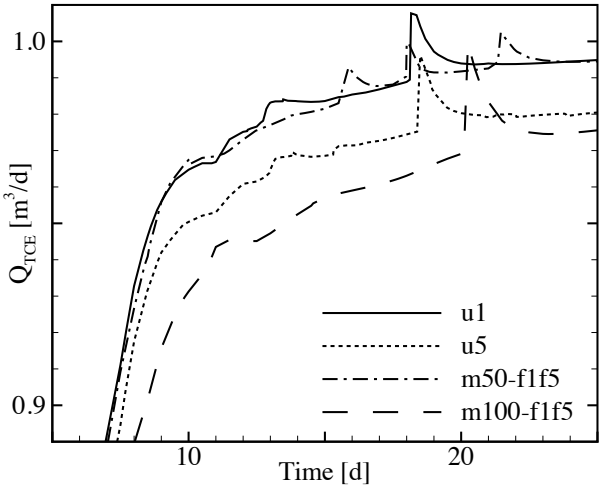

Figure 3-7 Horizontal flux of NAPL in the fracture network under varying levels of grid refinement. Flux is normalized by the NAPL injection rate.

Figure 3-7 shows the horizontal flux of NAPL across the four vertical monitoring fences (see Figure 3-5a). We select four specific refinement cases, u1, u5, m50-f1f5 and m100-f1f5, to compare. It is evident that in saturated conditions the size of porous media CVs is relatively unimportant as compared to refinement of fractures near the fracture intersection for NAPL diversion into the horizontal fracture. Several of the other simulations that lacked refinement near the intersection failed to divert more than 30% of NAPL into the horizontal fracture. However, as NAPL displaces aqueous phase in the

fractures it influences the phase pressure field in surrounding nodes. This propagates into the matrix and is not likely well resolved without a finer matrix CV discretization. The sharp spikes observed in the flow rates in Figure 3-7 occur when the NAPL front invades coarsely refined CVs at the periphery of the domain. The magnitudes are exacerbated by symmetry. Results of this exercise agree with Slough et al. [2] in that refinements of 1 cm and 5 cm in the fracture network provide adequate convergence to the u1 (most refined) solution. Given that the matrix CVs have sizes from 50 cm to 100 cm, the results also imply that matrix refinement beyond some interval yields little benefit to accuracy.

3.2.2.3 Aqueous-Gas, in the Vadose Zone

Figure 3-8 shows results from the aqueous-gas steady-state simulation with sensitivity of phase saturation profiles to asperity contact area, as well as the effect of grid refinement. Asperity contact varies from α = 0% to 20%. More specifically, Figure 3-8 shows the aqueous phase saturation versus depth in a scan line adjacent to the vertical fracture intersection. Vertical scan lines located elsewhere show identical S_q-z profiles, so this one is generally representative. Recharge water is distributed evenly over the top of the domain to both matrix and fracture CVs, but capillarity causes all infiltrating water to be imbibed into the rock matrix. This leaves the fractures at residual water saturation $S_{qr} = 0.02$ (i.e. $k_{rq} = 0$) and hence diminishes any influence their high intrinsic permeability may have on the flow field. The vertical fractures are parallel to the dominant advective flow direction of infiltration in the matrix and do not influence flow. The horizontal fracture is perpendicular to this flow direction and influences the water saturation profile equally at all areal locations by a capillary barrier effect. This is the effect we wish to highlight.

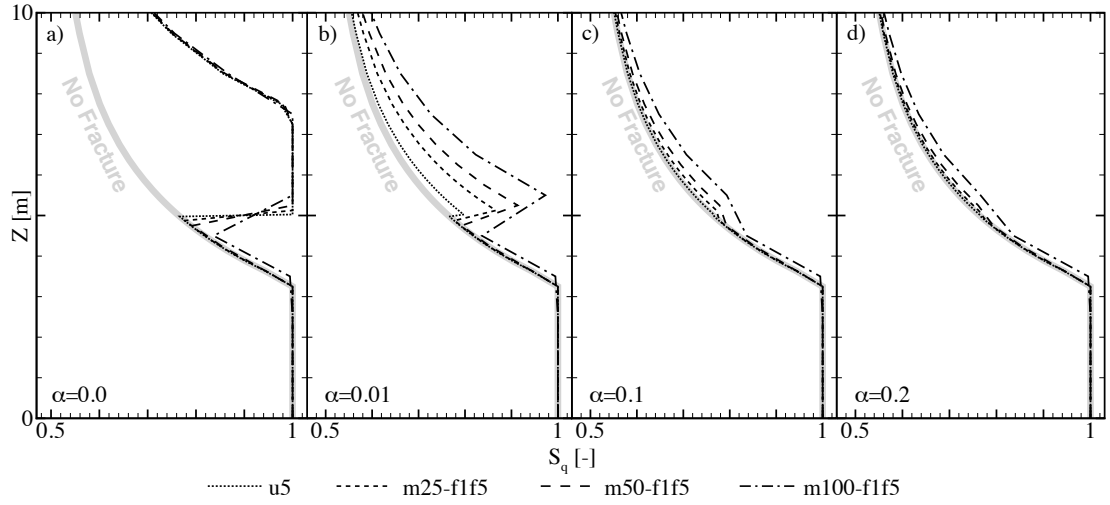

Figure 3-8 Aqueous phase saturation with depth in the porous medium in a column adjacent to the vertical fracture intersection. Asperity contact α varies in a) through d). Mesh refinement varies within each panel.

Figure 3-8a is unique in that the asperity contact area of α = 0% causes fractures to spatially disconnect the rock matrix. Thus, the horizontal fracture becomes a strong barrier to downward flow since aqueous phase must build sufficient head to breach the capillary barrier caused by the gas phase-filled fracture. This is evidenced by the fully aqueous phase-saturated region above the fracture. In this case, the grid refinement exercise shows excellent convergence to the u5 solution even with the coarsest mesh. The cases depicted in Figure 3-8b-d show the effect of using 1%, 10% and 20% asperity contact area, respectively. Using any amount of contact area causes the capillary barrier generated by the fracture to rapidly diminish. In these cases, the coarser mesh causes a stronger capillary barrier effect as evidenced by elevated aqueous phase saturations above the horizontal fracture with the effect diminishing as asperity contact increases. As asperity contact area increases beyond 20% the solution for saturation versus depth converges to the no-fracture curve.

This suite of simulations illustrates that asperity contact is an important control on aqueous phase saturation in the vadose zone. The sensitivity of the aqueous phase saturation profile to this parameter will undoubtedly vary with different matrix permeability, horizontal fracture aperture and fracture network density. Site-specific data may be used to constrain such parameters and to validate simulation results. As we shall see in the subsequent sections it is important to use appropriate antecedent water saturation conditions, as NAPL source zone evolution in the vadose zone is highly dependent on these conditions.

3.2.2.4 Aqueous-NAPL-Gas, Above the Capillary Fringe

The simulation results shown in Figure 3-9 are snapshots of the transient TCE NAPL source zone (the source) after 10 years of NAPL injection with asperity contact α = 1%. The sequence of simulations m50-f1f5, m25-f1f5, and u5 shall be referred to as the coarse, medium, and fine simulation, respectively. In terms of the grid refinement exercise, one must consider the effect of varying spatial accuracy on NAPL and gas flow in the fracture planes and on NAPL, aqueous and gas flow in the matrix through time, not just the NAPL as pictured. The antecedent water and air saturation conditions depicted in Figure 3-8b have a strong influence on the shape of the source since these phase saturations influence both the mobility and the potential for imbibition of NAPL from the fracture to the matrix continuum. Furthermore, because there is NAPL flow in the fractures and matrix, the cumulative effects of grid refinement in the direction perpendicular to flow (i.e. imbibition out of the vertical fracture into the matrix) and parallel to flow (i.e. NAPL in the matrix flowing downward across the horizontal fracture) are now present.

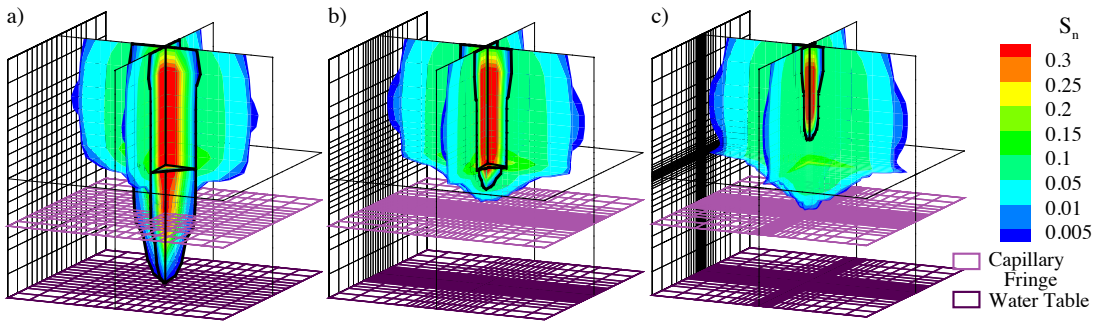

Figure 3-9 NAPL saturation in the fracture planes (contours bounded by black lines) overlaying the adjacent matrix (contours), water table, and capillary fringe in the a) coarse, b) medium, and c) fine simulations after 10 years of injection.

As the mesh is taken from coarse to fine, differences in the shape of the NAPL source's core in the fractures and its bulbous imbibition halo in the matrix are evident. The coarse simulation in Figure 3-9a shows an extensive vertical core that penetrates to the bottom of the domain in the fracture network. As this source develops, the NAPL front in the fractures leads the front of the imbibition halo. The converse is true for the fine simulation where, at one year of injection (not shown), the halo front overtakes the front in the fractures and thereafter leads the downward migration (shown in Figure 3-9c). The medium simulation in Figure 3-9b is intermediate to the previous cases. The NAPL front in the fractures leads for about 5 years or until it just penetrates the horizontal fracture, then the imbibition halo leads the depth and horizontal breadth of the source.

Despite the small aperture of the horizontal fracture very little flow is diverted laterally away from the vertical fracture in any of the simulations. This lack of lateral flow is contrary to the result of the 371-295, wetting invading non-wetting glass plate simulation. This difference occurs due to the absence of matrix in the glass plate scenario. This emphasizes the role of the matrix, specifically in imbibition scenarios, in determining the flow path. To further exemplify the impact of imbibition, at 20 years of injection in the fine simulation (not shown), the source's core in the fracture does not extend down to the horizontal fracture. However, the imbibition halo does cross the horizontal fracture via asperity contact bridging and extends down to the bottom of the domain.

A final observation about the imbibition halos in Figure 3-9 is the amount of NAPL held in the matrix above the horizontal fracture. Each mesh shows a capillary barrier induced by the gas-filled horizontal fracture. Similar to the perturbation in the S_q-z curve at the fracture in Figure 3-8, S_n-z in Figure 3-10 has an analogous kink.

Although a trend is evident, the source zones in the course and medium simulations do not show a clear convergence to the fine mesh solution shown in Figure 3-9. The combined effects of grid refinement (causing more imbibition) and the antecedent aqueous-gas phase saturation profile (leaving gas-filled pore space available for NAPL invasion) may be obscuring pattern towards convergence. Because it is difficult to isolate these effects, we present the following simplified summary: 1) in general, factures tend to guide the flow of NAPL in the vadose zone due to their high permeability relative to the matrix; 2) coarse meshes overestimate downward flow of NAPL in the fracture network; 3) coarse meshes underestimate imbibition of NAPL into the rock matrix; 4) in general, gas-filled horizontal fractures in the vadose zone act as capillary barriers that inhibit downward intermediate wetting and wetting phase flow in the matrix; and, 5) as matrix imbibition and matrix flow become the dominant processes for NAPL flux (e.g. when the matrix has low antecedent aqueous phase saturation characteristic of the region above the capillary fringe), they may preclude the error in flow diversion caused by CV elimination at fracture intersections where a wetting phase displaces a non-wetting phase (as observed in the glass plate simulations with no surrounding PM).

A result we did not anticipate appears in Figure 3-10. This figure represents the three-phase saturation versus depth profile adjacent to the vertical fracture intersection after 10 years of NAPL injection in the fine simulation. Based on the aforementioned order of

wettability we would have expected the invading NAPL to preferentially displace the gas phase, or cause a gas and aqueous double displacement [75]. Instead, we see an increase in the gas phase saturation accompanied by a decrease in the aqueous phase saturation. We believe this is caused by: 1) the S_n^* parameter in the $P_{c,nq}$-$P_{c,gl}$ blending equation (see equation (9)) because other simulations using $S_n^* = 0$ (not shown) exhibit the dominant decrease in gas phase saturation accompanied by a modest decrease in aqueous phase saturation as we had expected; or 2) by some combined effect of the boundary conditions and the highly contrived one-fracture-in-ten-metres conceptual scenario. Because few numerical models handling the invasion of NAPL into an aqueous-gas system have been created, the formulation of k_r-S-P_c relationships that transition from two to three phases is still an open area of research. (See, for example, theory put forth in van Dijke et al. [75], or theory and modeling in Fagerlund et al. [76].) At this point it is uncertain whether this unexpected displacement effect will be manifest in large scale or less contrived scenarios. Laboratory experiments conducted for the express purpose of quantifying P_c-S relationships as NAPL saturation increases from zero would help decide whether an acceptable value for S_n^* can be found or whether the formulation of the $P_{c,nq}$-$P_{c,gl}$ blending scheme should be modified.

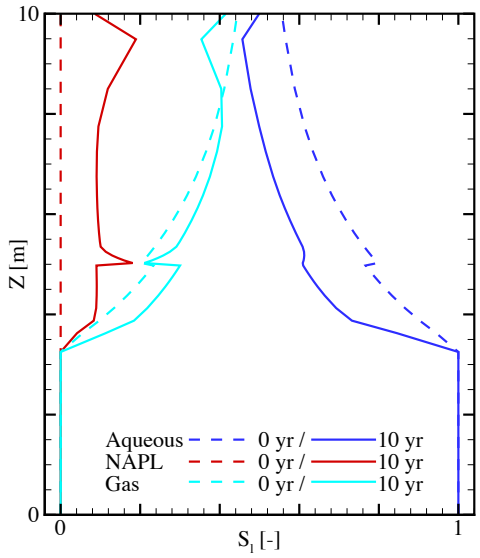

Figure 3-10 Phase saturations in the matrix adjacent to the vertical fracture intersection at 0 and 10 years with S_n^*=0.1 in the fine mesh simulation.

3.2.2.5 Aqueous-NAPL-Gas, Within the Capillary Fringe

The physical set up for the coarse, medium and fine simulations in this suite is similar to those in the previous section except that the water table is located at about z=3 m.

Accordingly, the results are similar, but the elevated capillary fringe and rarefaction in aqueous phase saturation leave less gas-filled pore space into which the NAPL may imbibe. The imbibition halo in each case is smaller than those seen in Figure 3-9 and NAPL penetrates to the bottom boundary of the domain in the fracture network in all cases because of less storage. Results of the fine simulation are shown in Figure 3-11 at three points in time that highlight interesting flow patterns that are somewhat contrary to our expectations.

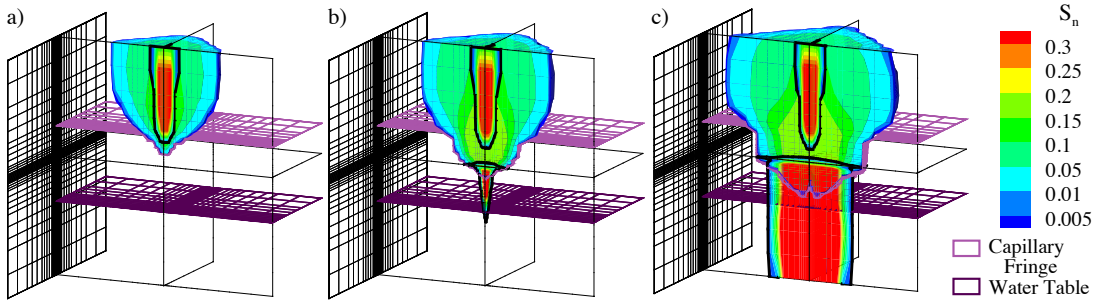

Figure 3-11 NAPL saturation in the matrix (contours) and fracture planes (contours bounded by black lines), water table location, and depressed capillary fringe in the fine mesh simulation after a) 2.5 years, b) 5 years, and c) 10 years of NAPL injection.

Our hypothesis that the NAPL would flow into the horizontal fracture due to capillarity and reduced NAPL storage capacity in the matrix (or rather, the hypothesis likening this scenario to the water-air glass plate experiment in section 3.2.1.3) was incorrect. What we observe instead is that imbibed NAPL above the capillary fringe forms a static column of pressure that, because TCE is denser than water, displaces the aqueous phase and depresses the top of the capillary fringe. This phenomenon begins after about 2.5 years of NAPL injection as seen in Figure 3-11a. With imbibition and matrix flow being the dominant process, fracture flow ceases and the imbibition halo migrates downward until it encounters the horizontal fracture. At this point, as depicted in Figure 3-11b, NAPL enters the horizontal fracture and continues downward migration in the fracture network. Apparently, the preferential flow path is from matrix to gas-filled fracture, rather than fracture cross flow into aqueous-saturated PM at the halo's leading edge. At later time, as in Figure 3-11c, the capillary fringe is depressed below the horizontal fracture, but the water table is unaffected as NAPL flow restricts itself to the fracture network.

The coarse and medium simulations (not shown) result in less imbibition above the capillary fringe when compared to the fine simulation pictured in Figure 3-11. Consequently, more NAPL is available to flow downward and a continuous path from injection

point to the domain bottom forms in the fracture network. The greatest difference in NAPL front location in these, as compared to the fine simulation, occurs at early time. Thus, the spatial discretization is again responsible for an initial overprediction in downward flux of NAPL. At 10 years time, the coarse and medium simulation both show increased NAPL saturation in the fracture below the horizontal fracture.

We conclude, in general, that if NAPL encounters a horizontal, gas-filled fracture in the capillary fringe or other area of near-unity water saturation, it may become a conduit for horizontal NAPL flow instead of merely participating in vertical fracture cross flow as in the previous aqueous-NAPL-gas case. This result further emphasizes the complex flow relationships between fractures and PM and the importance of k_r-S-P_c relationships in three-phase flow, and it builds the case for considering all types of flow as important when contemplating the evolution of a NAPL source zone, such as at the SSFL site.

3.3 Conclusions

Our ultimate goal is to produce 3D simulations of NAPL release from the ground surface at a scale that encompasses the terminal NAPL source zone. To achieve this we make simplifying assumptions so that small volume nodes at the intersections of fractures can be algebraically eliminated, thus removing undue constraints on the time step size. We also apply our novel formulation of asperity contact bridged flow. The topic hereof is the design and results of small scale test problems that investigate these two aspects. From these small scale exercises we have gained many insights about: capillary barriers to wetting and non-wetting phase flow at fracture intersections; flow direction at fracture intersections as dictated by capillarity; capillary barriers to fracture cross flow; rates of imbibition dependent upon grid refinement; and the importance of asperity contact bridged flow.

The effect of node elimination was observed in wetting phase and non-wetting phase capillary barriers and in determining flow direction at fracture intersections. For flow of NAPL in the saturated zone the impact of elimination is negligible. However, for wetting phase flow in the unsaturated zone strong temporal lags and differences in the proportion diverted to different discharge channels are observed to occur. As compared to cases with a centre node, node elimination causes a downward flow bias, unless horizontal outflow fractures are sufficiently small leading to a sideways bias. Although these discrepancies

exist, the node elimination technique has proven itself invaluable in larger simulations as the deciding factor between what is tractable and intractable.

Grid resolution has distinct effects in the saturated and unsaturated zones. In the saturated zone, refinement at the fracture intersections is important for determining the correct flow path under the influence of capillary forces. Refinement in the matrix does not appear to be as important in terms of NAPL and aqueous phase flow. Refinement would be necessary to abate numerical dispersion of dissolved species transport. In three-phase flow situations, grid refinement is important in two ways: 1) to reduce the apparent capillary barriers to wetting phase flow perpendicular to fracture planes; and 2) to increase the amount of imbibition perpendicular to the direction of NAPL flow. Poorly refined meshes will overestimate strength of capillary barriers at fracture planes and will underestimate the amount of wetting phase or intermediate wetting phase imbibition.

The notion of asperity contact in a rough-walled fracture is physically apparent and can be estimated by measurement of the properties of the porous media (see [60] and Appendix C). Asperity contact bridging has been newly added to this numerical model in a very simple fashion to allow a direct flow path between matrix CVs across a fracture plane. Absence of asperity contact creates a combined capillary pressure and relative permeability barrier to wetting flow perpendicular to fracture planes in the unsaturated zone. Presence of asperity contact quickly reduces this capillary barrier effect. Contact values of 1-20% of fracture surface area (with the permeability and infiltration conditions used here) remove the perched water table and nearly smooth the saturation versus depth curve.

Finally, a laboratory study of capillary pressure at an invading NAPL front (i.e. as a gas-aqueous, two-phase system transitions to a three-phase system) needs to be done to more definitively prescribe the form and parameters used in the equations to model such phenomena. These processes have a great influence on the mobility and storage of NAPL as a contaminant source zone develops.

Based on the numerical model's performance in these numerical exercises, we feel sufficiently confident to proceed with larger scale simulation runs that stylistically represent the nature of NAPL migration in a fractured porous medium. Results from future simulations must be interpreted carefully, given the biases exposed by these small

scale scenarios. Final defensible simulation results are contingent firstly on laboratory experiments of relative permeability and capillary pressure in the fracture network (that have yet to be done), and secondly on inclusion of more site specific geologic data. More complex geometry in the fracture network (e.g. non-orthogonal fracture orientations) and better utilization of computational resources (e.g. parallel computing) may be required to accommodate more realistic physical domains in the future. Before these more advanced tasks are attempted it is necessary to fully understand simplified and well-tested simulations of three-phase flow in discretely fractured porous media.

Chapter 4

Simulating Three-Phase Flow in Discretely Fractured Rock

Chapter Summary

In support of the remediation investigation of trichloroethylene (TCE) contamination at the Santa Susana Field Laboratory (SSFL) site, we present results of our recent numerical modeling efforts. The SSFL site sits on a local fractured sandstone bedrock topological high in the coastal mountain ranges near Los Angeles, California. We use the numerical simulator *CompFlow Bio* to model three-phase flow and transport in a fully coupled porous media and discrete fracture network (DFN) domain. We consider a portion of the near-surface vadose zone and shallow saturated zone in two and three dimensions on the spatial scale of 5-30 m where fracture density is 2-3 per metre. Specifically, we model steady and transient infiltration events to create antecedent aqueous-gas phase saturation conditions, then we inject a finite amount of dense, nonaqueous phase liquid (DNAPL) TCE into the fractured sandstone and allow the source zone to evolve for several years or, in one scenario, several centuries. This study highlights the need for asperity contact bridged flow in the vadose zone to create appropriate water saturation conditions, raises several discussion points related to the parameterization of three-phase numerical models, predicts a very long lasting DNAPL source in the vadose zone, and creates a base of work for future numerical source zone models for the SSFL site investigation.

4.1 Introduction

Many industrial sites in North America and worldwide have subsurface contamination by some toxic chemical originating from the facility located above. Managing the contamination at such sites is important to protect the groundwater resource because contaminated groundwater many affect ecosystems and human health. Management efforts commonly include numerical modeling to assess contamination and remediation scenarios.

The Santa Susana Field Laboratory (SSFL), located near Los Angeles, California, is one such site with trichloroethylene (TCE) contamination. As described by Cherry et al. [49], the SSFL sits atop a mountain elevated approximately 300 m above the valley floor and populated urban centres. The mountain is composed of fractured Chatsworth Formation bedrock, a turbidite sequence of sandstones with shale interbeds. Within the mountain, groundwater is mounded; the water table is found 3-20 m below the ground surface and water either discharges out of mountain-slope seeps or joins the regional flow system. The main contaminants of concern are TCE and its daughter products, which were introduced primarily in the late 1940s through early 1960s.

In support of the numerical modeling work of the SSFL site, the general topic of this study is the modeling of three components, TCE, water and air, in three mobile fluid phases, the nonaqueous phase, aqueous phase and gas phase, in a fully coupled porous medium (PM) and discrete fracture network (DFN) domain. Our goal is simulation of contaminant source zone architecture created when a dense, nonaqueous phase liquid (DNAPL) migrates through the vadose zone and down below the water table. More specifically, this study applies the unstructured mesh and fracture intersection elimination theory presented in Chapter 2, increases the complexity of the physical system from two phases in the Smithville site example in Chapter 2 to three phases, and extends the small scale exercises of fracture intersection flow and fracture-matrix interaction in Chapter 3 by increasing the geometric complexity of the fracture network. Although based in the context of contaminant hydrogeology, the multiphase, DFN modeling aspects described herein lend applicability to the fields of petroleum engineering, enhanced oil recovery, and carbon sequestration.

Numerical modeling of fractured rock dates back to the 1960s when the works of Warren and Root [8] and Kazemi [9] and Barenblatt et al. [11] were published; numerical models incorporating discrete fractures did not appear in the literature until the 1980s (e.g. Grisak and Pickens [12] and Noorishad et al. [13]). Studies modeling three-phase flow in porous media also began in the 1980s with the work of Abriola and Pinder [5]. Since then, and in parallel with increases in computational power, many numerical models with varying levels of physical and geometric complexity have emerged. Huyakorn et al. [77] put forth an early mathematical framework for multiphase flow in a dual porosity or DFN domain. The projects at Yucca Mountain have used numerical models extensively for saturated and unsaturated flow and transport simulation (e.g. Nitao and Buscheck [78] and Oldenburg and Pruess [79] and Wu et al. [80]). Included in this body of work is special treatment of fast, preferential flow paths in the fracture network caused by transient infiltration events (e.g. Liu et al. [21] and Finsterle et al. [81]). Hoteit and Firoozabadi [24, 27, 28, 29] have put forward several studies involving two-phase flow in complex fracture and PM systems with and without capillarity; Moortgat et al. [30] enhance this simulator to model compressible three-phase flow. Lesinigo et al. [31] model kinetic fluid flow of a single phase in fractures and PM.

This modeling effort unites many aspects of the other models/simulators described above. We consider compressible three-phase fluid flow with capillary pressure effects in a fully coupled DFN and PM domain. We also add aspects of fracture cross flow and use an unstructured spatial discretization. Chapter 2 describes the conceptual pathway of contaminant migration and source zone evolution that incorporates and elaborates upon the preceding phenomena. Embedded in this pathway are a number of key hypotheses that we wish to test here. Namely, now that we expand simulations from Chapter 3 to a field-relevant spatial scale and use a dense, well-connected DFN, we wish to explore: a) how fracture spacing and asperity contact influence the bulk transmissivity of the rock, particularly in the air-water system in the vadose zone; b) how transient infiltration affects water flow paths and water saturation in the vadose zone, and whether NAPL source zone architecture is affected; And c) the longevity of a NAPL source zone in the vadose zone when flushing by recharge water is the only means of TCE mass removal.

This chapter is structured as follows. We first present the conceptual problem, including key hydrological features related to the SSFL site investigation. We then describe,

in brief, the numerical simulator and, in depth, the numerical domains and boundary conditions used for the simulations. Results of 2D and 3D, air-water and air-water-TCE simulations are then presented. We finish with a number of discussion points regarding data needs for DFN models and prospects for future SSFL site simulations.

4.2 Methods

We divide our description of transforming the underlying conceptual scenario to computer simulation into three topics: the conceptual model, the numerical model and parameterization of the numerical model. The conceptual model describes the key hydrologic features of the site that we attempt to capture. We then briefly describe the numerical model *CompFlow Bio* and how we apply its features to the SSFL site problem. Finally, we describe the site specific and literature-based data that are used as parameters in the simulation.

4.2.1 Conceptual Model

We consider one basic conceptual scenario involving a volume of discretely fractured porous rock that extends from near the ground surface down to some distance below the water table as depicted in Figure 2-1. The spatial scale is on the order of 10 m. Spatially, the saturated zone represents about one third of the volume's depth. Because this depth is relatively shallow, we assume a vertically downward flow regime driven by gravity for the vadose and saturated zones. Precipitation and evapotranspiration occur at the ground surface, thus we consider only the water that infiltrates. Infiltration may occur either at a steady rate or at temporally varying rates corresponding to precipitation events. The long-term interaction of infiltration with the water table and fractured rock domain forms the antecedent conditions prior to contaminant release. TCE is loaded into the domain by introducing a NAPL onto the ground surface from where it can migrate downward by gravity and under the influence of recharge water. To translate this general scenario to the context of the SSFL, we apply the following data.

The spatial scale of the above-described scenario is adapted from general observations of the SSFL site. At the SSFL site, the water table sits at depths ranging from 6 to 24 m below the ground surface (mbgs) [49]. We take 20 mbgs to the water table and 30 mbgs as our target depths. The actual domain depth, areal extent, and depth to water table in the

2D and 3D model domains are subject to practical constraints, as described in the next section.

We simplify the PM to have homogeneous properties representative of Chatsworth formation sandstone. Specifically, we use the quantitative properties measured or derived from the rock core sample C4-137 as conducted by Amirtharaj et al. [82]. Fractures at the site are typically vertical or sub-vertical joints or parallel bedding plane fractures dipping at 25° to 30° [73] which we idealize as vertical or horizontal. As a rough aggregation of data from Kennel et al. [73] and Schlumberger Water Services [83], we set our target fracture density at 3/m and assign random hydraulic apertures, location, and length. As per the findings of Reitsma and Kueper [84], constitutive relationships developed for PM are applied to fractures. We parameterize these relationships with quantitative results gleaned from the numerical study of rough-walled fractures conducted by Mendoza [85].

The vertically downward flow system, corroborated in the site study by Abbey et al. [86], is developed in the model by the following boundary conditions. Infiltration and gas exchange with the atmosphere occurs at the top of the domain. We set the infiltration rate based on the average annual precipitation rate of 46 cm/yr [87]. McWhorter [74] found that infiltration is 2-7% of total precipitation. However, we round this to an even 10% for the current study. We consider either steady or transient infiltration based on this annual value. The data source we use for the transient scenario is the 2010 daily precipitation record measured at a nearby meteorological station, California Irrigation Management Information System station #204 [88]. This station is located approximately 25 km Northeast of the SSFL site in a similar geographic setting and at a similar elevation. We adjust this record to match SSFL mean annual precipitation. Montgomery Watson [89], as cited in [90], observed vadose zone water saturation in the range of 70-79%, which we take as an important point of calibration for the numerical model. The water table is set to the desired height by maintaining a constant hydrostatic pressure at the bottom of the domain. Lateral boundaries are impermeable. From a location near the top of the domain, TCE is introduced in the matrix and fractures. Gravity and concurrently infiltrating water may drive it downwards. We select the rate of injection as ~7 L/d, i.e. one “55 gallon drum” of TCE per month. We keep this loading rate constant between 2D and 3D domains to allow comparison of the contaminant source zones’ areal spread.

4.2.2 Numerical Model

We use *CompFlow Bio* numerical formulation as described in Chapter 2. In brief, *CompFlow Bio* is a three-phase, multicomponent, isothermal numerical simulator for flow and transport. It uses a first-order accurate, finite-volume numerical scheme to solve the multicomponent advection, dispersion equation in three spatial dimensions. A preprocessing step accepts stochastic parameters to create an axis-aligned fracture network and couples the network realization to the porous medium. Porous medium control volumes (CVs) are 3D, rectilinear entities. Fracture CVs are represented as 2D entities that are coupled to each other and the surrounding porous medium by Darcean flow and dispersive/diffusive transport flux terms. Porous medium CVs on opposite sides of a fracture plane communicate hydraulically via asperity contact bridged flow. Fracture aperture and effective hydraulic aperture are assumed equal for simplicity. Component species transfer between phases via equilibrium partitioning relationships.

Applying this framework to the conceptual model, we employ all three fluid phases (aqueous, nonaqueous, and gas phases) and consider three component species (water, TCE, and air). We represent fractured sandstone using the a stochastically generated DFN and by assigning the physical properties of Chatsworth formation sandstone to model CVs. We use the spatial formulation in a full 3D domain, and in pseudo-2D vertical cross section. Because the primary focus of this study is phase architecture we emphasize the role of advective flow processes over diffusive/dispersive transport.

4.2.3 Numerical Domains and Parameterization

In this section we describe a relevant subset of the parameters required for the numerical simulations: the domain discretizations and stochastic parameters for the DFN; intrinsic permeability of fractures and the rock matrix; k_r-S-P_c relationships for the fractures and rock matrix; and a description of boundary conditions (including the transient recharge histogram). A description of the remaining parameters, including fluid properties, equilibrium partitioning relationships, etc., may be found in Appendix A.

Figure 4-1 shows the two computational domains that we consider herein. The first is a pseudo-2D domain with dimensions 30×1×30 m in the *x*-, *y*- and *z*-directions. Fractures are restricted to *yz*-vertical or *xy*-horizontal orientations. The water table is at approximately z = 10 m. The second domain is 3D with dimensions 5×5×15 m. Fractures

are permitted in all three axial planes. The water table is approximately 2 m from the bottom of the domain. We note that we found it necessary to reduce the size of the 3D domain from our target size. Using three mobile phases, plus the number of CVs required to represent the matrix and discrete fractures, imposed a restriction on time step size; it proved impractical to consider a larger domain due to the computational burden.

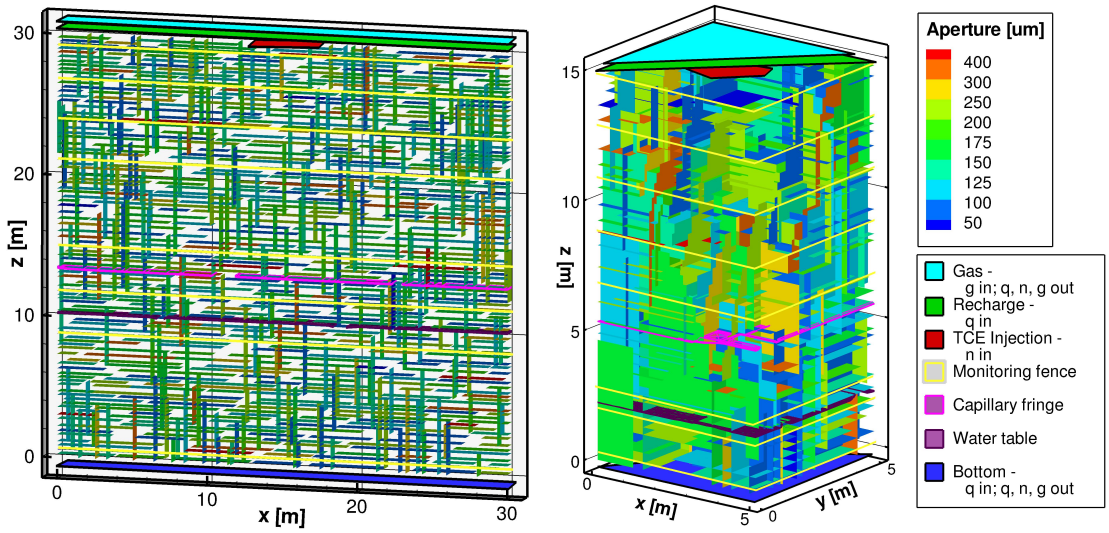

Figure 4-1 Domains for the 2D and 3D simulations showing discrete fractures, apertures, boundary conditions and monitoring fence locations.

In each case, we consider only one fracture network realization. The set of statistical parameters is common to both. Fracture apertures have been studied by a variety of test methods at the site (e.g. see Sterling [91], McWhorter and Reiners [92], and Kennel et al. [93]), which conclude that mean hydraulic aperture lies between 90-125 μm, depending on test location and method. We assume fracture apertures to follow a lognormal distribution with a geometric mean aperture of 150 μm and a variance of 0.2 m. Less is known about fracture length at the SSFL site; we choose fracture length in each spatial direction from uniform distribution between 2.0 m and 7.0 m. Aperture values in the resulting fracture network realizations are shown in Figure 4-2. Fractures are grouped into aperture-based "bins" for purposes described below. Table 4-1 and Table 4-2 show fracture length and density for each simulation. The descriptive statistics for fracture length are produced by considering all fractures; density is calculated from fractures hit by arbitrarily placed scan lines (three to seven in each axial direction), analogous to counting fractures that intersect a borehole drilled in rock.

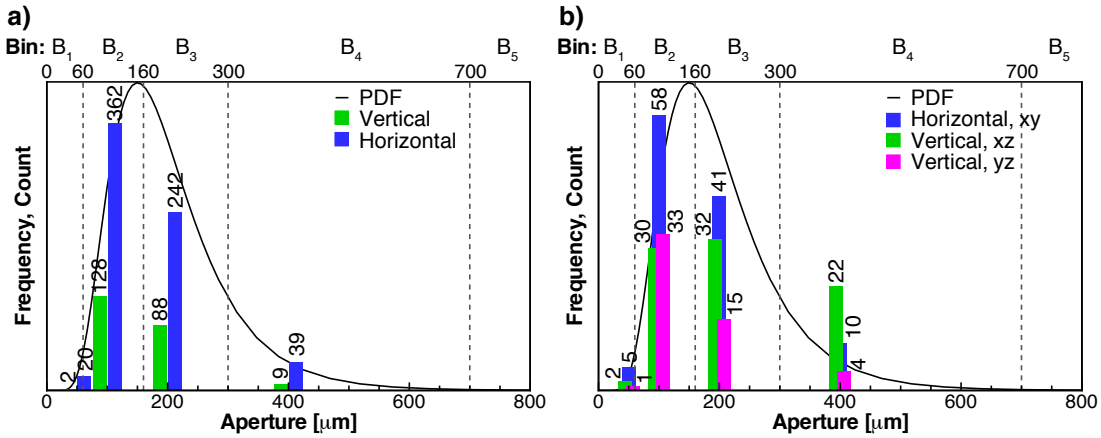

Figure 4-2 Statistical description of fracture aperture in a) the 2D and b) the 3D DFN realizations. Counts of fractures of each orientation are grouped by "fracture aperture bin," B_1 through B_5. The target probability density function (PDF) for fracture aperture (a lognormal distribution with 150 μm mean and 0.2 m^2 variance) is included for reference.

Table 4-1 Statistical description of fracture lengths in the 2D and 3D DFN realizations.

Sim., Direction	Min.	Max.	Avg.
2D, horizontal	1.1	7.1	3.4
2D, vertical	1.1	7.0	4.3
3D, horizontal, *x*	1.1	5.0	2.6
3D, horizontal, *y*	1.0	5.0	2.8
3D, vertical, *z*	1.4	7.1	4.3

Table 4-2 Average density of fractures in a given orientation in the 2D and 3D DFN realizations.

Sim., Frac. Orientation	Avg. Density [m^{-1}]
2D, horizontal	2.4
2D, vertical	1.0
3D, horizontal, *x*-*y*	2.2
3D, vertical, *x*-*z*	1.3
3D, vertical, *y*-*z*	1.5

Absolute permeability values for fractures are calculated using the effective hydraulic aperture in the cubic law as discussed in Chapter 2. The rock matrix simplified to be a homogeneous porous medium based on the C4-137 sample of Amirtharaj et al. [82]; its permeability is set to k_m=1.0×10^{-14} m^2.

For the purpose of assigning k_r-S-P_c relationships to fracture CVs we categorize them into five "bins" based on hydraulic aperture: <60, 60-160, 160-300, 300-700, and >700 μm, as depicted in Figure 4-2. Each bin is assigned a characteristic hydraulic aperture size of 50, 100, 200, 400, or 1000 μm, respectively, for calculation of capillary pressure. Full details of the method of calculating three-phase capillary pressure curves is given in Appendix A. We show the two-phase input curves for the five characteristic apertures and the blended three-phase relationships for the 200 μm fracture in Figure 4-3. The relative permeability relationships used in fractures were originally produced by Mendoza [85]. These data were derived from a model calibration exercise of a DNAPL-water system in a rough facture and we warily reuse Mendoza's $k_{r,nq}$ data for $k_{r,nq}$ and $k_{r,gn}$ for all fracture apertures. (A more recent study on upscaled constitutive relationships for water-gas systems in rough walled fractures may be found in Nuske et al. [94].) The final blended k_r versus three-phase saturation are shown in Figure 4-4. The rock matrix k_r-S-P_c relationships are shown in Figure 4-4 and Figure 4-5. Full discussion of these parameters may be found in Appendix A.

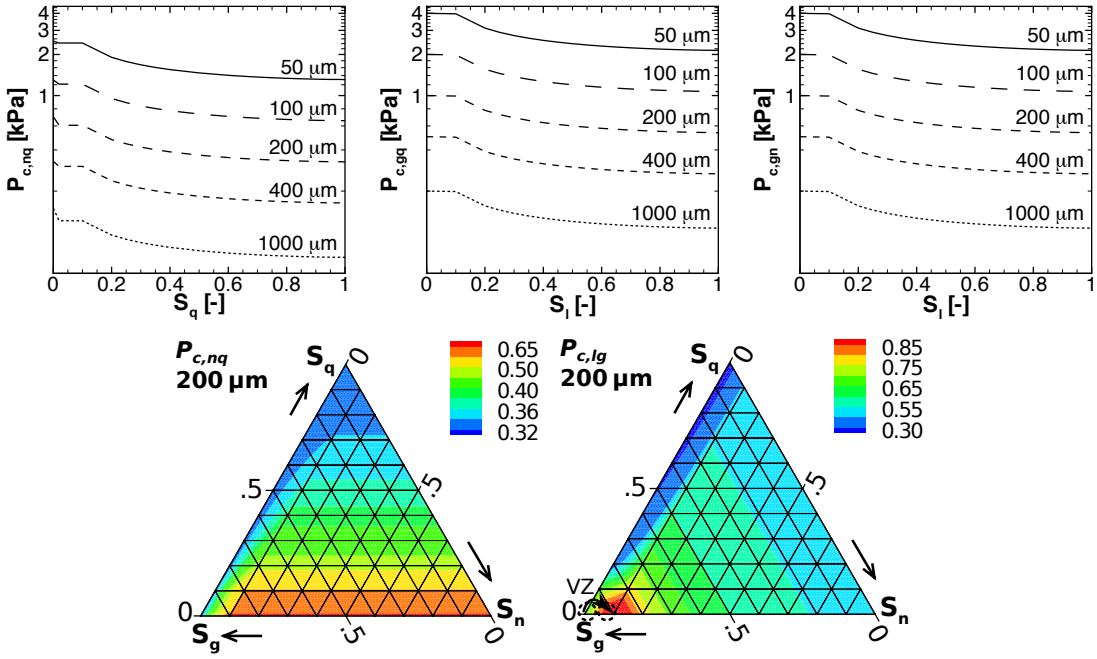

Figure 4-3 Two-phase capillary pressure (P_c) versus saturation relationships for all characteristic fracture apertures (top row) and the blended three-phase P_c relationships for the 200 μm fracture (bottom row).

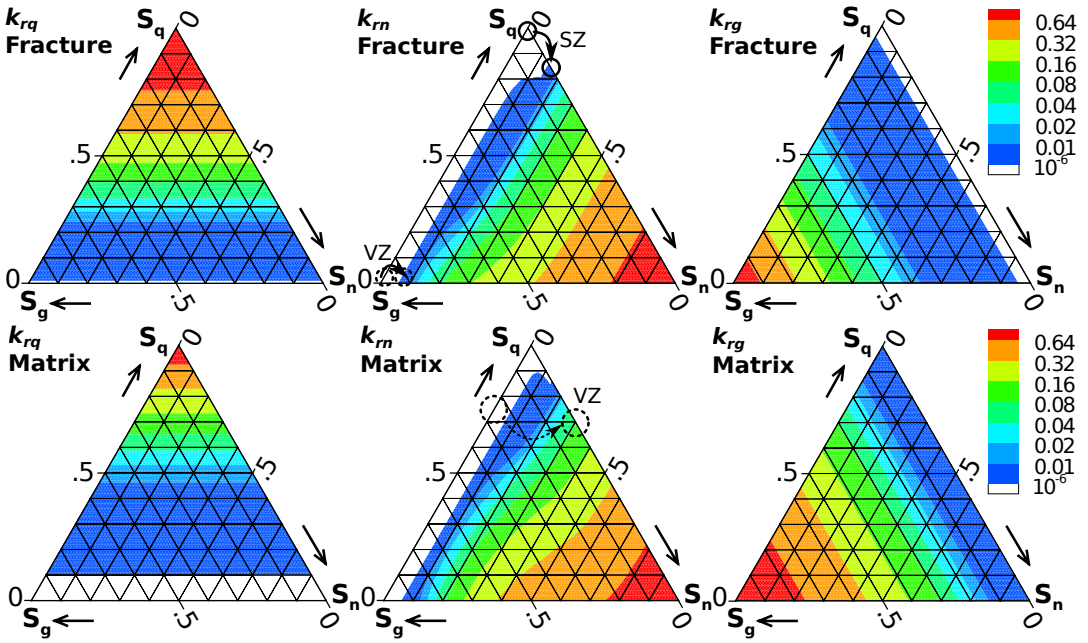

Figure 4-4 Relative permeability (k_r) of each phase versus three-phase saturation in fractures and in SSFL, sample C4-137, sandstone rock. k_{rn} plots are annotated with the approximate change in phase saturations from pre- to post TCE loading in the 2D, steady infiltration simulation in the vadose zone (VZ) and saturated zone (SZ).

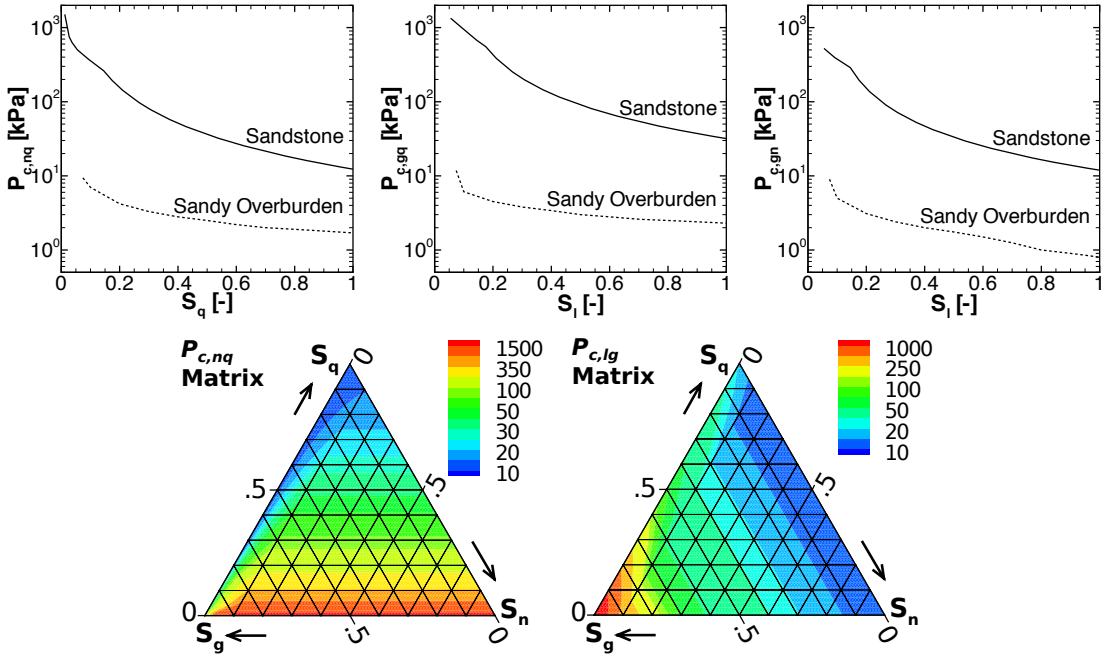

Figure 4-5 Two-phase capillary pressure (P_c) relationships for the sandstone rock matrix and overburden (top row) and the blended three-phase P_c relationships for the sandstone (bottom row).

The boundary conditions used in the numerical model to create the vertical flow regime and for TCE loading are depicted in Figure 4-1. Common to both the 2D and 3D simulations are gas boundaries in the top layer of CVs, recharge boundaries in the layer

below, TCE loading regions in the third layer, and hydrostatic boundaries in the bottom layer. Gas boundaries, which enforce a constant gas phase pressure, are set to atmospheric pressure, $P_{g,atm}$ = 100 kPa, for the duration of the simulation; they allow gas phase to flow in, and gas, aqueous, or nonaqueous phase to flow out to maintain the specified pressure. Recharge boundaries inject water into each host CV at a volumetric rate commensurate with infiltration rate and the surficial area in the *xy*-plane. In the case of steady infiltration this rate is constant through time. In the case of transient infiltration the rate changes daily according to the aforementioned precipitation record. The daily data from this station is scaled to reflect the mean annual precipitation at SSFL, multiplied by the 10% infiltration rate, and then repeated annually. Steady and transient infiltration rates are described further in Section 4.3.3 and are depicted in Figure 4-10a, TCE loading occurs in a relatively small number of fracture and matrix CVs near the top-centre of each domain at the constant rate stated above. The 2D simulation experiences two years of TCE injection, whereas, the 3D simulation experiences only 1.1 years of loading due to the extended computational time required for prolonged NAPL injection. (We found that NAPL reaches the bottom boundary at ~53 weeks of injection. Hence we set the injection period just long enough for this event to occur.) Finally, the bottom hydrostatic boundary condition is set at a constant aqueous phase pressure to maintain the water table at 10 m and 2 m in the 2D and 3D simulations, respectively. This boundary allows inflow of aqueous phase or outflow of the aqueous and/or nonaqueous phase.

4.3 Results

We present the results of the simulations in four parts. First, we examine only the gas-aqueous phase system to ensure we have created the desired hydrologic setting prior to NAPL injection. Second, we show 2D and 3D simulation results of NAPL injection with emphasis on the source zone architecture. Third, we focus on trends in the flow of water and TCE flow rates in the 2D simulation under steady and transient infiltration, which raise many discussion points about parameterization. Finally, we look at the 2D NAPL source zone architecture in long-term, which has relevance when compared to current site observations.

4.3.1 Antecedent conditions

Prior to reporting on the 2D and 3D simulations, we reinforce the importance of capillary barriers and discrete fractures to the overall saturation conditions in the vadose zone. The antecedent proportion of gas to water may have a strong impact on the amount of NAPL imbibed into the rock matrix pores due to the intermediately wetting nature of the nonaqueous phase. The following simulations address aqueous phase saturation conditions in multi-fracture systems.

4.3.1.1 1D Column Simulation

Although not the primary focus of this chapter, we conducted a numerical side-experiment modeling vadose zone water saturation in a 1D column. We use *CompFlow Bio* but modify key parameters and the domain to mimic other modeling paradigms, as described in Appendix B. The results in Figure 4-6 show, by adjusting the asperity contact ratio, α, and exploiting the capillary barrier effect caused by grid resolution near fracture planes, that the DFN model can tweak the aqueous phase saturation in the vadose zone. The line for 'RDFN 10%' in Figure 4-6 is taken from a scan line down the centre of the domain in the 2D simulation, and shows a vadose zone aqueous phase saturation of ~75%. This is within the target saturation range of 70-79%. The results of single continuum model (SCM), equivalent porous medium model (EPM), and dual permeability model (DK) show 60% water saturation in the vadose zone given "equivalent" parameters based on the site data. Details of these simulations and the calculation yielding α = 0.10 are found in Appendix C.

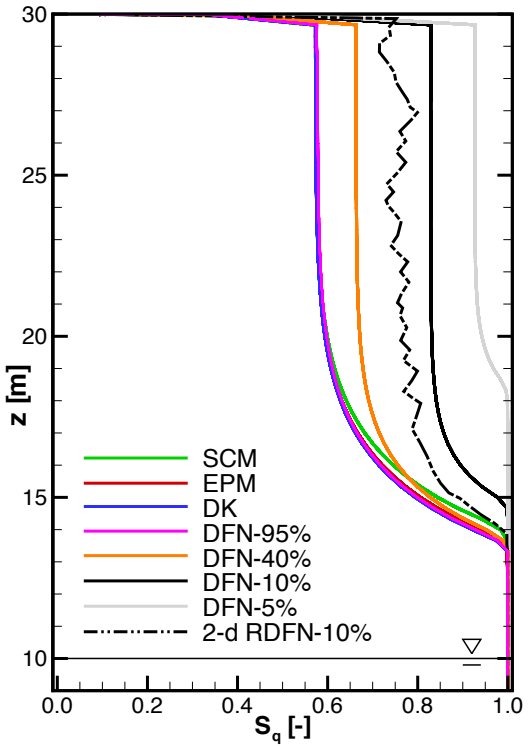

Figure 4-6 Comparison of simulated water saturation profiles (S_q) under different modeling paradigms: single continuum model (SCM), equivalent porous media (EPM), dual permeability (DK), discrete fracture network (DFN) with different asperity contact values (as %), and results of the 2D, steady infiltration simulation with a random discrete fracture network (RDFN) with 10% asperity contact.

4.3.1.2 2D and 3D Simulations

Figure 4-7 shows the saturation conditions that exist in the 2D and 3D, steady infiltration simulations in the matrix and fracture network prior to NAPL loading. Aqueous phase saturation in the fracture network of the 2D simulation is omitted due to similarities with the 3D results. We observe that the aqueous phase saturation is ~75% between the capillary fringe and top of the domain. As stated in the introduction, this value is dependent on the infiltration rate and other factors affecting bulk transmissivity. Qualitatively, we see that the aqueous phase saturation varies spatially, e.g. see Figure 4-7a-b. This variation is due to the influence of capillary barriers at randomly located fractures. As per our hypotheses, this heterogeneous saturation pattern will have some impact on the NAPL source zone architecture. Contrasting the 75% aqueous phase saturation in the matrix to that of the fractures, e.g. see Figure 4-7b-c, we see that fractures are nearly "dry;" their aqueous phase saturation is very near to residual. This is caused by strong capillary forces in the matrix causing imbibition out from the fractures.

Finally, we note the changes in the dominant flow paths at various depths in the 2D simulation domain, e.g. see the depth-ordered sequence in Figure 4-10a. In the vadose zone the rock matrix conducts between four and eight orders of magnitude more water volumetrically than the fracture network. Proceeding downwards into the capillary fringe water flow in the matrix remains dominant and is negligible in the fractures. Roles reverse in the saturated zone, where fractures become dominant for flow. The water flow we observe here is split between the fractures and the matrix in proportions of 97% to 3%, respectively. The vertical hydraulic gradient is about 0.015.

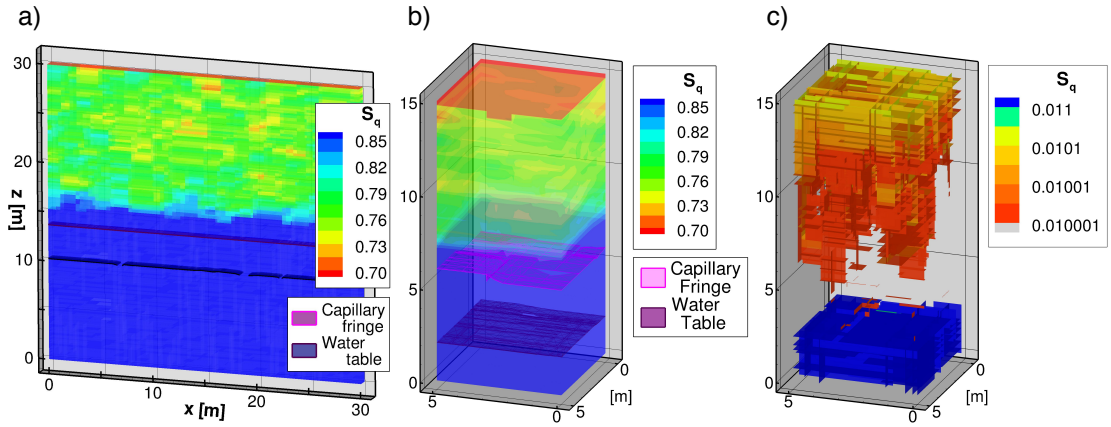

Figure 4-7 Water saturation (S_q) in the rock matrix at pseudo steady-state in the scenarios: a) 2D, with fracture CVs omitted, b) 3D simulation, with fracture CVs omitted, and c) 3D simulation with matrix CVs omitted.

4.3.2 Short Term Source Zone Development

To see how the DNAPL source zone develops during NAPL loading we present Figure 4-8 and Figure 4-9. Figure 4-8 shows NAPL saturation in the 2D and 3D, steady infiltration, simulations at times of one and two years since the beginning of NAPL loading. These images give us a general picture of the source zone's advancing front and architecture. Figure 4-9 expresses more quantitatively the changes in saturation of all three phases that occur from pre-NAPL invasion to the end of loading. It shows saturation versus depth in a vertical scan line.

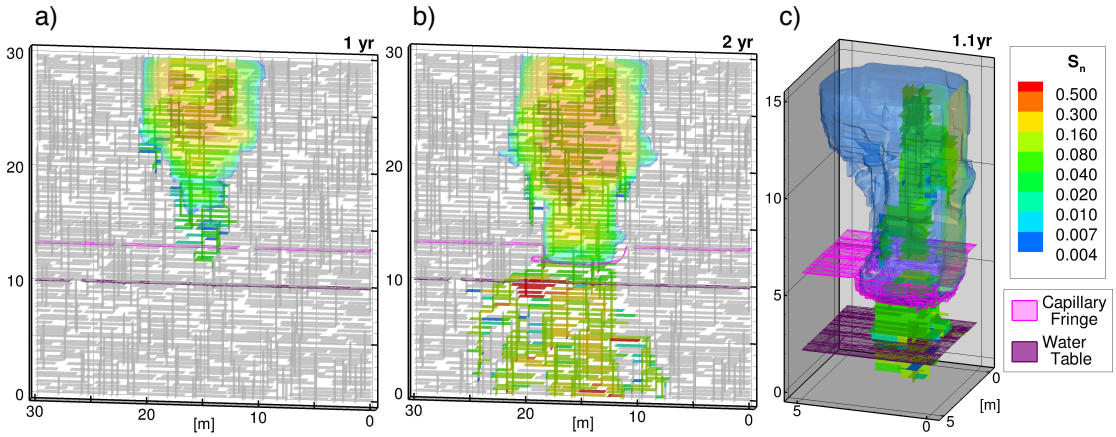

Figure 4-8 NAPL saturation (S_n) in the matrix and fractures at the middle or end of NAPL loading: a) 2D at 1 year, b) 2D at 2 years, and 3D at 1.1 years.

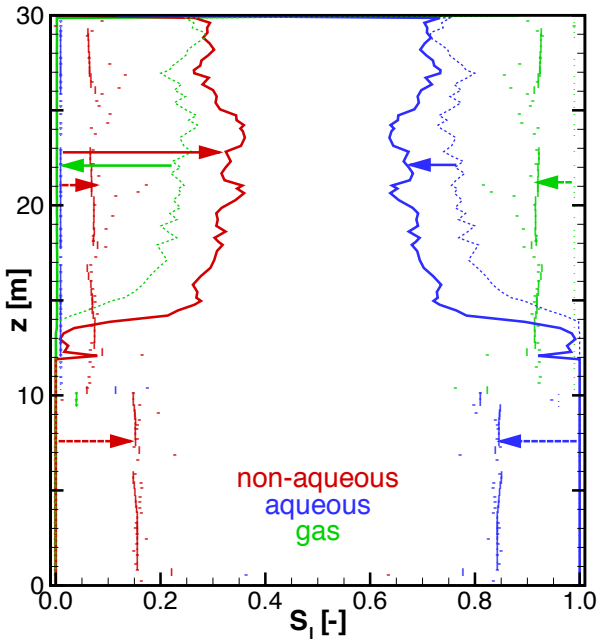

Figure 4-9 Phase saturations (S_l) along the scan line near x=15 m in the 2D simulation. Comparison of S_l before and after NAPL loading in the matrix (dotted lines/solid lines), vertical fractures (dots/bars), and horizontal fractures (dots/dashes). Arrows indicate trends in the change in phase saturations in the matrix (solid) and fractures (dashed) above and below the water table.

Figure 4-8 shows several characteristics of the developing source zone. First, from Panels a and b (the 2D simulation at one year and two years), we observe that the front of NAPL advances in the fracture network first and trails in the matrix. Thus, the fracture network has some influence, at least initially, on the advective path of NAPL. Panel c (the 3D simulation at the end of loading) most clearly shows the "imbibition halo" of the NAPL; the fluid has spread transverse to its gravity-driven, downward trajectory. In this case, the edge of the halo is several metres from the nearest NAPL-occupied fracture. Panels b and c

show that the NAPL depresses the capillary fringe in the matrix slightly, then continues its downward path below the water table in the fracture network only. Finally, Panel c shows that the source zone is vaguely cylindrical in shape, although we note some interference with the x = 0 m domain boundary.

Figure 4-9 is a saturation versus depth plot of all three phases taken from a vertical scan line from the 2D simulation. The scan line is taken at x = 15 m, which intersects rock matrix and horizontal fracture CVs; we allow ±0.35 m to include the data of five nearby vertical fractures. We differentiate data points from each of the three sources. Saturation values are shown at two times: before (i.e. Figure 4-7a) and after the two-year loading period (i.e. Figure 4-8b). From these figures, we make the observations that follow. Also, we refer back to the annotations in Figure 4-4 that show the change in capillary pressure and relative permeability values from pre- to post-loading in the vadose zone and saturated zone. These transitions correspond to the 'trend arrows' in Figure 4-9. Noting that there is variation in saturation values within the single scan line and undoubtedly variation between different scan lines, the saturation values we offer in the following discussion are approximate. We now discuss important changes in the vadose zone and saturated zone separately.

In the vadose zone, the post-loading NAPL saturation is about 30% in the matrix and 8% in fractures. The matrix achieves the value of 30% by vacating nearly all resident gas phase, S_g = 20%→2%, and some aqueous phase, S_q = 75%→65%. Two physical processes, imbibition from fractures and gravity-driven flow in the matrix, are responsible. We note that this transition in three-phase saturation puts $k_{rn,\text{Matrix}}$ (see annotation in Figure 4-4) well into its mobile range. Similarly in the fracture network, NAPL achieves pore occupancy at the expense of the gas phase, S_g = 98%→90%; no aqueous phase is displaced because S_q is already at its residual value. It appears that only certain horizontal fractures experience S_n > 6%; the three vertical fractures captured by the scan line have S_n = ~6%. In the latter case, Figure 4-4, $k_{rn,\text{Frac}}$, shows that the nonaqueous phase is only marginally mobile.

In the saturated zone, NAPL invades the fracture network only. The scan line shows no change to the aqueous phase saturation in the matrix. This indicates the expected change in flow regime from combined fracture and matrix flow in the vadose zone to exclusive fracture flow below the water table. The fracture data points in Figure 4-9 shows

a near-constant saturation of S_n = 15%. The nonaqueous phase is again only marginally mobile (see Figure 4-4, $k_{rn,\text{Frac}}$). Referring back to Figure 4-8b, certain localized areas of the fracture network reach S_n > 15%. Closer inspection of simulation results (not shown) reveal very high saturation values, e.g. S_n > 95%. Magnification of these localized areas reveals that these areas are dead-end fracture zones. We suspect that alternate flow paths and relatively small dead-end zones precluded the nonaqueous phase from gaining sufficient pressure to breach the capillary entry pressure of the surrounding porous medium.

4.3.3 Short Term Trends in Flow

Figure 4-10 shows rates of the water and TCE components in the 2D transient infiltration simulation crossing monitoring fences at different depths (refer to fences depicted in Figure 4-1). Rates are separated as fracture flow and matrix flow, where quantities represent the entire amount of a component (e.g. all free-phase plus dissolved TCE) crossing horizontal control planes. We express the flow rates as volume-per-unit-time to permit direct comparison with infiltration/loading rates at the top boundary. As discussed previously, Figure 4-10a shows water flow prior to commencing transient infiltration events and/or NAPL loading. Figure 4-10b expresses water flow rates before (t < 0 yrs), during (0 ≤ t < 2 yrs), and after (t ≥ 2 yrs) NAPL loading, where we consider the rates in -1 < t < 0 yrs to be the *base flow* patterns. Figure 4-10c emphasizes TCE flow rates in the same time periods. In the following description, we make reference to results of the 2D, steady infiltration simulation, but we omit them due to fundamental similarities to the transient simulation results. Likewise, we omit the results of the 3D, steady and transient simulations because they yield few additional insights relevant to this discussion. Here we briefly examine features in the aqueous-gas phase system of the transient simulation, the effect of TCE on water and the effect of water on TCE.

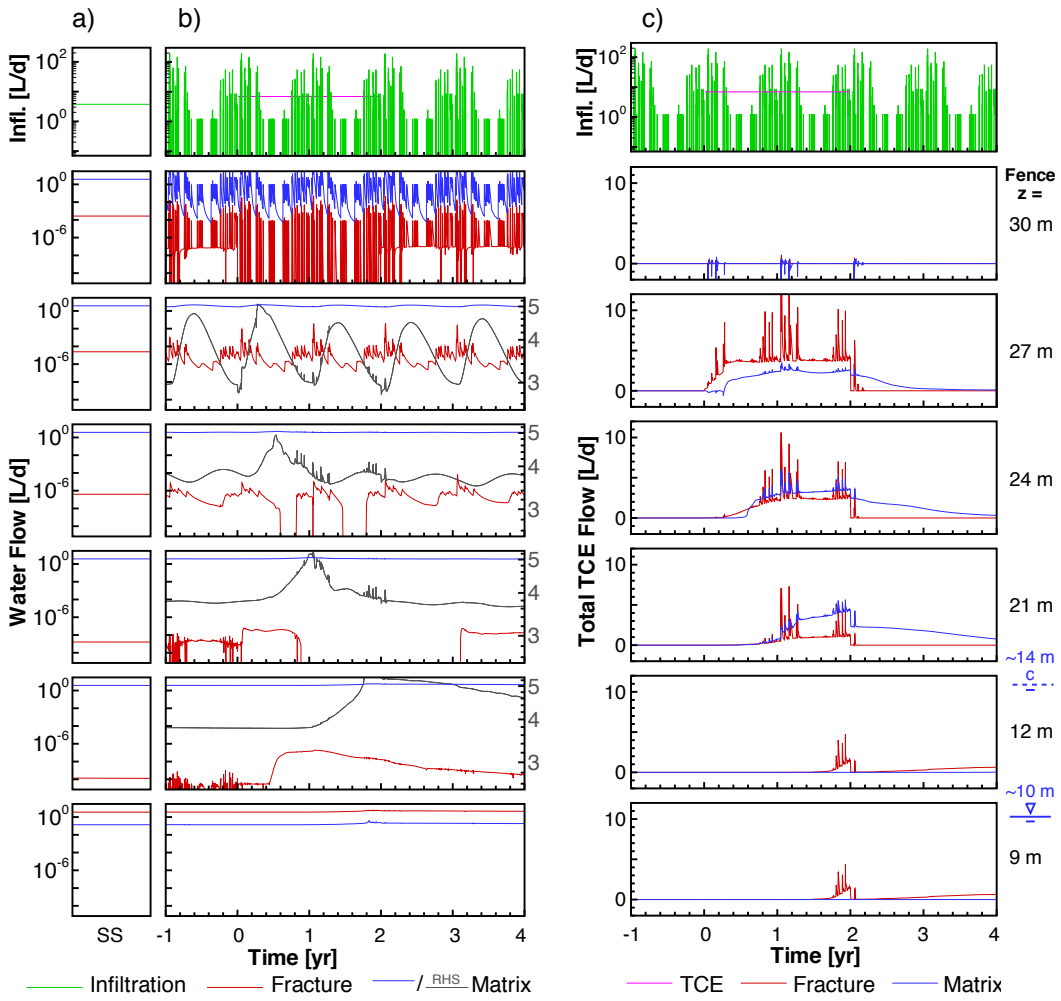

Figure 4-10 Water and TCE flow rates over monitoring fences (elevations listed on the right). a) Water recharge at the inflow boundary (green) and flow in fractures (red) and matrix (blue) at equilibrium/steady-state (SS). b) Histogram of daily recharge events and water flow versus time. Expanded right-hand-side (RHS) scale shows seasonal influence in matrix flow (gray). c) TCE injection rate (pink) and total TCE flow rates across monitoring fences versus time.

First, the fracture network and matrix have a different response time to daily time scale infiltration events, particularly in the upper vadose zone. Fractures respond quickly (i.e. changes in flow rates are timed closely with the infiltration event itself), whereas the matrix responds with a much higher latency. These two response times are evident in Figure 4-10b. Fracture flow rates have sharp peaks and troughs, whereas gradual, "seasonal" peaks and troughs occur in the expanded-scale view of matrix flow rates. These "seasonal" trends in the matrix become negligible at the depth z = 21 m. Conversely, short term disturbances in flow rates in the fracture network occur through the entire vadose zone and capillary fringe. However, the magnitude of these disturbances diminishes with depth. The potential consequence to seasonally varying infiltration rates is a change in the

pore occupancy of air in the rock matrix. I.e. there is a seasonally dependent amount of gas-filled pore space available for NAPL invasion and storage. Analogous to Figure 4-9 (but omitted), the S_q-z plot shows that the perturbation to gas saturation only reaches a depth of ~5 m from the surface; the post-NAPL injection S_n-z curve is identical to the one in Figure 4-9. Thus, the seasonal change in gas phase saturation has a negligible effect on resultant NAPL storage in this instance.

Three effects are apparent with respect to the influence of TCE on water flow rates. The first is a peak-shaped increase in the flow rate of water. This corresponds to the displacement of aqueous phase by NAPL that as noted previously (i.e. corresponds to the upper blue arrow in Figure 4-9). This can be seen or inferred from the deviation from the *base flow* rate in the z = 24, 21 m, and 12 m panels of Figure 4-10b, matrix flow RHS scale. This perturbation appears as a peak rather than a square-shaped pulse because the invading NAPL displaces only a fraction of the resident pore water as it establishes its downward flow path. The volume of displaced water increases as NAPL proceeds down through the vadose zone, hence, the perturbation at z = 12 m is greater in magnitude than the disturbances above. The second effect to water flow appears in the fracture network in the vadose zone and capillary fringe. TCE disrupts the antecedent flow rate pattern (t < 0 yr) in Figure 4-10b, panels z = 24, 21 and 12 m. These disruptions include periods when net upward flow occurs (depicted as a rate < 10^{-11} L/d or below the lower bounds of the scale). Because these flow rates (upward or downward) are orders of magnitude less than matrix flow, we do not consider them as a significant finding. The final effect is the presence of small magnitude spikes in the flow of water in the matrix. These do not obscure the seasonal trend in the plots of z = 21 m and above and they are not present in the steady infiltration simulation.

Finally, Figure 4-10c depicts TCE flow rates across the same set of monitoring fences. We distinguish between three types of TCE flow here: *loading-driven*, *infiltration-driven*, and *redistribution* rates. *Loading-driven* flow rates are evident at all panels below z = 30 m. These all increase from zero at times commensurate with NAPL arrival at the fence and drop abruptly at t = 2 years, i.e. at the end of loading. These *loading-driven* TCE flow rates are different from water flow in that neither matrix nor fracture flow overwhelmingly dominates the other. However, the relative dominance changes with depth. Near the top of the vadose zone fractures conduct most of the TCE, whereas the matrix is more dominant

at z = 21 m. This speaks to the importance of capillarity and fracture-matrix interaction as it impacts the flow regime of the invading NAPL in this system. Secondly, *infiltration-driven* flow, which does not occur in the steady infiltration simulations, appears as the sharp peaks in TCE flow rates that correspond with the sharp peaks in infiltration rates. These are more distinctly realized in the fracture network. Because these peaks are short in duration they do not contribute significantly to the bulk migration of TCE, nor the overall source zone architecture between the transient and steady infiltration simulations. Seasonal trends are not apparent in this instance. Thirdly, *redistribution* flow rates occur after the end of loading and appear as "tails" in the matrix flow rates in z = 27, 24, and 21 m in Figure 4-10c. These tails indicate changes in the architecture of the source zone driven by gravity acting on the nonaqueous phase.

4.3.4 Long Term Source Zone Evolution

Finally, we consider the long term evolution of the NAPL source zone under steady infiltration conditions. Results of the 2D, steady infiltration simulation are in the sequence of panels in Figure 4-11. These images range in time from 10 to 400 years post-loading. We are limited in our discussion to the 2D results because the 3D simulation has not reached such late-time results (as of the date of publication). The sequence in Figure 4-11 produces two main discussion points: longevity and long-term evolution of the source zone.

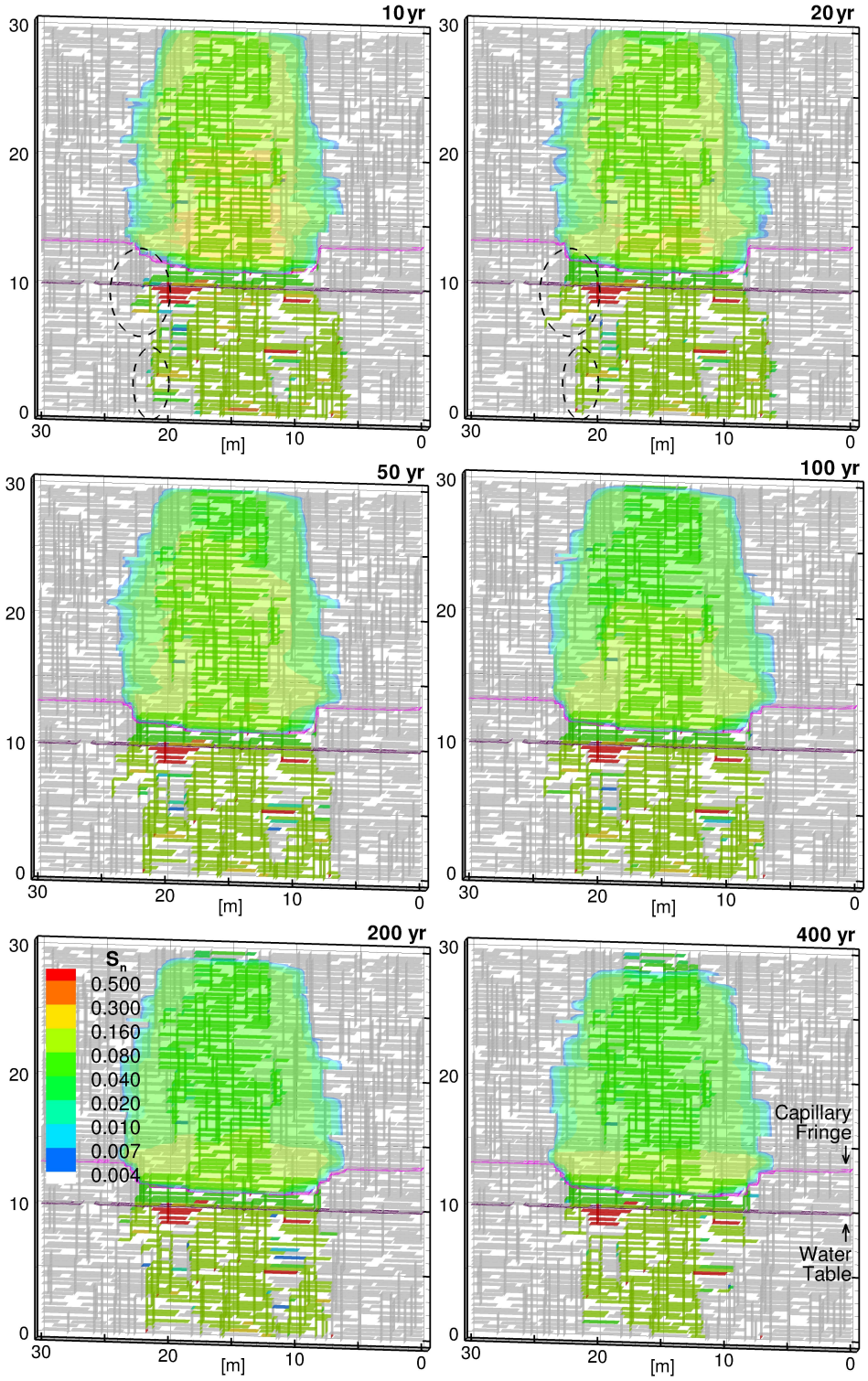

Figure 4-11 NAPL saturation (S_n) in the 2D scenario at various times past contaminant loading.

The first observation is that the source zone persists for a very long period of time. From a maximum of ~7200 kg TCE at the end of loading, ~3200 kg of TCE still exists in the domain at 400 years. This demonstrates that flushing alone is an ineffective means for

dislocating (or diminishing) the source zone. The fact that a large amount of mass is stored in the matrix in the vadose zone leads to recharge water being saturated with dissolved contaminant by the time it reaches the capillary fringe. Few of the saturated zone fractures below the core of the source zone lose any NAPL. The ones that do experience mass loss are below the periphery. At the top of the domain only a few metres of matrix material has been flushed by 200 and 400 years. The fractures in this "flushed zone" still hold NAPL near residual saturation.

A second observation is that the source zone continues to evolve. Certainly, when one compares the 2-year source zone depicted in Figure 4-8 with the 10-year image in Figure 4-11, it is evident that the architecture of the source zone changes greatly. The breadth of the source zone increases with time as capillary forces draw the NAPL sideways. More subtly, the source zone continues to advance in the saturated zone fracture network in the next 50 years. The two most prominent areas are highlighted by the ovals in the 10- and 20-year panels. Even after several decades since NAPL loading *redistribution* flows still occur.

4.4 Discussion

The methods and results described above prompt numerous discussion points stemming from challenges in parameterization, the model outputs, and observed limitations of the simulator. These points may be roughly categorized into the topics of importance of fracture cross flow, the need for additional laboratory and field data, reconciling model output with SSFL site observations, and the computational burden.

Contiguity in the porous medium is not inherent in DFN models as contrasted to equivalent porous medium or dual continuum models. *CompFlow Bio* exemplifies this by its fractures, conceptualized as parallel plates, that may completely separate adjacent matrix blocks. Thus, we must be careful to recapture that flow connectivity that is known to exist at rough-walled fractures in nature. Asperity contact, as introduced in Section 3.1, is our method of reestablishing this physical phenomenon. As demonstrated with the SSFL site example in Section 4.3.1 and in Appendix B, fracture cross flow is important in the vadose zone. In the vadose zone capillarity causes void fracture space to be gas-filled, and thus act as a barrier to aqueous and nonaqueous phase flow; asperity contact bridges allow wetting fluids to circumvent these barriers. Thus, in combination with fracture

spacing and matrix permeability, asperity contact and capillary barriers are very important in determining the unsaturated bulk permeability in the vadose zone.

It follows that the parameters used to create asperity contact bridged flow and capillary barriers are also very important to the simulation results. Namely, the asperity contact ratio, α, and the k_r-S-P_c relationships. This suggests the following field and laboratory measurements: to determine α, the elastic properties of the rock (i.e. Young's modulus), plus an estimate of the effective stress in the rock matrix at the depth of interest, must be obtained (see Appendix C for details); Second, appropriate k_r-S-P_c models and residual saturation parameters are crucial. From the results in section 4.3.2, we infer that nonaqueous phase flow in fractures is highly sensitive to residual NAPL saturation. Thus, these parameters are particularly important at the transition away from an aqueous phase only or a gas-aqueous phase system to one with a NAPL. van Dijke et al. [75] have developed theoretical relationships for k_r-S-P_c at such low nonaqueous phase saturations and Fagerlund et al. [76] have performed laboratory experiments of a NAPL invading a gas-aqueous phase system, but these are for PM. Analogous studies and results for rough-walled fractures are required.

Two points conceptually relevant to future SSFL site modeling efforts are: the agreement between the model's prediction of source zone longevity with SSFL site observations; and, as a minor point, the impact the NAPL loading mechanism may have on the source zone architecture. First, vadose zone core samples taken from various locations at the SSFL site show TCE concentrations well below its solubility limit in water (Anon [95], Table 7-8) decades after TCE was last released. Our model shows TCE in DNAPL form existing for centuries past loading. The foremost reason for this discrepancy is the omission of degradation processes from our model that are occurring at the site [96]. Recall that our model only considers advection and dissolved species transport; TCE may only be eliminated by outflow at a domain boundary. Although TCE persists for a very long time in the simulation we cannot deem the results as "conservative," i.e. the simulation does not necessarily produce the most long-lived source zone. The results of Unger et al. [97] suggest that kinetic phase partitioning models would protract dissolution of the NAPL source even more. Secondly, the conceptual method of TCE loading, i.e. steady-rate injector (see Section 2.2.4), may need reevaluation. We chose this source term due to its simplicity but the abrupt change in flow rate below the water table in Figure 4-10 may

indicate undue influence on the migratory path of the NAPL. We postulate that if the injection rate or fluid loading pressure had tapered towards the end of injection then the NAPL would not have been driven so deep. The result would have been more TCE mass residing in the vadose zone. Thus, the source term choice may have had an unintended impact on the NAPL source zone architecture. This prompts the question of whether this simulation artifact fits with the conceptual model of the SSFL site; for DFN modeling in general, modelers must be aware of the impact BCs may have given the highly permeable fracture flow paths.

Finally, we would like to comment on the computational burden of these simulations and to extrapolate these anecdotal experiences into prospects for foreseeable enhancements to the SSFL site source zone model. Two potential enhancements are: a) increasing the spatial scale or increasing the fracture density; and b) augmenting the physical system (e.g. adding component species relevant chain decay, biotic, or abiotic degradation). The 3D case presented herein represents the upper limit of what we can simulate in a practical way. The limiting factor in this case is the constraint on the time step size as imposed by nonlinearity in the physical system. We note that this is a different restriction than the one observed in Chapter 2, where the number of CVs (i.e. the size of the numerical system of equations) was the limiting factor. To overcome the current limitation, simplifications or tuning in the physical system will need to be made rather than the addition of "brute" computational power. Simplifications to the physical system may entail, for example, making the gas phase passive (i.e. use a Richards' equation-like approach). System tuning would require identifying and fixing problematic physical relationships or parameters thereof (e.g. the method of smoothing the k_r-S relationship near residual saturation as described in section 2.2.1, equation (9)). A third strategy is to identify the CVs that are holding back the time step and segregate them into a smaller numerical system (i.e. the "sub-time stepping" approach [98]). Thus, the prognosis for expanding the spatial scale and/or complexity of the physical system for future SSFL site modeling applications is highly contingent upon implementing one of the above-mentioned measures.

4.5 Conclusions

In summary, this study uses the numerical model *CompFlow Bio* to simulate antecedent water saturation conditions and the loading of a nonaqueous phase contaminant into the vadose and saturated zones of a discretely fractured, sandstone host

rock in 2D and 3D. Parameterized by many measurements and observations of the hydrogeological conditions at the SSFL site, the simulation results presented herein are a rare exposition of three-phase flow simulation in discretely fractured rock. The results highlight the need for further laboratory and experimental work to solidify certain model parameters and to provide data for more rigorous validation experiments. Based on the computational limitations experienced in the cases herein, results also indicate the need for some means to speed up the simulation so that larger, more field scale relevant simulations can be performed.

Chapter 5

Conclusions and Recommendations

5.1 Summary

In support of numerical modeling of DNAPL source zones in fractured porous media, this thesis covered the theory and basic testing of the new enhancements to the simulator *CompFlow Bio*. Chapter 2 explained the procedure of creating an unstructured mesh and eliminating CVs at fracture intersections and examined a suite of field scale, two-phase test simulations based on the Smithville, Ontario, site. Chapter 3 explained the theory of asperity contact bridged flow and examined small scale simulations that tested flow at fracture intersections and the effect of asperity contact ratio and grid refinement on two- and three-phase flow scenarios. The simulation results presented in Chapter 4 are the culmination of this thesis. We united aspects of the preceding chapters by performing 2D and 3D simulations with a dense fracture network at a field-relevant scale of an evolving DNAPL source zone based on the SSFL site. Such an exposition of a three-phase DFN simulator is rare in the scientific literature and thus represents the most significant contribution of this research.

We conclude by summarizing some specific findings and making recommendations about how *CompFlow Bio* may be further tested or enhanced.

5.2 Conclusions

Our overall conclusions fall into three categories: biases to flow and transport caused by choices in spatial discretization; the importance of certain simulation parameters; and a general evaluation of the simulator.

Error caused by temporal and spatial discretization of the governing equations is inherent in all numerical simulation. In Chapter 2 and Chapter 3 we saw numerous instances where error due the spatial discretization of fractures, the porous medium, or both, manifests itself by enhancing or diminishing some physical flow phenomenon. As a means to moderate the interpretation of future *CompFlow Bio* simulation results Table 5-1 summarizes these biases.

Furthermore, the investigation in Chapter 4 yielded information about the importance of certain parameters:

- Elastic properties of the rock on the asperity contact ratio, effective hydraulic aperture and hence the bulk permeability of the porous medium in the vadose zone and saturated zones;
- Capillary pressure, in the formation of capillary barriers and in imbibition of wetting fluids from fractures into the matrix; and
- Residual NAPL saturation and the k_{rn}-S relationship, in determining the saturation at which downward migration of the nonaqueous phase could occur in fractures in the vadose and saturated zones.

The numerical model *CompFlow Bio* has a number of limitations as reported. However, it has performed well in key areas with respect to the SSFL site investigation. Based on:

- Inputs of water infiltration data (derived from chloride mass balance studies at the SSFL site);
- Inputs of geomechanical properties of rock, fracture network characteristics, and fluid constitutive relationships (derived from core sample measurements and site observations);
- Agreement of water saturation model outputs with field data; and
- Plausible predicted realizations of the NAPL source zone architecture,

we conclude that the model has yielded some key insights into subsurface flow and is worthy of continued development and use.

Table 5-1 Summary of biases to flow caused by various spatial discretization choices.

Mesh Option			
	Elimination of Fracture Intersection CVs	VZ	q-phase and n-phase: Elimination 1) removes temporal lag in intersection breakthrough, and 2) affects proportion of flow in each outflow branch (Section 3.2.1.3).
		SZ	n-phase: Negligible effect (Section 3.2.1.2).
	Refinement of Fracture CVs at Intersections	VZ	q-phase and n-phase: No effect observed due to strong imbibition from fracture to matrix. (Section 3.2.2.4)
		SZ	q-phase: Increased flow (Section 2.3.4). n-phase: Poor resolution may cause downward bias in flow direction but resolution of matrix adjacent to fracture intersections may override this effect, (Section 3.2.2.2).
	Refinement of Porous Medium CVs	VZ	q-phase and n-phase: Increases fracture cross flow (Section 3.2.2.3). n-phase: Increases imbibition transverse to flow direction (Section 3.2.2.4).
		SZ	q-phase: Increase bulk permeability (Section 2.3.4). n-phase: Decreases fracture flow; decreases source zone extent (Section 2.3.3).

Note: Omissions from the list above indicates that no specific tests were performed for this option. Abbreviations: vadose zone (VZ); saturated zone (SZ); aqueous phase (q-phase); nonaqueous phase (n-phase).

5.3 Recommendations for Future Research

5.3.1 Analysis of the Current *CompFlow Bio* Code

Although many efforts have been made to asses the role of numerical error in this simulator, we note several aspects that would be valuable to quantitatively bound the error. Many tests could be performed but we suggest two of critical importance:

- Assess the fracture flow rates, bound the rates of flow for which the assumption of laminar flow is acceptable.

- Quantify the error incurred by the structured mesh (e.g., revert to single phase (water only flow) to pumping tests in a confined aquifer varying structured vs. unstructured vs. fracture network realizations.)

5.3.2 Enhancements to the *CompFlow Bio* Code

At this point two types of enhancements are recommended for the *CompFlow Bio* code: firstly, due to the long computation times required for certain simulations herein, we put forward enhancements to speed up simulation runs. The two main themes of enhancements to increase speed are simplification in the physical system and improved use of computational resources; secondly, enhancements to incorporate additional physical aspects that affect multiphase fluid architecture.

Simplification in the physical system:

- Removing the active gas phase, e.g. reverting to a Richard's equation-like formulation for liquid flow in the vadose zone.

Improved use of computational resources:

- Dynamically adding/removing equations when they are/are not needed to keep the numerical system as small as possible;
- Renumbering control volumes to improve locality of node data stored in computer memory and hence improve cache performance. Additionally, this enhancement helps prepare for domain partitioning needed for parallel computing; and
- Parallelization of the matrix building and solution phases of the numerical system of equations.

To include other physical phenomena that influence NAPL source zone architecture, we recommend:

- Enhancing the mesh generator to include non-orthogonal fracture sets;
- Incorporating non-axis aligned anisotropy to the PM permeability tensor (e.g. [99]; and

- Including hysteresis in the relative permeability-saturation-capillary pressure (k_r-S-P_c) relationships to better model fluid entrapment and changes in fluid mobility in advancing front versus retreating situations.

References

[1] Unger A, Sudicky E, Forsyth P. Mechanisms Controlling Vacuum Extraction Coupled with Air Sparging for Remediation of Heterogeneous Formations Contaminated by Dense Nonaqueous Phase Liquids. Water Resources Research. 1995, August;31(8):1913-1925.

[2] Slough K, Sudicky E, Forsyth P. Grid refinement for modeling multiphase flow in discretely fractured porous media. Advances in Water Resources. 1999, November 1;23(3):261-269.

[3] Slough K, Sudicky E, Forsyth P. Importance of rock matrix entry pressure on DNAPL migration in fractured geologic materials. Ground Water. 1999, March-April;37(2):237-244.

[4] McLaren RG, Sudicky EA, Park Y, Illman WA. Numerical simulation of DNAPL emissions and remediation in a fractured dolomitic aquifer. Journal of Contaminant Hydrology. 2012, August;136:56-71.

[5] Abriola L, Pinder G. A multiphase approach to the modeling of porous-media contamination by organic compounds .1. Equation development. Water Resources Research. 1985;21(1):11-18.

[6] Parker B, Gillham R, Cherry J. Diffusive Disappearance of Immiscible-Phase Organic Liquids in Fractured Geologic Media. Ground Water. 1994, September-October;32(5):805-820.

[7] Narasimhan T. Multidimensional Numerical-Simulation of Fluid-Flow in Fractured Porous-Media. Water Resources Research. 1982;18(4):1235-1247.

[8] Warren J, Root P. The Behavior of Naturally Fractured Reservoirs. Society of Petroleum Engineers Journal. 1963;3(3):245-255.

[9] Kazemi H. Pressure Transient Analysis of Naturally Fractured Reservoirs with Uniform Fracture Distribution. Society of Petroleum Engineers Journal. 1969;9(4):451-462.

[10] Reiss L. The Reservoir Engineering Aspects of Fractured Formations. Gulf Publishing Co.; 1980.

[11] Barenblatt GI, Zheltov IP, Kochina IN. Basic concepts in the theory of homogeneous liquids in fissured rocks. J. Appl. Math. Mech. Engl. Transl.. 1960;24(5):1286-1303.

[12] Grisak G, Pickens J. Solute transport through fractured media .1. The effect of matrix diffusion. Water Resources Research. 1980;16(4):719-730.

[13] Noorishad J, Ayatollahi M, Witherspoon P. A Finite-Element Method for Coupled Stress and Fluid-Flow Analysis in Fractured Rock Masses. International Journal of Rock Mechanics and Mining Sciences. 1982;19(4):185-193.

[14] Cokuner G, Hyde T. Homogeneous equivalents of naturally fractured porous media for miscible fluid displacements. Journal of Petroleum Science and Engineering. 1998, March;19(3-4):145-157.

[15] Lee R, Ketelle R, Bownds J, Rizk T. Aquifer Analysis and Modeling in a Fractured, Heterogeneous Medium. Ground Water. 1992, July-August;30(4):589-597.

[16] Balfour DJ. Evaluation of lateral solute migration in surficial weathered clayey till [Master's thesis]. Ontario, Canada: University of Waterloo; 1991.

[17] McKay L, Gillham R, Cherry J. Field experiments in a fractured clay till .2. Solute and colloid transport. Water Resources Research. 1993, December;29(12):3879-3890.

[18] Jorgensen P, McKay L, Spliid N. Evaluation of chloride and pesticide transport in a fractured clayey till using large undisturbed columns and numerical modeling. Water Resources Research. 1998, April;34(4):539-553.

[19] Kazemi H, Gilman JR. Multiphase flow in fractured petroleum reservoirs. In: Bear J, Tsang CF, de Marsily G, editors. Flow and Contaminant Transport in Fractured Rock. Academic Press; 1993.

[20] Ngien SK, Rahman NA, Lewis RW, Ahmad K. Numerical modelling of multiphase immiscible flow in double-porosity featured groundwater systems. International Journal for Numerical and Analytical Methods in Geomechanics. 2012, July;36(10):1330-1349.

[21] Liu H, Doughty C, Bodvarsson G. An active fracture model for unsaturated flow and transport in fractured rocks. Water Resources Research. 1998, October;34(10):2633-2646.

[22] Sarma P, Aziz K. New transfer functions for simulation of naturally fractured reservoirs with dual-porosity models. SPE Journal. 2006, September;11(3):328-340.

[23] Unger AJA, Bodvarsson GS, Simmons AM. Simulating infiltration in unsaturated basalt for the Large-Scale Aquifer Pumping and Infiltration Test at INEEL [Simulation de l'infiltration dans des basaltes non-saturş pour des tests à grande échelle de pompage et d'infiltration à l'INEEL]. Journal of Hydraulic Research. 2004;42(Extra Issue):105-113.

[24] Hoteit H, Firoozabadi A. An efficient numerical model for incompressible two-phase flow in fractured media. Advances in Water Resources. 2008, June;31(6):891-905.

[25] Reichenberger V, Jakobs H, Bastian P, Helmig R. A mixed-dimensional finite volume method for two-phase flow in fractured porous media. Advances in Water Resources. 2006, July;29(7):1020-1036.

[26] Geiger S, Matthaei S, Niessner J, Helmig R. Black-Oil Simulations for Three-Component, Three-Phase Flow in Fractured Porous Media. SPE Journal. 2009, June;14(2):338-354.

[27] Hoteit H, Firoozabadi A. Multicomponent fluid flow by discontinuous Galerkin and mixed methods in unfractured and fractured media. Water Resources Research. 2005, November 10;41(11).

[28] Hoteit H, Firoozabadi A. Compositional modeling of discrete-fractured media without transfer functions by the discontinuous Galerkin and mixed methods. SPE Journal. 2006, September;11(3):341-352.

[29] Hoteit H, Firoozabadi A. Numerical modeling of two-phase flow in heterogeneous permeable media with different capillarity pressures. Advances in Water Resources. 2008, January;31(1):56-73.

[30] Moortgat J, Sun S, Firoozabadi A. Compositional modeling of three-phase flow with gravity using higher-order finite element methods. Water Resources Research. 2011, May 11;47(W05511).

[31] Lesinigo M, D'Angelo C, Quarteroni A. A multiscale Darcy-Brinkman model for fluid flow in fractured porous media. Numerische Mathematik. 2011, April;117(4):717-752.

[32] Flemisch B, Darcis M, Erbertseder K, Faigle B, Lauser A, Mosthaf K, Muething S, Nuske P, Tatomir A, Wolff M, Helmig R. DuMu(x): DUNE for multi-phase, component, scale, physics, ... flow and transport in porous media. Advances in Water Resources. 2011, September;34(9, SI):1102-1112.

[33] Tatomir AB, Szymkiewicz A, Class H, Helmig R. Modeling Two Phase Flow in Large Scale Fractured Porous Media with an Extended Multiple Interacting Continua Method. Computer Modeling in Engineering and Sciences. 2011, July;77(2):81-112.

[34] Forsyth P. A Positivity Preserving Method for Simulation of Steam Injection for Napl Site Remediation. Advances in Water Resources. 1993;16(6):351-370.

[35] Yu S, Unger AJA, Parker B. Simulating the fate and transport of TCE from groundwater to indoor air. Journal of Contaminant Hydrology. 2009, July 21;107(3-4):140-161.

[36] Sleep B, Sykes J. Modelling the Transport of Volatile Organics in Variably Saturated Media. Water Resources Research. 1989, January;25(1):81-92.

[37] Forsyth P, Shao BY. Numerical simulation of gas venting for NAPL site remediation. Advances in Water Resources. 1991;14(6):354-367.

[38] Forsyth P. A Control Volume Finite-Element Approach to NAPL Groundwater Contamination. SIAM Journal On Scientific And Statistical Computing. 1991, September;12(5):1029-1057.

[39] Kaluarachchi J, Parker J. An Efficient Finite-Element Method for Modeling Multiphase Flow. Water Resources Research. 1989, January;25(1):43-54.

[40] Reynolds DA, Kueper BH. Multiphase flow and transport through fractured heterogeneous porous media. Journal of Contaminant Hydrology. 2004;71:89-110.

[41] Forsyth P, Rubin B, Vinsome P. The elimination of the constraint equation and modeling of problems with a non-condensable gas in steam simulation. Journal of Canadian Petroleum Technology. 1981;20(4):63-68.

[42] Forsyth P. 3-Dimensional Modeling of Steam Flush for DNAPL Site Remediation. International Journal for Numerical Methods in Fluids. 1994, December 30;19(12):1055-1081.

[43] Yu S, Freitas JG, Unger AJA, Barker JF, Chatzis J. Simulating the evolution of an ethanol and gasoline source zone within the capillary fringe. Journal of Contaminant Hydrology. 2009, February 27;105(1-2):1-17.

[44] Golder Associates Ltd.. Assessment of Extent of PCB plume at CWML Site Smithville, Ontario. Ontario Ministry of the Environment Smithville documents; 1999.

[45] Tang D, Frind E, Sudicky E. Contaminant Transport in Fractured Porous-Media - Analytical Solution for a Single Fracture. Water Resources Research. 1981;17(3):555-564.

[46] Agency for Toxic Substances and Disease Registry. Toxicological profile for Trichloroethylene. Atlanta, GA: U.S. Department of Health and Human Services, Public Health Service; 1997. September. 298 p.

[47] Link M, Squires R, Colburn I. Slope and Deep-Sea Fan Facies and Paleogeography of Upper Cretaceous Chatsworth Formation, Simi Hills, California. AAPG Bulletin-American Association of Petroleum Geologists. 1984;68(7):850-873.

[48] Sterling S, Parker B, Cherry J, Williams J, Lane J, Haeni F. Vertical cross contamination of trichloroethylene in a borehole in fractured sandstone. Ground Water. 2005, July-August;43(4):557-573.

[49] Cherry J, McWhorter D, Parker B. SCM Element 0-2: Overview of the Site Conceptual Model for the Migration and Fate of Contaminants in Groundwater at the Santa Susana Field Laboratory, Simi, California. In: Site Conceptual Model for the Migration and Fate of Contaminants in Groundwater at the Santa Susana Field Laboratory, Simi, California. Vol. 1. SSFL Groundwater Advisory Panel; 2009.

[50] Parker BL, Chapman SW, Cherry JA. Column Theme: Advances and Strategies in Groundwater Remediation. Ground Water. 2010, November-December;48(6):799-803.

[51] Neuman SP. Trends, prospects and challenges in quantifying flow and transport through fractured rocks. Hydrogeol J. 2005;13:124-147.

[52] Parker BL, Cherry JA, Chapman SW. Discrete Fracture Network Approach for Studying Contamination in Fractured Rock. AQUA mundi. 2012, December;:101-116.

[53] Wang J, Narasimhan T. Unsaturated Flow in Fractured Porous Media. In: Bear J, Tsang CF, de Marsily G, editors. Flow and Contaminant Transport in Fractured Rock. Academic Press; 1993. p. 325-394.

[54] Wang J, Narasimhan T. Hydrologic Mechanisms Governing Fluid-Flow in a Partially Saturated, Fractured, Porous-Medium. Water Resources Research. 1985;21(12):1861-1874.

[55] Makurat A. Laboratory experiments of fracture flow and fracture cross flow. In: Jha, PC and Gupta, RN editors. Proceedings of the Site Characterisation Practice; 2000. p. 271-284.

[56] Firoozabadi A, Hauge J. Capillary pressure in fractured porous media. JPT, Journal of Petroleum Technology. 1990;42(6):784-791.

[57] Firoozabadi A, Markeset T. Laboratory Studies in Fractured Porous-Media Part .1. Reinfiltration for Gas-Liquid Systems. In Situ. 1995;19(1):1-21.

[58] Dejam M, Hassanzadeh H. Formation of Liquid Bridges Between Porous Matrix Blocks. AICHE Journal. 2011, February;57(2):286-298.

[59] Saidi A. Reservoir Engineering of Fractured Reservoirs-Fundamentals and Practical Aspects. Paris: Total Edition Press; 1987.

[60] Unger A, Mase C. Numerical study of the hydromechanical behaviour of two rough fracture surfaces in contact. Water Resources Research. 1993, July;29(7):2101-2114.

[61] McDermott C, Kolditz O. Geomechanical model for fracture deformation under hydraulic, mechanical and thermal loads. Hydrogeology Journal. 2006, April;14(4):485-498.

[62] Walsh R, McDermott C, Kolditz O. Numerical modeling of stress-permeability coupling in rough fractures. Hydrogeology Journal. 2008, June;16(4):613-627.

[63] Dahan O, Nativ R, Adar E, Berkowitz B, Weisbrod N. On fracture structure and preferential flow in unsaturated chalk. Ground Water. 2000, May-June;38(3):444-451.

[64] Glass R, Nicholl M, Rajaram H, Wood T. Unsaturated flow through fracture networks: Evolution of liquid phase structure, dynamics, and the critical importance of fracture intersections. Water Resources Research. 2003, December 17;39(12).

[65] Dragila M, Weisbrod N. Fluid motion through an unsaturated fracture junction. Water Resources Research. 2004, February 13;40(2).

[66] Ji S, Nicholl M, Glass R, Lee K. Influence of a simple fracture intersection on density-driven immiscible flow: Wetting vs. nonwetting flows. Geophysical Research Letters. 2004, July 27;31(14).

[67] Ji S, Nicholl MJ, Glass RJ, Lee K. Influence of simple fracture intersections with differing aperture on density-driven immiscible flow: Wetting versus nonwetting flows. Water Resources Research. 2006, October;42.

[68] Pruess K, Oldenburg C, Moridis G. TOUGH2 User's Guide, Version 2.0. Berkeley, California 94720: Lawrence Berkeley National Laboratory; 1999. November.

[69] Glass R, Nicholl M, Pringle S, Wood T. Unsaturated flow through a fracture-matrix network: Dynamic preferential pathways in mesoscale laboratory experiments. Water Resources Research. 2002, December 7;38(12).

[70] Slough K, Sudicky E, Forsyth P. Numerical simulation of multiphase flow and phase partitioning in discretely fractured geologic media. Journal of Contaminant Hydrology. 1999, December;40(2):107-136.

[71] Cey E, Rudolph D, Therrien R. Simulation of groundwater recharge dynamics in partially saturated fractured soils incorporating spatially variable fracture apertures. Water Resources Research. 2006, September 19;42(9).

[72] Roels S, Vandersteen K, Carmeliet J. Measuring and simulating moisture uptake in a fractured porous medium. Advances in Water Resources. 2003, March;26(3):237-246.

[73] Kennel J, Parker BL, Cherry JA. SCM Element 4-3: Determination of Fracture Density and Fracture Set Orientations from Geophysical and Geologic Logs for the Chatsworth Formation at the Santa Susana Field Laboratory. In: Site Conceptual Model for the Migration and Fate of Contaminants in Groundwater at the Santa Susana Field Laboratory, Simi, California. Vol. 2. 2009.

[74] McWhorter DB. SCM Element 10-2: Groundwater Recharge, Santa Susana Field Laboratory, Ventura County, California. In: Site Conceptual Model for the Migration and Fate of Contaminants in Groundwater at the Santa Susana Field Laboratory, Simi, California. Vol. 3. 2009.

[75] van Dijke M, McDougall S, Sorbie K. Three-phase capillary pressure and relative permeability relationships in mixed-wet systems. Transport in Porous Media. 2001, July;44(1):1-32.

[76] Fagerlund FF, Niemi A, Oden M. Comparison of relative permeability-fluid saturation-capillary pressure relations in the modelling of non-aqueous phase liquid infiltration in variably saturated, layered media. Advances in Water Resources. 2006, November;29(11):1705-1730.

[77] Huyakorn P, Panday S, Wu Y. A 3-dimensional Multiphase Flow Model for Assessing NAPL Contamination in Porous and Fractured Media .1. Formulation. Journal of Contaminant Hydrology. 1994, June;16(2):109-130.

[78] Nitao J, Buscheck T. Infiltration of a Liquid Front in an Unsaturated, Fractured Porous-Medium. Water Resources Research. 1991, August;27(8):2099-2112.

[79] Oldenburg C, Pruess K. On Numerical Modeling of Capillary Barriers. Water Resources Research. 1993, April;29(4):1045-1056.

[80] Wu Y, Zhang W, Pan L, Hinds J, Bodvarsson G. Modeling capillary barriers in unsaturated fractured rock. Water Resources Research. 2002, November;38(11).

[81] Finsterle S, Fabryka-Martin J, Wang J. Migration of a water pulse through fractured porous media. Journal of Contaminant Hydrology. 2002, January;54(1-2):37-57.

[82] Amirtharaj ES, Ioannidis MA, Parker B, Tsakiroglou CD. Statistical Synthesis of Imaging and Porosimetry Data for the Characterization of Microstructure and Transport Properties of Sandstones. Transport in Porous Media. 2011, January;86(1):135-154.

[83] Schlumberger Water Services. SCM Element 4-2: Ground Truthing and Interpretation of Discrete Feature data From Core, Televiewer, and Geophysical Logs at the Santa Susana Field Laboratory. In: Site Conceptual Model for the Migration and Fate of Contaminants in Groundwater at the Santa Susana Field Laboratory, Simi, California. Vol. 2. 2009.

[84] Reitsma S, Kueper BH. Laboratory measurement of capillary pressure-saturation relationships in a rock fracture. Water Resources Research. 1994, April;30(4):865-878.

[85] Mendoza CA. Capillary pressure and relative transmissivity relationships describing two-phase flow through rough-walled fractures in geologic materials [PhD thesis]. Waterloo, ON, Canada: University of Waterloo; 1992.

[86] Abbey D, Martin P, Bester M, Andrachek R, McWhorter D. SCM Element 9-1: The Shallow-Deep Hydraulic Continuum at the Santa Susana Field Laboratory. In: Site Conceptual Model for the Migration and Fate of Contaminants in Groundwater at the Santa Susana Field Laboratory, Simi, California. Vol. 3. SSFL Groundwater Advisory Panel; 2009.

[87] McWhorter DB. SCM Element 10-1: Concepts for Shallow Groundwater Behavior and Recharge. In: Site Conceptual Model for the Migration and Fate of Contaminants in Groundwater at the Santa Susana Field Laboratory, Simi, California. Vol. 3. 2009.

[88] California Irrigation Management Information System. CIMIS Data[Internet]. [cited January, 2011].http://wwwcimis.water.ca.gov/cimis/data.jsp

[89] Montgomery Watson. Technical Memorandum -- Conceptual Site Model, Movement of TCE in the Chatsworth Formation, Santa Susana Field Laboratory, Ventura County, California. 2000. April.

[90] Haley & Aldrich. Appendix 4-P, Reports on Radiological Groundwater Characterization: 2004 Through 2006 Data Gap Investigation for Radiological Constituents in Groundwater. In: Draft Site-Wide Groundwater Remedial Investigation Report Santa Susana Field Laboratory, Ventura County, California. Vol. 5. MWH; 2009. p. 2623.

[91] Sterling S. Comparison of discrete depth sampling using rock core and removable multilevel system in a TCE contaminated fractured sandstone [Master's thesis]. Waterloo, ON, Canada: University of Waterloo; 1999.

[92] McWhorter DB, Reiners SH. SCM Element 8-1: Fracture Apertures Chatsworth Formation Santa Susana Field Laboratory. In: Site Conceptual Model for the Migration and Fate of Contaminants in Groundwater at the Santa Susana Field Laboratory, Simi, California. SSFL Groundwater Advisory Panel; 2009.

[93] Kennel J, Parker BL, Cherry JA, Reiners SH. SCM Elemend 8-2: Hydraulic Apertures Determined by Application of the Cubic Law to FLUTe Continuous Hydraulic Conductivity Profiling at the Santa Susana Field Laboratory, Simi, California. In: Site Conceptual Model for the Migration and Fate of Contaminants in Groundwater at the Santa Susana Field Laboratory, Simi, California. Vol. 3. SSFL Groundwater Advisory Panel; 2009.

[94] Nuske P, Faigle B, Helmig R, Niessner J, Neuweiler I. Modeling gas-water processes in fractures with fracture flow properties obtained through upscaling. Water Resources Research. 2010, September 24;46.

[95] Anon. Draft Site-Wide Groundwater Remedial Investigation Report; Santa Susana Field Laboratory, Ventura County, California. MWH; 2009.

[96] Pierce AA. Isotopic and hydrogeochemical investigation of major ion origin and trichloroethene degradation in fractured sandstone [Master's thesis]. Waterloo, ON, Canada: University of Waterloo; 2005.

[97] Unger A, Forsyth P, Sudicky E. Influence of alternative dissolution models and subsurface heterogeneity on DNAPL disappearance times. Journal of Contaminant Hydrology. 1998, April;30(3-4):217-242.

[98] Bhallamudi S, Panday S, Huyakorn P. Sub-timing in fluid flow and transport simulations. Advances in Water Resources. 2003, May;26(5):477-489.

[99] Wolff M, Flemisch B, Helmig R, Aavatsmark I. Treatment of Tensorial Relative Permeabilities with Multipoint Flux Approximation. International Journal of Numerical Analysis and Modeling. 2012;9(3):725-744.

[100] Unger A, Forsyth P, Sudicky E. Variable spatial and temporal weighting schemes for use in multi phase compositional problems. Advances in Water Resources. 1996;19(1):1-27.

[101] Demond A, Lindner A. Estimation of Interfacial-Tension Between Organic Liquids and Water. Environmental Science and Technology. 1993, November;27(12):2318-2331.

[102] Keller A, Chen M. Effect of spreading coefficient on three-phase relative permeability of nonaqueous phase liquids. Water Resources Research. 2003, October 16;39(10).

[103] Pankow JF, Cherry JA. Dense chlorinated solvents and other DNAPLs in groundwater: history, behavior, and remediation. Portland, OR: Waterloo Press; 1996.

[104] Ondarts M, Hort C, Platel V, Sochard S. Indoor Air Purification by Compost Packed Biofilter. International Journal of Chemical Reactor Engineering. 2010;8.

[105] Knauss K, Dibley M, Leif R, Mew D, Aines R. The aqueous solubility of trichloroethene (TCE) and tetrachloroethene (PCE) as a function of temperature. Applied Geochemistry. 2000, May;15(4):501-512.

[106]Chlorocarbons and Chlorohydrocarbons. Kirk-Othmer Encyclopedia of Chemical Technology. 2nd ed. New York, NY: Wiley Interscience; 1964.

[107] Chiao FF, Currie RC, McKone TE. Intermedia Transfer Factors for Contaminants Found at Hazardous Waste Sites: Trichloroethylene. Davis, California, 95616: Department of Environmental Toxicology, University of California; 1994. December.

[108] Hurley J. Rock Core Investigation of DNAPL Penetration and Persistence in Fractured Sandstone [Master's thesis]. Waterloo, ON, Canada: University of Waterloo; 2003.

[109] Abriola L, Pinder G. A Multiphase Approach to the Modeling of Porous-Media Contamination by Organic-Compounds .2. Numerical-Simulation. Water Resources Research. 1985;21(1):19-26.

[110] Leverett M. Capillary behavior in porous solids. Transactions of the American Institute of Mining and Metallurgical Engineers. 1941;142:152-169.

[111] Stone H. Estimation of 3-phase relative permeability and residual oil data. Journal of Canadian Petroleum Technology. 1973;12(4):53-61.

[112] Oliveira L, Demond A. Estimation of primary drainage three-phase relative permeability for organic liquid transport in the vadose zone. Journal of Contaminant Hydrology. 2003, November;66(3-4):261-285.

[113] Oak M, Baker L, Thomas D. 3-phase relative permeability of berea sandstone. Journal of Petroleum Technology. 1990, August;42(8):1054-1061.

[114] Bogdanov II, Mourzenko VV, Thovert J, Adler PM. Two-phase flow though fractured porous media. Physical Review E. 2003;68(026703).

[115] Tsakiroglou CD, Klint KES, Nilsson B, Theodoropoulou MA, Aggelopoulos CA. From aperture characterization to hydraulic properties of fractures. Geoderma. 2012, JUL;181:65-77.

[116] Spiteri E, Juanes R. Impact of relative permeability hysteresis on the numerical simulation of WAG injection. Journal of Petroleum Science and Engineering. 2006, February 16;50(2):115-139.

[117] Enouy R. Continuum approach to two- and three-phase flow during gas-supersaturated water injection in porous media [Master's thesis]. University of Waterloo; 2010.

[118] Holm R, van Dijke MIJ, Geiger S. Three-Phase Flow Modelling Using Pore-Scale Capillary Pressures and Relative Permeabilities for Mixed-Wet Media at the Continuum-Scale. Transp Porous Med. 2010, May;81:423--442.

[119] Birdsell K, Newman B, Broxton D, Robinson B. Conceptual models of vadose zone flow and transport beneath the Pajarito Plateau, Los Alamos, New Mexico. Vadose Zone Journal. 2005, August;4(3):620-636.

[120] Snow D. Anisotropic Permeability of Fractured Media. Water Resources Research. 1969;5(6).

[121] McWhorter DB. SCM Element 17-1: DNAPL Fate and Transport In the Vadose Zone. In: Site Conceptual Model for the Migration and Fate of Contaminants in Groundwater at the Santa Susana Field Laboratory, Simi, California. Vol. 4. 2009.

[122] Martin P, Abbey D, Cherry JA, Parker BL, Andrachek R, McWhorter D. SCM Element 6-2: Decreased Hydraulic Conductivity with Depth at the SSFL. In: Site Conceptual Model for the Migration and Fate of Contaminants in Groundwater at the Santa Susana Field Laboratory, Simi, California. Vol. 2. 2009.

[123] Arslan AT, Koca MY, Aydogmus T, Klapperich H, Yilmaz HR. Correlation of Unconfined Compressive Strength with Young's Modulus and Poisson's Ratio in Gypsum from Sivas (Turkey). Rock Mechanics and Rock Engineering. 2008, December;41(6):941-950.

[124] Rohde J, Feng H. Analysis of the Variability of Unconfined Compression Tests of Rock. Rock Mechanics and Rock Engineering. 1990, July-September;23(3):231-236.

[125] Vasarhelyi B, Van P. Analyzing the influence of the water saturation on the strength of sandstones. In: Cotthem, AV and Charlier, R and Thimus JF and Tshibangu JP editors. Proceedings of the Eurock 2006 Multiphysics Coupling and Long Term Behaviour in Rock Mechanics; 2003. p. 169-172.

Appendices

Appendix A SSFL Simulation Parameters

Herein, we recount our parameters for reproducibility and to point out gaps and disagreement in data and modeling approaches for various physical phenomena. We list well-understood simulation parameters for fluid phases in Table A-1, component/chemical species in Table A-2, equilibrium partitioning relationships and parameters in Table A-3, and porous medium properties in Table A-4. Finally, we discuss the most challenging parameters in a three-phase context, capillary pressure versus saturation and relative permeability versus saturation relationships.

Table A-1 Phase property/parameter data

Property/Parameter	**Value**
Phase compressibility:	
$\hat{C}_q$ [kPa^{-1}]	3.0×10^{-6} [i]
$\hat{C}_n$ [kPa^{-1}]	4.3×10^{-7} [i]
$\hat{C}_g = V/(nRT)$ with "pure air" at 10°C [kPa^{-1}]	1.037×10^{-2}
Phase viscosity (at 10°C):	
μ_q [kPa d]	2.4×10^{-11}
μ_g [kPa d]	1.6×10^{-13} [i]
μ_n [kPa d]	8.9×10^{-12}
Phase interfacial tensions:	
σ_{nq} [mN/m]	34.5 [ii]
σ_{gq} [mN/m]	72.7 [iii]
σ_{gn} [mN/m]	28.8 [iii]
Molecular diffusion coefficient:	
D_l^* [m^2/day]	0.0 [iv]

[i] Unger et al. [100]; [ii] Demond and Lindner [101]; [iii] Keller and Chen [102]; [iv] Based on CV size, numerical dispersion will dominate modeled physical diffusion.

Table A-2 Component property/parameter data

Property/Parameter	Value
Molecular weight	
ω_{water} [kg/mol]	0.01802 [i]
ω_{air} [kg/mol]	0.02897 [i]
ω_{TCE} [kg/mol]	0.1315 [ii]
Standard component density	
M^*_{water} [mol/m^3]	55,500 [i]
M^*_{air} [mol/m^3]	41.05 [i]
M^*_{TCE} = 1460 kg/m^3 [ii] / ω_{TCE} [mol/m^3]	11,100

[i] Unger et al. [100]; [ii] [103]

Table A-3 Equilibrium partitioning data at 10°C and P_g=P_{atm}=100 kPa

Property/Parameter	Value
Water:	
$P_{\text{vap,w}}$=10^{23.1964[i]-3816.44[i]/(227.05[i]+10)}/1000 [kPa] in Z_{wgq}=$P_{\text{vap,w}}/P_g$	1.2
TCE:	
$C_{\text{sol,TCE}}$ [g/L] in $Z_{cqn} = C_{\text{sol,TCE}} M_{\text{water}}/(M_{\text{TCE}}\rho_q)$	1.3[ii]
$P_{\text{vap,TCE}}$=10^{10.128 [iii]-1830.4 [iii] /(273 [iii]+10)}/1000 [kPa] in Z_{cgq}=$P_{\text{vap,TCE}}/P_g$	4.6

[i] Ondarts et al. [104]; [ii] Aggregated from Knauss et al. [105]; [iii] Kirk-Othmer [106] as cited in Chiao et al. [107]

Table A-4 Porous medium properties

Property/Parameter	Value
Porosity, ϕ [-]	0.13[i]
Intrinsic permeability, $\mathbb{K}$, homogeneous and isotropic [m^2]	1×10^{-14} [ii]
Cementation exponent, m [-]	2.074 [ii]
Bulk density, ρ_b [kg/m^3]	2.65×10^3 [iii]
Dispersivity, longitudinal and transverse, $\alpha_L^l = \alpha_T^l, \forall l$ [m]	0.0 [iv,v]
Sorption coefficients, K_d [m^3/kg]	0.0 [iv]

[i] SSFL sandstone arithmetic mean [108]; [ii] SSFL sample C4-137 [82]; [iii] Unger et al. [100]; [iv] Dissolved transport is not of primary focus in this study; [v] Numerical dispersion is assumed to dominate physical dispersion

Two-phase P_c-S curves are based on the experimental results and analysis methods of Amirtharaj et al. [82]. They performed mercury intrusion porosimetry tests on rock cores taken from the Chatsworth Formation at the SSFL site, specifically sample C4-137. The

data from this sample are fitted with Brooks-Corey curves, depicted in Figure A-1d-f. Two-phase P_c-S curves are bound together using the following equations:

$$\begin{aligned} P_q &= P_n - \hat{\alpha} P_{c,nq}(S_q) - (1-\hat{\alpha}) P_{c,nq}(S_q = 1) \\ P_g &= P_n + \hat{\alpha} P_{c,gn}(S_g) + (1-\hat{\alpha})\left[P_{c,gq}(S_g) - P_{c,nq}(S_q = 1)\right] \\ \hat{\alpha} &= \min\langle 1, S_n / S_n^* \rangle \end{aligned} \tag{30}$$

where $P_{c,gn}, P_{c,gq}, P_{c,nq}$ [kPa] are two-phase capillary pressure curves as functions of saturation and S_n^* is a blending parameter [-]. The blending function $\hat{\alpha}$ and parameter S_n^* provide a linear transition from the gas-aqueous $P_{c,gq}$ to the gas-NAPL-aqueous $P_{c,gn}$ and $P_{c,nq}$ capillary pressure system. This yields the correct the capillary pressure in the absence of NAPL and when NAPL is present in sufficient quantity $S_n \geq S_n^*$. The linear transition was introduced in Forsyth [38] to remove the discontinuity in the relationships proposed in Kaluarachchi and Parker [39] and Abriola and Pinder [109] that transition abruptly at a critical NAPL saturation.

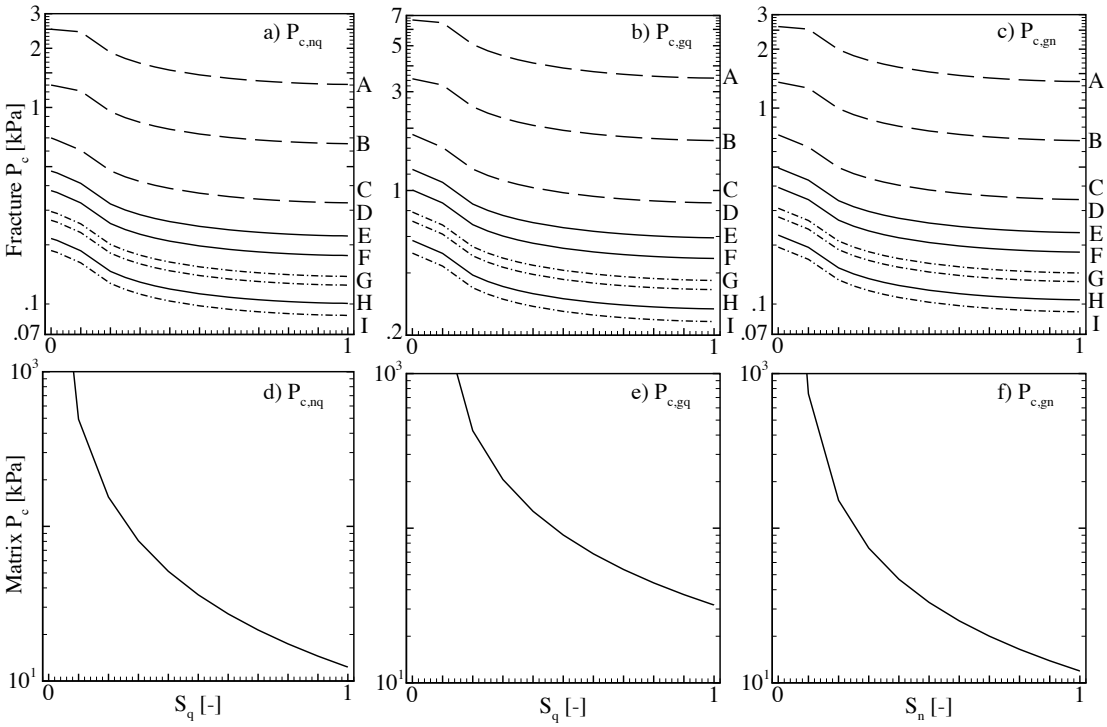

Figure A-1 Fracture capillary pressure versus saturation relationships for a) the NAPL-aqueous system, b) the gas-aqueous system and c) the gas-NAPL system with line labels in A) 50 μm fracture, B) 100 μm fracture, C) 200 μm fracture, D) 295 μm fracture, E) 371 μm fracture, F) 474 μm fracture intersection, G) 525 μm fracture intersection, H) 650 μm fracture and I) 748 μm fracture intersection. Matrix capillary pressure-saturation relationships for d) the NAPL-aqueous system, e) the gas-aqueous system and f) the gas-NAPL system.

The three-phase relationships for the rock matrix as derived from Figure A-1d-f are shown in Figure A-2. Figure A-2a shows capillarity in the NAPL-aqueous system where the values along the $S_g = 0$ axis correspond to Figure A-1d and the values along $S_n = 0$ correspond to Figure A-1e. Figure A-2b shows capillarity in the gas-liquid system with correspondences to Figure A-1e and Figure A-1f by the axes $S_n = 0$ and $S_q = 0$, respectively.

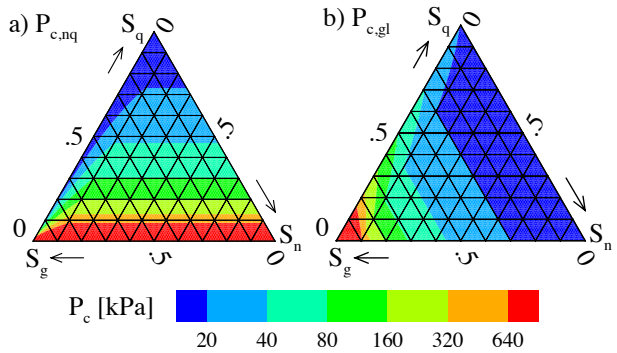

Figure A-2 Matrix capillary pressure relationships for a) NAPL-aqueous, S_n^* = 0.1, and b) gas-liquid, S_n^*=0.1.

Capillary pressure versus saturation curves shown in Figure A-1a-c have origins in the numerical study by Mendoza [85]. Mendoza's curve for a 200 μm fracture is scaled according to a modified version of the dimensionless scaling function [35] equation (6), originating from Leverett [110], using pore size distribution parameter $\tilde{\alpha} = 0.5$ to produce curves for all relevant fracture apertures. The dimensionless scaling equation and simplified scaling relationship are given by:

$$P^D_{cl_1l_2} = \frac{P_{cl_1l_2}}{\sigma_{l_1l_2}}\left(\frac{k}{\phi}\right)^{\tilde{\alpha}} \rightarrow P_{cl_1l_2,2b} = P_{cl_1l_2,200}\frac{200}{2b} \tag{31}$$

where: $P^D_{cl_1l_2}$ is a dimensionless capillary pressure curve [-]; $\sigma_{l_1l_2}$ is interfacial tension between phases l_1 and l_2 [mN/m]; $P_{cl_1l_2,200}$ is the source capillary pressure data for a 200 μm fracture [kPa]; $P_{cl_1l_2,2b}$ is the new capillary pressure data for a fracture with aperture $2b$ [kPa]; $k = (2b)^2/12$ is the intrinsic permeability of a fracture with aperture $2b$ [m^2]; and $\phi = 1$ for fractures.

For the fracture network it suffices to present only the two-phase P_c-S relationships shown in Figure A-1a-c because: only the aqueous phase and NAPL are present in the saturated zone, in which case Figure A-1a applies; the capillary fringe is formed based on

the gas-aqueous phase relationship in Figure A-1b, and thereafter NAPL displaces aqueous phase; and fractures transition abruptly from aqueous phase- to gas-saturated at the top of the capillary fringe. Aqueous phase is reduced to residual $S_{qr} = 0.02$, and thus Figure A-1c is reasonably accurate to describe the remaining gas-NAPL capillary system. Nevertheless, the numerical model uses the aforementioned blending procedure for fracture CVs, which defines capillary pressure differences when three phases are present.

Estimation of three-phase relative permeability, especially for the NAPL phase, in a porous medium and in fractures is challenging. A number of models, including two proposed by Stone [111], have been assessed by Oliveira and Demond [112] for their ability to describe a comprehensive set of two- and three-phase relative permeability measurements in water-wet Berea sandstone [113]. According to Stone [111], relative permeabilities relevant to a three-phase displacement may be approximately reconstructed from knowledge of two-phase relative permeabilities as follows: the relative permeability of the most (least) wetting phase is a function only of the saturation of that phase and is the same function in a three-phase system as in a two-phase system; the relative permeability of the intermediate wetting phase has a functional dependence on saturations of the other two. A wide variety models have been used in recent studies for relative permeability in rough fractures. A small set of examples include: Moortgat et al. [30] who used the Stone I model; Bogdanov et al. [114] who simply used the square of NAPL saturation; and Cey et al. [71] used the Brooks-Corey-Mualem k_r model. Most recently Tsakiroglou et al. [115] concluded that Corey-type functions were appropriate macro-scale flow parameters, based on their pore-scale fracture flow simulations.

For the purposes of our investigation, the aqueous and gas phase relative permeabilities in a three-phase system were inferred from NAPL-water and gas-liquid capillary pressure data from the SSFL site sample C4-137 (see Figure A-1d-f) using the Corey-Burdine model:

$$k_{rq} = \left(\frac{S_q - S_{qr}}{1 - S_{qr}}\right)^{1+m+2/\lambda_{nq}} \tag{32}$$

$$k_{rg} = \left(1 - \frac{S_l - S_{lr}}{1 - S_{lr}}\right)^{m} \left[1 - \left(\frac{S_l - S_{lr}}{1 - S_{lr}}\right)^{1+2/\lambda_{gl}}\right] \tag{33}$$

where S_q and S_l are the aqueous phase and total liquid saturations [-], S_{qr} and S_{lr} are residual saturations [-], and λ_{nq} and λ_{gl} are Corey exponents that best describe the

capillary pressure data of Figure A-1d-f. The NAPL relative permeability is a function of both the gas and aqueous phase saturations and, according to Stone's second model (see also [43]), is given by:

$$k_{rn} = k_{r(nq_c)}\left[\left(\frac{k_{r(nq)}}{k_{r(nq_c)}} + k_{rq}\right)\left(\frac{k_{r(ng)}}{k_{r(nq_c)}} + k_{rg}\right) - k_{rq} - k_{rg}\right] \tag{34}$$

where $k_{r(nq_c)} = 1$ and $k_{r(nq)}$, $k_{r(ng)}$ are the NAPL relative permeability in the two-phase aqueous-NAPL and NAPL-gas systems, respectively. The latter two terms are also assumed to obey the Corey-Burdine model:

$$k_{r(nq)} = \left(1 - \max\left\{\frac{1 - S_n - S_{qr}}{1 - S_{qr}}, 0\right\}\right)^m \left[1 - \max\left\{\frac{1 - S_n - S_{qr}}{1 - S_{qr}}, 0\right\}^{1+2/\lambda_{nq}}\right] \tag{35}$$

$$k_{r(ng)} = \left(\frac{S_l - S_{lr}}{1 - S_{lr}}\right)^{1+m+2/\lambda_{ng}} \tag{36}$$

Figure A-3 shows relative permeability versus three-phase saturation for a) the aqueous phase, b) the NAPL phase, c) the gas phase, and d) the NAPL phase as calculated according to the Stone II model. From the diagram it is apparent that the Stone II model exhibits a relatively large range of saturations in (S_q,S_n,S_g)-space where the NAPL is immobile. This immobile range is due to the fact that calculated negative k_{rn} values are truncated to zero and is therefore not physical (see also Oliveira and Demond [112] and Spiteri and Juanes [116]). Such behavior is not unique to the Stone II model. Spiteri and Juanes [116] have pointed out the inadequacy of all available models to describe oil relative permeability in the range of very low oil saturations (see also Keller and Chen [102]), which is precisely what is needed in order to simulate imbibition of NAPL from the fractures into partially saturated matrix. An empirical model for oil relative permeability that describes the mobility of water-flood residual oil in the presence of a flowing gas phase in a three-phase system has been recently proposed by Enouy [117]:

$$k_{rn} = k_{r(nq)} + \Lambda k_{rg} k_{rnc}\left(1 - k_{rg}\right)(1 - k_{rnc}) \tag{37}$$

In the above expression, $k_{r(nq)}$ and k_{rg} have their usual meaning (see equations (35) and (33)), whereas the constant Λ and function $k_{rnc} = [(S_n - S_{nrc})/(1 - S_{nrc})]^{n_n}$ are determined empirically by fitting of the model to experimental three-phase flow data. NAPL relative permeability in a three-phase system calculated using the model of Enouy [117] are shown in Figure A-3b, which bears a qualitative resemblance to Figure 8a in reference [75] and Figure 5b in reference [118]. The additional parameter values used in

this model are listed in Table A-5. These values were determined by Enouy [117] for a three-phase flow scenario very different than the ones considered here and may not be applicable to the problem at hand. Precise determination of relative permeabilities for aqueous-NAPL-gas flow in SSFL sandstone material is beyond the scope of this study.

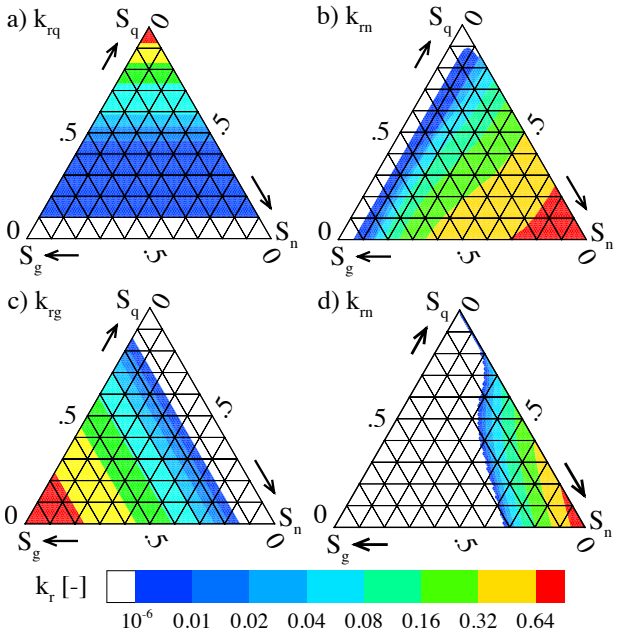

Figure A-3 Relative permeability of the matrix for a) aqueous phase k_{rq}, b) NAPL using Enouy-Stone k_{rn} model, c) gas phase k_{rg}, and d) NAPL with Stone II k_{rn} model. White indicates immobile regions.

Table A-5 Parameters for the Corey-Burdine and Enouy NAPL relative permeability models

Property/Parameter	**Value**
Residual aqueous phase saturation, S_{qr} [-]	0.012 [i]
Residual total liquid saturation, S_{lr} [-]	0.055 [i]
Corey curve fitting parameters:	
λ_{nq} [-]	0.66 [i]
λ_{gl} [-]	0.73 [i]
Enouy model fitting parameters:	
Λ [-]	4.5 [ii]
S_{nrc} [-]	0.06 [ii]
n_n [-]	1.5 [ii]

[i] Reference SSFL sample C4-137 [82]; [ii] Reference silica sand [117]

For relative permeability in fractures, we use the k_r-S relationships determined numerically by Mendoza [85] for rough-walled fractures. The two-phase relationships, k_{rq}-S and k_{rn}-S, are shown in Figure A-4. We note the qualitative similarity in the shapes of

the Mendoza and the Tsakiroglou k_r-S relationships (indeed, they are both Corey-type functions), but disagreement in the S_{qr} values. Our selection of S_{qr} values based on [85] ought to be revisited in future simulations, as they will have a bearing on antecedent aqueous phase saturation and hence NAPL flow in fractures. For lack of definitive experimental data, the same k_{rq}-S and k_{rn}-S curves are reused for the liquid-gas system. All sets of curves are then blended using the Enouy procedure described above.

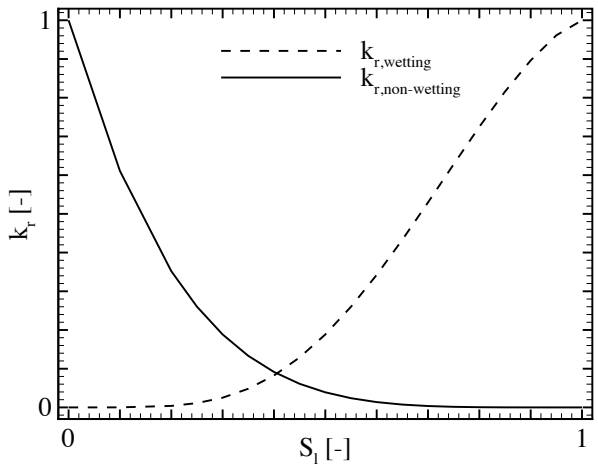

Figure A-4 Relative permeability versus saturation relationships for a rough-walled fracture used for the NAPL-aqueous and the liquid-gas systems in fractures of all apertures.

Appendix B Modeling Paradigm Comparison

To highlight the importance of capillary barrier effects at discrete fractures to water saturation in the vadose zone, we carry out a numerical experiment that contrasts model results under four different modeling paradigms: single continuum (SCM), equivalent porous medium (EPM), dual permeability (DK), and discrete fracture network (DFN). Birdsell et al. [119] carried out a similar exercise in comparing modeling paradigms in the context of vadose zone beneath the Los Alamos National Lab site, New Mexico; we base our experiment on theirs in spirit, and we refer to their article for a more in-depth description of modeling paradigms. Capillary barriers are directly modeled only in the DFN simulations. Therefore, this "comparison" is more of an exposition of the inadequacy of the SCM, EPM, and DK to model saturation conditions in the vadose zone of the SSFL site, and a cursory validation of the DFN modeling approach.

Here, we apply the numerical model *CompFlow Bio* with subsets of the SSFL site parameters to create or mimic four different modeling paradigms. We restrict the conceptual scenario depicted in Figure 2-1 to an aqueous-gas two-phase system in a 0.3×0.3×30 m, pseudo 1D column of fractured rock. One vertical fracture covers the entire x = 0 m face of the domain. This fracture is connected to adjacent PM and fracture CVs which alternate each 0.3 m in the z-direction. We take the same boundary conditions, as described previously, including gas exchange and steady-rate recharge boundaries at the top and a hydrostatic water boundary at the bottom. For discrete fractures or equivalency calculations we assume a uniform fracture density of 3 per metre in the x- and z-directions. Fracture and matrix permeability parameters are listed in Table B-1 and we use the k_r-S-P_c relationships described in section 4.2.3.

Table B-1 Comparison of fracture parameters used in the 1D column simulations.

Paradigm	Property	Value
SCM	k_m	1.0×10^{-14} m^2
	k_r-S-P_c	homogeneous, PM
EPM	$k_{m,unsat}$, z > 10.5 m	1.0×10^{-14} m^2
	$k_{m,sat}$	9.4×10^{-13} m^2
DK	k_m	1.0×10^{-14} m^2
	k_f	1.9×10^{-9} m^2
	k_r-S-P_c	homogeneous, PM; 150μm fracture
	fracture spacing	uniform, 3 per metre
U. DFN 40%	α	0.40
U. DFN 10%	α	0.10
U. DFN 5%	α	0.05
R. DFN 10%	α	0.10
	k_f	varies by fracture aperture
	k_r-S-P_c	homogeneous, PM; various, by fracture aperture
	fracture spacing	random, 2.5 per metre

From simplest to most complex we now briefly describe essential features of each modeling paradigm and our choices for parameterization: The basic assumption in SCM is that fractures do not influence flow. Thus, we apply the Chatsworth formation sandstone properties and constitutive relationships in a homogeneous fashion throughout the domain and omit all fractures. In the EPM model, fractures are still omitted but modifying the properties of the rock matrix captures their influence. We apply the calculation of Snow [120] to calculate the bulk intrinsic permeability of the porous medium. The caveat to this calculation is that it assumes that the porous media and fractures are fully water saturated. Here, we apply it to intrinsic permeability in the saturated zone and hold the intrinsic permeability of the unsaturated zone the same as SCM. Next, the DK model contains both fractures and PM, each continuum with its own distinct permeability and k_r-S-P_c relationships. Fracture CVs are modeled in the same way (e.g. aperture, volume, network connectivity, etc.) as their discrete counterparts, but we use a modified version of *CompFlow Bio* that prevents fractures from cross cutting porous medium blocks. Thus, the porous medium continuum is fully connected in the z-direction. Considering just a single porous medium block as an example, the surface area for fracture-matrix interaction is the

block's upper and lower face plus one of its side faces. Transfer over this area is calculated by the pressure-driven fluid flux, as per equations (1) and (14). Finally, our DFN paradigm assumes that fractures separate adjacent matrix blocks to varying degrees. We examine the consequence of this separation by using asperity contact ratios of α=0.95 (excellent matrix connectivity), 0.40, 0.10, 0.005 (poor matrix connectivity), or equivalently, 95%, 40%, 10% and 5%.

Also, for comparison to the results of these 1D models, we include the S_q-z profile from the x=15 m scan line of the 2D SSFL simulation. This simulation is identical in parameterization to DFN-10%, except for the domain and discretization. In RDFN-10% average density of the random horizontal fractures is only 2.5 per metre as opposed to 3 per metre, porous medium CVs are not uniformly 0.3 m thick, and no fully penetrating vertical fracture is present.

Results of the four different paradigms, i.e. seven different parameterizations, depicted as aqueous phase saturation in the matrix versus depth appear in Figure 4-6. Here we see the SCM, EPM, DK, and DFN-95% produce nearly identical results with an upper-vadose zone saturation of ~60%. In the sequence DFN-40%, 10%, and 5% (for decreasing asperity contact ratio), the matrix becomes progressively more saturated. (We note that in the DK and DFN simulations the gas phase saturation in fractures is near to 98%.) Decreasing asperity contact area decreases the ability for direct matrix-to-matrix flow. Hence, it reduces the infiltrating water's ability to avoid capillary barriers caused by the air-filled discrete fractures. In turn, this causes water saturation in the matrix to rise.

The DFN simulations with α=10% to 40% are nearer the target vadose zone water saturation of 70% [121] than all the other simulations. We have not carried out a systematic analysis. Other factors that influence on bulk permeability, such as infiltration rate, heterogeneity, stratigraphy, fracture network characteristics, etc., or that influence fluid flow, such as k_r-S-P_c relationships, etc., would affect the water saturation profile. Pending this analysis, our conjecture remains that too much connectivity/conductivity in the matrix will underpredict water saturation and too little connectivity will overpredict it; the DFN paradigm with asperity contact ratio parameter is the best model alternative that harmonizes with the available data.

Appendix C Asperity Contact Ratio

The asperity contact ratio, α, is a value representing the area where opposing rough fracture walls touch per unit area of fracture plane. As we have demonstrated in Sections 3.2.2.3, 4.3.1.2, and Appendix B, this model parameter is influential to water saturation in the vadose zone by forming asperity contact "bridges" for fracture cross flow. These bridges allow wetting-phase fluids to circumvent fracture void space filled with non-wetting fluid. Here we emphasize that this is not merely a fitting parameter and we present how it may be calculated using a SSFL site-relevant example.

The general process involves combining a measurement of the unconfined compressive strength of the rock with an estimate of the normal stress at a fracture plane. A ratio of these quantities determines, in turn, the dimensionless contact stress, relative fracture closure, and finally the asperity contact ratio.

Martin et al. [122], Table 1, report the average unconfined compressive strength of SSFL site sandstone as σ_c = 40 MPa. Applying the relationship for sandstone listed in Table 1 of Arslan et al. [123] based on data of Rohde and Feng [124], we calculate the Young's modulus as E_t [GPa] $= 2.25(\sigma_c$ [MPa]$)^{0.523} = 2.25(40)^{0.523} = 15.5$ GPa.

For the normal stress we choose z = 20 mbgs, the approximate depth to the water table, as a representative depth. Following from Eqn 1 in [122], with their bulk density value ρ_b = 2435 kg/m^3 and with g = 9.81 m/s, the normal stress is $\sigma_n = \rho_b g z$ = 2435 kg/m^3 × 9.81 m/s^2 × 20 m = 0.48 MPa.

Following from [60], by dividing the normal stress by the Young's modulus we calculate the dimensionless contact stress value of σ_c/E_t = 0.48 MPa ÷ 15 GPa = 3.2×10^{-5}. Making use of the dimensionless contact stress versus relative closure and percent contact area versus relative closure relationships in [60], Figures 11a-b, respectively, our dimensionless contact stress of 3.1×10^{-5} yields a relative closure of 0.3, which in turn yields a percent contact area of 10%.

Alternatively, using results of an empirical study by Vasarhelyi and Van [125] the Young's modulus may be estimated by the relationship for unsaturated sandstone portrayed in Figure 4 of [125]. This relationship gives $E_t = 178\times\sigma_c = 7.1$ GPa. As before, dividing the normal stress by this second Young's modulus value we have 0.48 MPa ÷

7.1 GPa $= 6.7\times10^{-5}$. From the figures in [60] this yields a relative closure of 0.45 and a closure of 20%.

Based on the calculations above and other numerical sensitivity analyses (ones in which the infiltration rate, matrix intrinsic permeability, and infiltration rate were varied; not shown), we adopt α = 10%.